SYNTHESIS, MODIFICATION, AND ANALYSIS OF TITANIUM DIOXIDE NANOPARTICLES FOR PHOTOCATALYTIC FUEL GENERATION

by

ASHLEY MARIE PENNINGTON

A dissertation submitted to the

School of Graduate Studies

Rutgers, The State University of New Jersey

In partial fulfillment of the requirements

For the degree of

Doctor of Philosophy

Graduate Program in Chemical and Biochemical Engineering

Written under the direction of

Fuat E. Celik

And approved by

_____

_____

_____

_____

New Brunswick, New Jersey

May, 2018

ABSTRACT OF THE DISSERTATION

Synthesis, Modification, and Analysis of Titanium Dioxide Nanoparticles for Photocatalytic Fuel Generation

by
ASHLEY MARIE PENNINGTON

Dissertation Director:

Fuat E. Celik

Elucidating structural and compositional polymorph changes of multi-phase semiconductors in a quick and quantitative manner is important for their manufacturing and applications in catalysis alike. Derivative peak fitting of diffuse-reflectance UV-visible spectra (DPR) is presented as an inexpensive, fast and quantitative method to estimate both the composition of a multi-phase semiconductor sample as well as the band gap energies of each component semiconductor in the mixture. Compositional measurements from DPR were in good quantitative agreement with XRD and Raman analysis. The application of in situ UV-Visible Spectroscopy DPR allowed for the on-stream determination of the onset temperature for rutilization during calcination.

The synthesis and modification of anatase phase titanium dioxide was investigated. High pressure high temperature annealing (HPHT) under various gases lacking a partial pressure of oxygen induces the formation of paramagnetic defects as

measured by Electron Paramagnetic Resonance (EPR) and X-ray Photoelectron Spectroscopy (XPS). The presence of these defects increased the metal-free photocatalytic activity of the samples towards hydrogen evolution from photocatalytic methane steam reforming (MSR) under UV illumination. The high concentration of unique Ti^{3+} defect sites generated during annealing catalyze hydrogen evolution, avoiding the need for precious metal cocatalysts, while anatase lacking these defects is inactive.

Metal-free hydrogen evolution from MSR over the annealed anatase and is compared to hydrogen evolution over the annealed sample with a nickel cocatalyst. The addition of nickel cocatalyst increased the photocatalytic methane activation as well as the hydrogen production rate between 773 K and 973 K. Under UV illumination catalyst activity was stable for hydrogen generation from MSR at a steam to carbon ratio of 0.9 for over 8 hours, owing to the regeneration of Ti^{3+} defects by UV photoexcitation, preventing coking on the surface, while activity decayed in the dark due to coking on the nickel cocatalyst. This work shows that the implementation of nickel supported on defect-rich anatase TiO_2 for highly stable photocatalytic hydrogen evolution from MSR with a major reduction in coking at low steam to carbon ratios.

Low pressure flame synthesis using a burner-stabilized premixed stagnation flat flame was employed to produce high surface area, carbon doped, anatase TiO_2 with a particle size below the quantum confinement limit. These nanoparticles had a 3.5-fold decrease in particle size (7 nm) and a 12-fold increase in surface area (187 m^2 g^{-1}) compared to commercial anatase. When the as synthesized particles are heated above 473 K, a majority of the carbon in the sample migrates to the surface and burns off, while

this process decreases the overall surface area of the sample, it slightly increases the particle size therefore decreases the band gap energy while increasing the average pore diameter, and the photocatalytic activity as measured by photocatalytic water reduction.

Acknowledgements

To begin, I would like to sincerely thank my research advisor, Prof. Fuat Celik, for the opportunity to work with the Celik Catalysis Group. His enthusiastic guidance and support has not only guided me through my thesis work but has also increased my understanding of catalytic processes, as well as what I am to expect when I become a professor. For their time and effort, I would like to thank the members of my thesis committee: Prof. Nina Shapley, Prof. George Tsilomelekis, and Prof. Stephen Tse.

I would like to thank the School of Engineering for supporting my first year via the Kurt Venkataraman Fellowship. I would also like to thank Sigma Xi, The Scientific Research Society, for supporting my research via the Grants In Aid of Research.

My colleagues in the Celik Catalysis Group, Alec Hook, and Boris Sheludko, have given me immense support. All of the amazing undergraduate research assistants that I have had the pleasure of mentoring in the Celik Catalysis Group: Katelyn Dagnall, Rachel Yang, Amanda Okonmah, Daryl Munoz, Umang Parikh, Kaitlyn Dickson, Robert Lavroff, Edward Zhao, Carolina Radecki, Haley Yang Hu, Stefanie Traeger, Valerie Balance, Taniya Arora, and Sean Noble; and in the Tse Lab: Jonathan Shi, Chidozie Buruzie, and Kartik Chapora. I would like to thank them for their wonderful attitudes and their unfailing work ethic that helped me become a better mentor and helped this project to progress towards completion.

I would like to thank our collaborators. Dr. John Landers and Prof. Alexander Niemark for training on and access to BET surface area and pore distribution analysis. Prof. Stephen Tse for access to the low pressure flame synthesis apparatus. Dr. Paul Smith, Dr. Alexi Tyrishkin, and Prof. G. Charles Dismukes for training on and access to EPR

Spectroscopy. Dr. Maureen Lagos and Prof. Phil Batson for training on and access to the UltraSTEM. Dr. Kevin Wyman and Prof. Paul G. Falkowski for training on and access to the SEM., and Thomas J. Emge for meaningful discussion on the interpretation of XRD patterns

I would like to thank my family, especially my mother and my boyfriend, who spent countless hours helping me to become better every day. Finally, a word to my 6 younger siblings for whom I blaze a path: There is no shortcut to any place worth going, therefore you must never give up.

Table of Contents

Table of Figures

Table of Tables

Chapter 1: Introduction

1.1 Hydrogen Gas, Fuel

Hydrogen gas has long been touted as a zero emissions fuel.[1] However, the majority of hydrogen is commercially produced from non-renewable, non-sustainable processes such as the steam reforming of fossil-fuel derived methane. If hydrogen could be derived from renewable sources such as biomass or biogas efficiently at large scales, then hydrogen would become and even more viable alternative to fossil fuels. Two promising sources of biogas are anaerobic digestion of food waste and capture of eking and flared landfill gas. The net-carbon-neutral production of hydrogen can be achieved via the photocatalytic reforming of biomass or the photocatalytic steam reforming of methane derived from the anaerobic digestion of food waste. The desired product of the photocatalytic methane steam reforming (PMSR) is hydrogen gas, although carbon dioxide (CO_2) is produced as a byproduct during the reforming process. Since the carbon source for this project (biomass or biogas) came from plant-based materials, the CO_2 produced during PMSR of biogas is considered to be part of nature's CO_2 circle where plants consume CO_2 from the atmosphere upon growth and elute CO_2 upon harvesting and consumption. The application of PMSR units can allow for the implementation of novel methods for small scale production and on-site carbon filtration, and capture. This would be beneficial to the environment and landfills alike—as the current method of converting the potent methane gas is complete combustion to CO_2 and water. Though CO_2 is 20 times less potent than methane, there is still a large loss in efficiency if the methane is simply burned. If a small portion of the energy stored in methane could be converted into hydrogen gas then this would aid in off-

setting the energy needs of the landfill and the surrounding operations, allowing for sustainable largely self-contained energy production.

The high heating value of hydrogen, 142.18 MJ kg^{-1}, compared to methanol, 22.88 MJ kg^{-1}, or gasoline[2], 46.54 MJ kg^{-1}, increases its desirability as an alternative fuel. Research and production of hydrogen fuel cells have been increasing over the last decade. However, its low energy density of 8.4 MJ L^{-1} (compared to 31.1 MJ L^{-1} for gasoline)[3] sparks the need to be able to derive hydrogen on-site from renewable sources. Though undesirable, a stationary fuel cell with a large footprint is acceptable, however, due to the low energy density of hydrogen, the widespread acceptance of commercialized hydrogen fuel cell vehicles and home power units will remain stagnant until two breakthroughs are achieved: find a way to produce the hydrogen in a renewable and cleanly manner, and secondarily, find a means to safely store the energy source (hydrogen or precursors) in a smaller volume.

1.2 Methane Steam Reforming

A majority of the current commercial hydrogen production is from endergonic processed that require high operational temperatures, such as the steam reforming of fossil fuel derived methane (natural gas). Figure 1 shows that of the hydrogen produced, 48% is produced by the reforming of natural gas.[4,5] Only 4% of the current hydrogen production is done so renewably. This high consumption of non-sustainable fuels to produce a sustainable fossil fuel alternative needs to be converted to a high consumption of renewable and sustainable hydrogen precursors in order to increase the beneficial effect of hydrogen gas as an energy carrier. This work focuses in the hydrogen synthesis route pertaining to the 0.1% of hydrogen production from other sources, **Figure 1.1**.

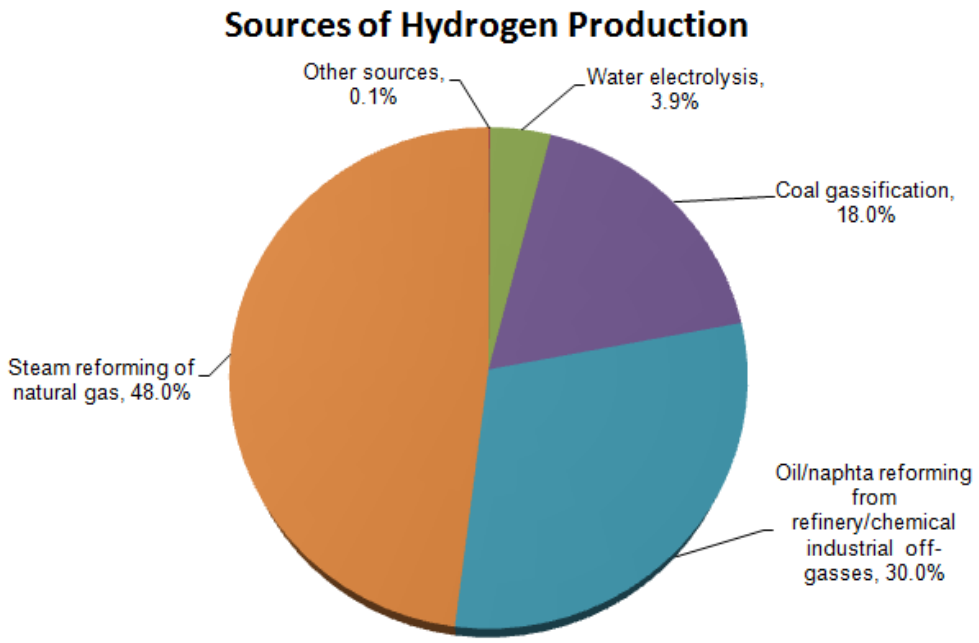

Figure 1.1 Sources of Hydrogen Production[4,5] in 2015

For every mole of methane reacted, either three moles of hydrogen and one mole of CO, or four moles of hydrogen and one mole of CO_2. With the product composition dependent on the initial methane to steam ratio.

Step 1

$CH_4 + H_2O \rightarrow CO + 3H_2$ ΔH°_R=206 kJ/mol, ΔG°_R=$^+$142 kJ mol^{-1}

Step 2

$CO + H_2O \rightarrow CO_2 + H_2$ ΔH°_R =-41 kJ/mol, ΔG°_R = -29 kJ mol^{-1}

Overall Reaction[6]

$CH_4 + 2H_2O \rightarrow CO_2 + 4H_2$ ΔH°_R =165 kJ/mol, ΔG°_R = $^+$113 kJ mol^{-1}

With a heat of reaction of 165 kJ mol^{-1}, and a free energy of 113 kJ mol^{-1}, methane steam reforming is a very endothermic and endergonic process. Due to this, the reaction must be carried out thermochemically at high temperatures, for instance many chemical reformers run at 900 °C and above with the aid of nickel based catalysts. Not only is the traditional synthesis of hydrogen gas derived from nonrenewable fossil fuels, it is also energy intensive. Although hydrogen is promoted as a green fuel, the current production is not currently a sustainable process. An aim of this thesis if to increase the sustainability of hydrogen gas by producing it from a renewable source (e.g. landfill derived methane) and using energy from sunlight to decreased the temperature of reaction.

1.3 Semiconductor

There are three basic classifications of solid materials: conductor, semiconductor, and insulator. Unlike conductors, both semiconductors and insulators have a discontinuous electron energy band. Of these bands the one lower in energy, where electrons sit at rest, is the valence band (VB); the band higher in energy, where electrons are excited to, is known as the conduction band (CB). The band gap energy (BGE) is the difference in energy between the VB and the CB. The BGE of an insulator is so large that an electron is not able to be excited from the valence band to the conduction band. In contrast, a semiconductor has a discontinuous electron band with a moderately sized band gap. The BGE gap is small enough that exposure to a certain amount of energy could excite the electron in the valence band to the conduction band. The energy to excite the electron from the VB to the CB must be equal to or greater than the BGE, for instance, a semiconductor with a BGE of 3.2 eV can only be excited by energy greater than 3.2 eV (i.e. orange visible light (625 nm) has an

energy of 2.0 eV and would not be sufficient to excite an electron from the VB to the CB). **Figure 1.2** illustrates how a semiconductor can be used in photocatalysis.

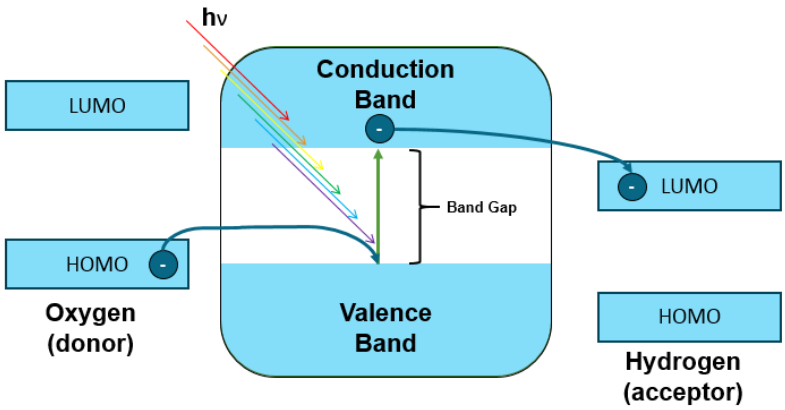

Figure 1.2 Electron-hole Pair Driving Oxidation and Reduction Reactions

As seen in **Figure 1.2**, upon illumination, the electron is excited from the valence band of the semiconductor to the conduction band, leaving behind a positively charged hole. The highest occupied molecular orbital (HOMO) of the electron donor (ie. the species being oxidized) must have a higher energy than the valence band of the semiconductor. The donor electron is transferred to the lower energy hole in the semi conductor's valence band. It follows that the lowest unoccupied molecular orbital (LUMO) of the electron acceptor (ie. The species being reduced) must be lower in energy than the conduction band of the semiconductor.[7] The electron from the conduction band of the photocatalyst is accepted in the lower energy hole in the LUMO of the acceptor. The valence and conduction band positions of TiO_2 meet these criteria for the steam reforming of methane and methanol to produce hydrogen gas. It is for this reason, among others, that titania based catalysts are studied in this work.

1.3.1 Direct vs. Indirect Semiconductor

Rutile TiO_2 is known to be a direct semiconductor, while anatase TiO_2 is known to be an indirect semiconductor. Direct indicates that the smallest energy difference between the minimal energy state in the conduction band and the maximal energy state in the conduction band is a direct path from the valence band to the conduction band, whereas indirect indicates that the smallest energy difference is not via a direct path, but rather an indirect path requiring a change in phonon energy, as depicted in **Figure 1.3**.

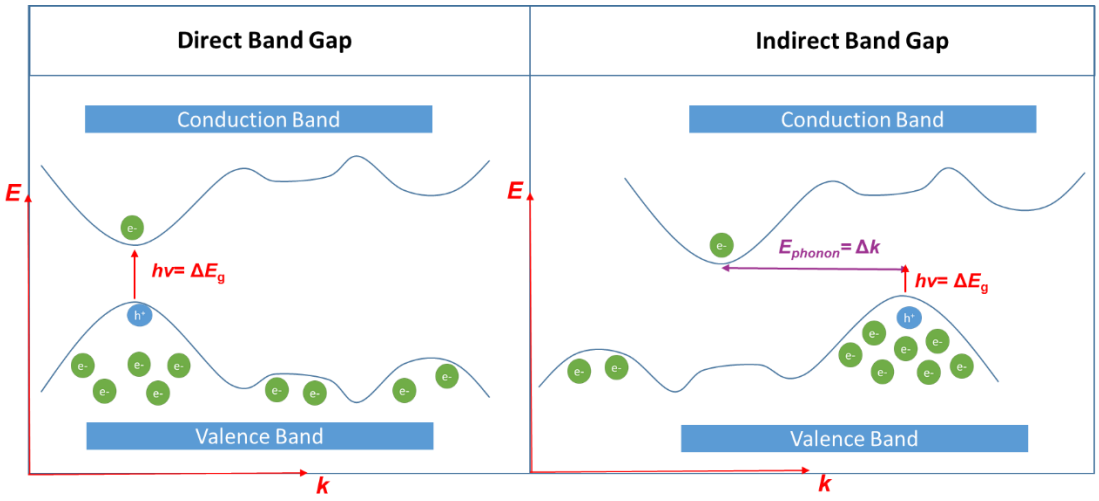

Figure 1.3 *E* vs *k* diagram of Direct and Indirect Band Gap Depiction

The *E* vs *k* diagram, drawn above, is used to attain information regarding the energy of specific orbitals along the *k*, where *k* is related to the momentum of an electron in the orbital of periodicity of e^{ikx}.[8] In essence, k represents the momentum of the electron where the minimum value of k is zero and the maximum value is π/λ. Therefore, when an electron is excited in a direct BGE semiconductor there is no change in momentum, but in an indirect semiconductor there is. The laws of conservation require that both charge and momentum be maintained such that the sum of the photon energy and the phonon energy is equal to that of the change in band gap energy.

$$E_{photon} + E_{phonon} = E_g$$

And therefore

$$\Delta k = \Delta k_{phonon}$$

The momentum change during the excitation of the electron in an indirect semiconductor must equal the phonon energy dissipated by a lattice vibration.

Since the electrons follow either a direct or indirect path during excitation the band gap must be measured for the correct band structure. In order to do so there is one method, the Tauc plot can be used to find both the direct and indirect BGE. When finding the indirect BGE one uses the square root of the Tauc equation, $Tauc^{½}$, whereas when finding the direct BGE one uses the square of the Tauc equation, $Tauc^2$.

1.3.2 Titanium Dioxide

Titanium Dioxide (TiO_2) is a photocatalytic semiconductor of interest due to its activity, stability, and low cost. [9,10] Unlike other photoactive semiconductors, such as zinc oxide or silicon dioxide, titanium dioxide remains stable at reaction temperatures and pressures and does not degrade. Additionally, titanium is desirable to use in as a sustainable catalyst since it is the ninth most abundant element in the Earth's crust.[11] The two main phases of TiO_2, rutile and anatase have cited BGE of 3.03 eV and 3.20 eV, respectively, which indicate absorbance of photons from ultraviolet light.[12] As most of incident solar radiation is visible light, we hypothesize that decreasing the band gap of TiO_2 will increase the efficiency of TiO_2 as a visible-light active photocatalyst. In order to more efficiently utilize solar radiation, we propose to modify the band gap of TiO_2 by manipulating the catalyst structure and composition via metal nanoparticle deposition, high temperature high pressure annealing for Ti^{3+} formation, and low pressure flame synthesis carbon doping.

Photons from ultraviolet sunlight excite electrons in the bulk of the semiconductor. As seen in figure 3, an electron, e^-, is excited from the valence band to the conduction band while simultaneously creating an electron hole, h^+, in the valence band.[13]

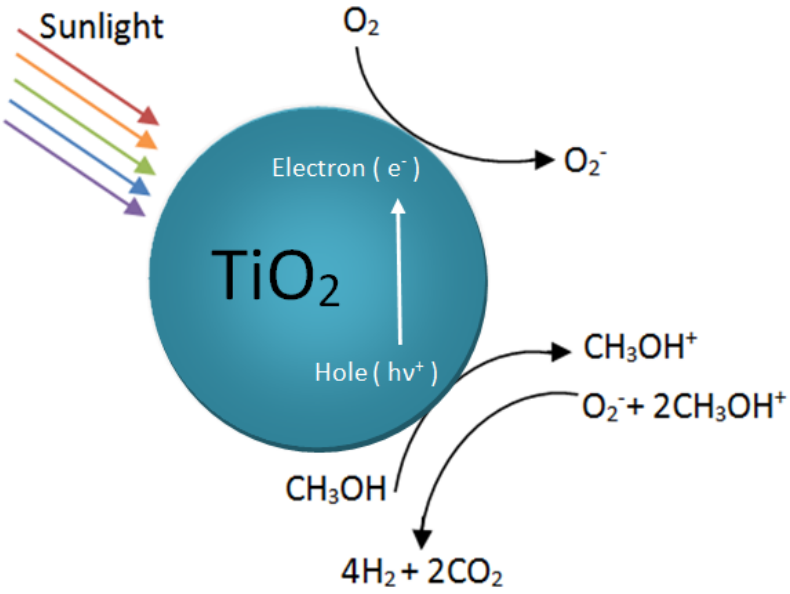

Figure 1.4 Titania Electron-Hole Depiction

In **Figure 1.4** the oxidized methanol reacts with the reduced dioxygen forming hydrogen gas as the desired product. The electron and hole separately diffuse to the surface of the TiO_2 particle and react with adsorbed molecules. On the surface of the particle, the electron hole is the source of the oxidation, while the electron is the source of reduction. In order for these reactions to occur charge separation must be maintained. If the electron and hole recombine in the bulk or on the surface, then no reaction takes place. It is hypothesized that supported metals act as electron traps and therefore supporting a small amount of metals on the surface of the TiO_2 will decrease the electron-hole recombination thus increasing the quantum photocatalytic efficiency of the photocatalyst.

1.4 Material Properties

1.4.1 Fermi Level

The Fermi level, also known as the fermi surface is the energy surface that separated the occupied and unoccupied quantum states at absolute zero while at T= 0 K there is a spread of vacant and occupied states near the Fermi Level, E_f.[14] All electron states that are significantly involved in electronic specific heat and electrical and thermal conductivities reside within the Fermi level of a metal. The fermi level of each of the supported metals are shown in **Table 1.1**.

Table 1.1 Fermi Level of Supported Metals[15]

Metal	**Fermi Level (eV)**
Copper	-7.0
Nickel	-7.4
Silver	-5.49

1.4.2 Benefit of supported metal on TiO_2

The ex situ samples are hypothesized to have a mixture of the metal and metal oxide supported on the TiO_2, where the amount of oxide is related to the oxophilicity of the metal. Post-reduction and post-passivation, the metal nanoparticles have a thin coating of oxide, protecting the metal bulk from oxidizing during reaction. Valence and conduction band positions of the various metal oxides are shown in **Table 1.2**.

Table 1.2 Valence and Conduction Band Positions (AVS)

Metal Oxide	Valence Band (eV)	Conduction Band (eV)	Band Gap (eV)
CuO	-6.66	-4.96	1.70
NiO	-7.5	-4.00	3.50
Ag_2O	-5.89	-4.69	1.20
anatase TiO_2	-7.41	-4.21	3.20

The positions of the valence and conductions bands of anatase TiO_2 and each supported metal oxide are depicted in **Figure 1.5**.

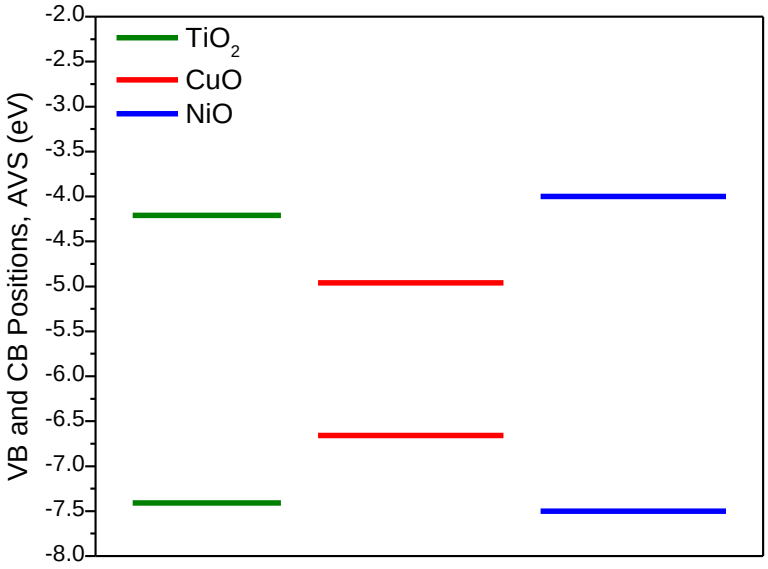

Figure 1.5 Valence and Conduction Bands of Supported Metal Oxides and TiO_2

In order for the metal oxide to be a good co-catalyst it is important that valence band of the supported metal oxide is more positive than that of TiO_2. This is because the TiO_2 valence band will act as an electron donor to the higher energy metal oxide valence band. The composite oxide will then have a smaller band gap than pure TiO_2 as the difference between the valence band of the supported metal oxide and the conduction band of the TiO_2 is less than the difference between the valence and conduction band of the TiO_2.

Post reduction and passivation, the potential change in the effective band gap is due to an interaction between the valence band of the TiO_2 and the Fermi level of the supported metal. A specific property of each metal, the Fermi level is the energy level at which an electron will rest at an elevated state. **Figure 1.6** depicts the Fermi levels of each supported metals in comparison to the valence and conduction band positions of anatase TiO_2.

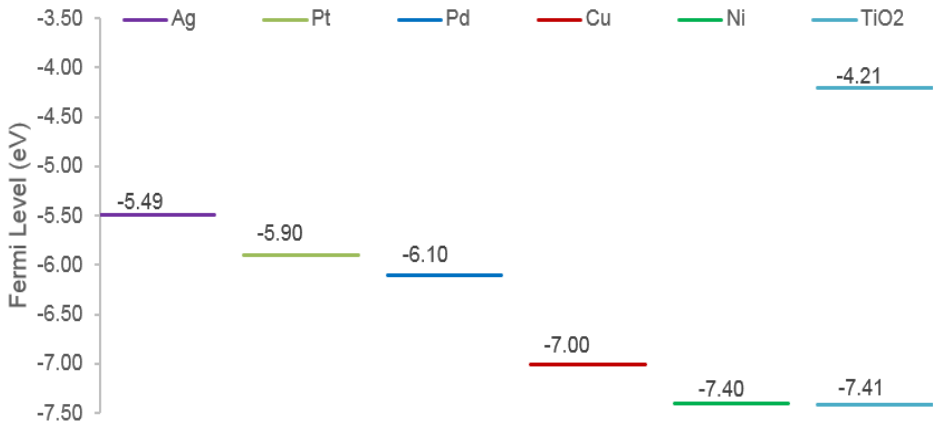

Figure 1.6 Fermi Level with TiO_2 Valence and Conduction Bands[16]

The effective band gap of the TiO_2 is reduced after metal modification due to the synergistic effect on electron density between the Fermi level of the metal and the valence band of TiO_2. The Fermi level of the supported metal must have a greater energy than the valence band of the TiO_2 support in order to provide the desired synergistic effect. Under these circumstances the electrons have a higher probability or resting at the Fermi level of the metal instead of the valence band of the TiO_2, thus decreasing the effective band gap of the semiconductor. The band gaps of the metal-modified samples post reduction and passivation will be measured as part of the proposed work.

1.4.2 Ti^{3+} Centers and Oxygen Vacancies

Titanium dioxide is primarily made up of titanium in the 4+ valence state and oxygen in the 2- valence state. However, Ti^{3+} centers in titanium dioxide can be caused by introduction of oxygen vacancies (V_o), hydrogenation of the Ti atoms, or by reduction of the Ti atoms, a schematic of which can be seen in **Figure 1.7**.

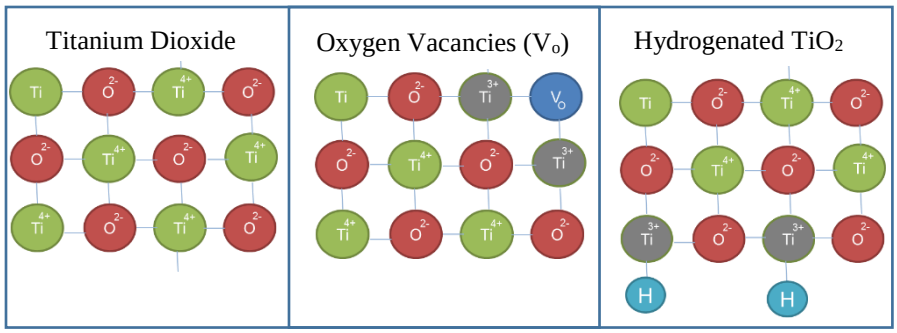

Figure 1.7 Schematic of TiO_2 with Ti^{4+} and Ti^{3+} Centers

Both Ti^{3+} centers and oxygen vacancies play an important role in the BGE. This is due to oxygen vacancies forming a donor level above the valence band and Ti^{3+} centers forming an acceptor level below the conduction band, **Figure 1.8**.

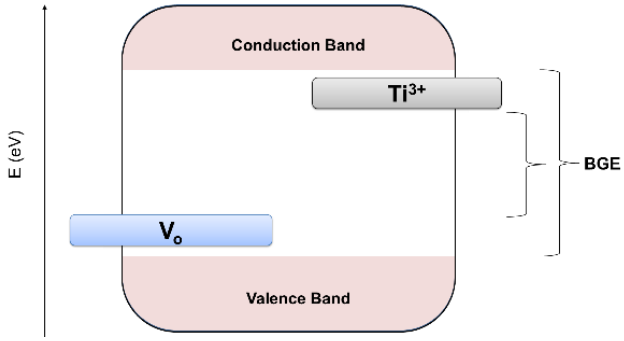

Figure 1.8 Ti^{3+} Centers and Oxygen Vacancies Effect on the BGE

The density of the Ti^{3+} centers and oxygen vacancies contribute to the net effect of the change in the band gap energy, as the densities approach the maximum the BGE approaches the energy difference between Ti^{3+} and V_o.

1.4.3 Anatase vs. Rutile

Industrially produced anatase nanoparticles are 25 nm in diameter while rutile nanoparticles average 200 nm in diameter. Particle size and charge carrier mobility within the bulk are important in determining efficiency losses due to bulk recombination. It has been shown that charge carriers excited nanometers deep in the bulk are able to reach the

surface to effect surface reaction, with maximum thickness of 2.5 nm and 5 nm for rutile and anatase films respectively.[17]

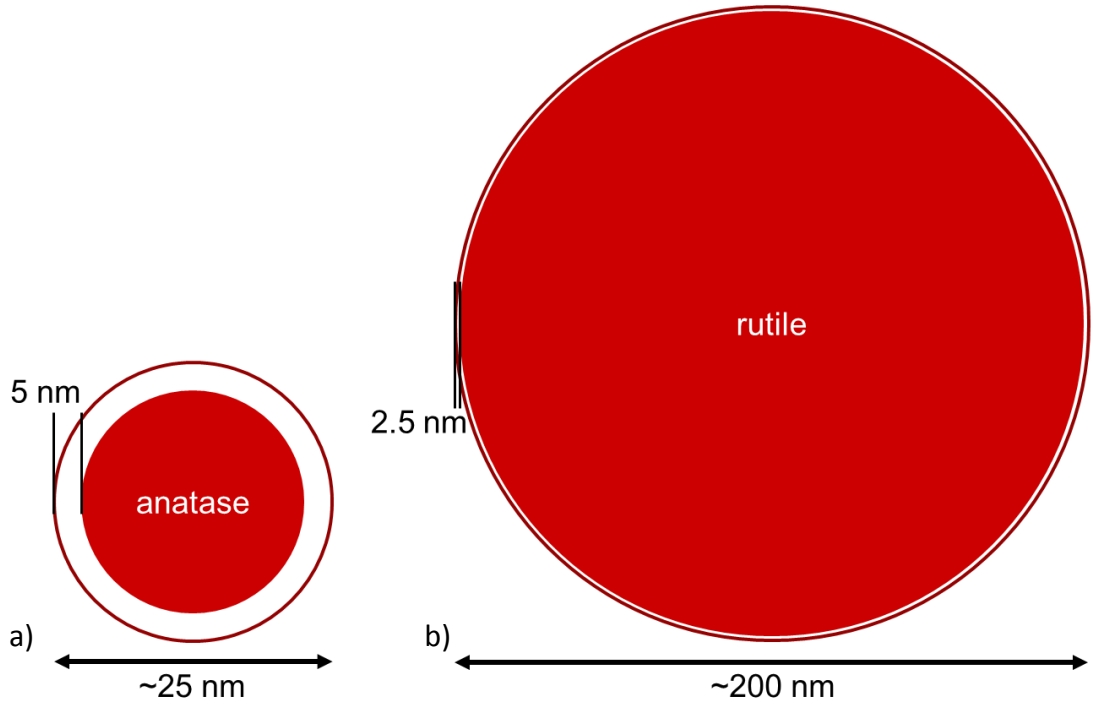

Figure 1.9 Exciton distance for a) anatase and b) rutile

Therefore, despite the larger BGE, anatase has a higher exciton mobility and is more photoactive than rutile. Due to its higher photoactivity we focus our studies on the anatase phase. We also aim to decrease particle size, d_p 10 nm, via low pressure flame synthesis such that the quantum efficiency of the excitons increases since a majority of the bulk excitons are lost in commercial anatase, d_p 25 nm.

1.4.4 Crystallite Size and the Quantum Confinement Effect

Decreasing particle size has the benefit of enhancing the photocatalytic activity due to the increasing ratio of surface to total atoms. The atoms on the surface provide locations for the surface redox reactions to occur indicating that the higher the ratio of surface atoms the higher the quantum efficiency of the photocatalyst. Decreasing the crystallite size also

causes various changes in the nanoparticle physical properties including an increase in surface area, an increase in internal pressure, and below the quantum confinement effect an increase in band gap energy. It has been noted that particles with a diameter of less than 10 nm fall below the quantum confinement effect.[8,18] As the particle size decreases so does the number of energy orbitals and therefore yielding a decrease in the confining dimension of the discrete energy orbitals. Due to this the fewer the number of TiO_2 molecules, the fewer the overlapping HOMO and LUMO orbitals forming the valence band and conduction band, respectively. Due to this, the band gap of a bulk material will widen until it reaches the energy difference between the HOMO and LUMO orbitals of an individual molecule, **Figure 1.10**.

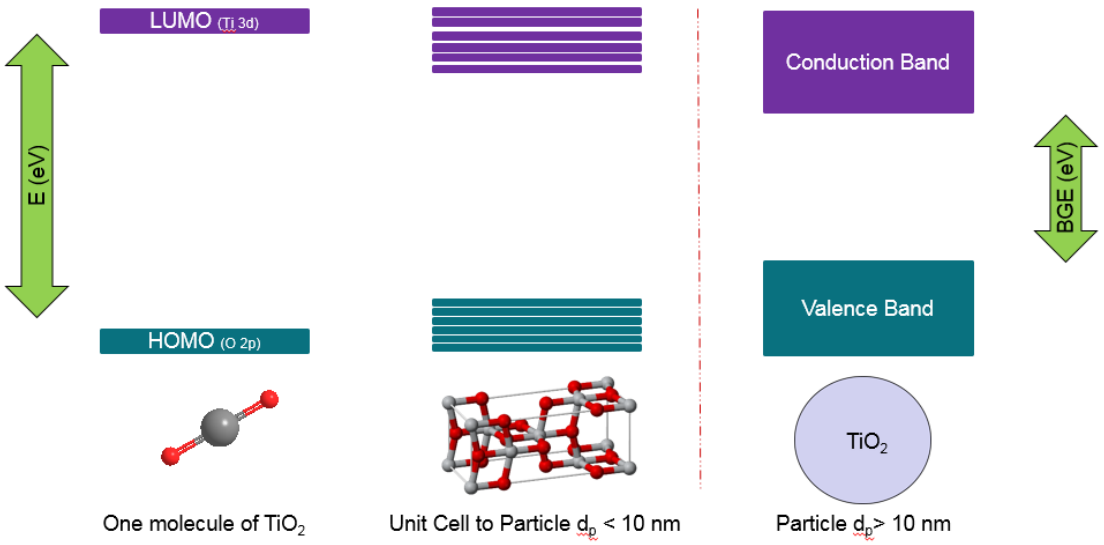

Figure 1.10 Schematic of Quantum Confinement Effect on TiO_2

This increase in band gap is undesirable since this leads to the photocatalyst using less of the available solar radiation. It is desirable to shrink the particle size to increase surface area for reaction and to increase quantum yield of the photo generated excitons, but a balance between particle size and band gap energy must be met. It is believed that

synthesizing particles with a crystallite size of 10 to 12 nm will exceed the quantum confinement limit yielding an acceptable BGE while also having a smaller particle size and therefore increased surface area and quantum efficiency when compared with conventional anatase.

1.5 Solar Spectrum

Of the solar irradiation that reaches earth's surface only 4% is ultraviolet light (UV), whereas 43% of the solar irradiation is visible light. Finding a photocatalysts that can efficiently use UV light and potentially harness some visible light would promote the viability of photocatalytic reactions. Figure 7 illustrates the intensity of the solar irradiation that reaches earth with respect to the wavelength of light.[19] The peak of spectral irradiance is near 500 nm.

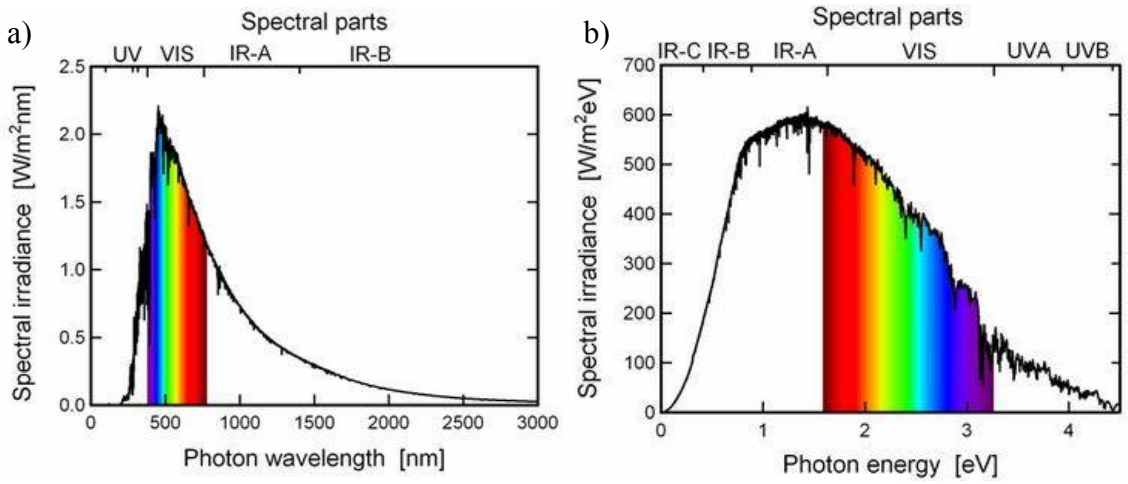

Figure 1.11 Solar Irradiation a) spectral irradiance vs wavelength, and b) spectral irradiance vs photon energy[19]

The visible region (400 nm to 700 nm) is shown via the overlay of colors that correspond to each wavelength. **Figure 1.11** depicts the spectral irradiance versus the photon energy.[19] Though compared to visible light photons UV light photons have much

higher energy, 3.1 eV to 6.2 eV, they are much less abundant than photons from visible light, compromising of only 4% as opposed to the 43% of the solar spectrum which is visible.

It can be noted that a large percentage of energy derived from solar irradiation is unusable for unaltered TiO_2 due to the large BGE. **Figure 1.11** aids in visualizing that the electrons in a semiconductor with a band gap less than 3.0 eV would be excited by a portion of the photons derived from visible light as well as photons from UV light. Due to the addition of excitable photons by decreasing the necessary energy, it is expected that increasing the photocatalytic efficiency will aid in photocatalysis Modifications will be done via High Pressure High Temperature Annealing, Low Pressure Flame Synthesis carbon doping, and supporting metals, specifically nickel, on anatase TiO_2.

1.5 Objectives

- Elucidating structural and compositional polymorph changes of multi-phase semiconductors in situ and ex situ using a quick and quantitative manner. Derivative peak fitting of diffuse-reflectance UV-visible spectra (DPR) is presented as an inexpensive, fast and quantitative method to estimate both the composition of a multi-phase semiconductor sample as well as the band gap energies of each component semiconductor in the mixture.
- Generating stable Ti^{3+} defects for the precious metal free generation of hydrogen gas from photocatalytic methane steam reforming (MSR) via High Temperature High Pressure annealing (HPHT) of anatase TiO_2

- Increasing photocatalytic hydrogen production under UV and broad spectrum illumination while decreasing coke formation at low steam to carbon ratios via combining a nickel metal cocatalyst and HPHT anatase TiO_2.
- Synthesis and analysis of high surface area, carbon doped, low pressure flame synthesized anatase TiO_2 via low pressure flame synthesis with a premixed flat flame for increased efficiency in photocatalytic applications, namely water reduction.

Chapter 2: Preparation and Analysis Techniques

2.1 Calcination Procedure

The pre-cleaned quartz boats were filled two thirds full with titania powder (*Acros Organics*). One to two boats were loaded into an inch outer diameter quartz tube with a thickness and a length of 1/8 inch and 31 inches, respectively. The loaded quartz tube was slid through the furnace opening and supported on each end by ceramic supports. The ends of the tube were fitted with UltraTorr® fittings. The upstream side of the tube was connected to the air cylinder, while the downstream side was connected to an air lock. The air purged the quartz tube at 100 ml/min while the furnace heated to 773 K at a ramp rate of 2 K per minute. The furnace temperature was maintained at 773 K for 3 hours. After 3 hours, the furnace cooled to room temperature at a ramp rate of 10 K per minute under constant air flow. The calcined titania sample was transferred to a glass vial and stored in a desiccator.

2.2 Pore Volume Measurement

The calcined anatase TiO_2 was used as a semiconductor support for various metals. All metal supported samples were synthesized via incipient wetness impregnation (IWI). Before beginning IWI, the pore volume of the support relative to the solvent in which the metal salt is dissolved (Water or Toluene) had to be determined. In order to check the pore volume 1.0 gram of support was massed, a capped vial of solvent was weighed and tared. The desired solvent was added drop wise to the support while the support was constantly stirred with a spatula. This process continued until the incipient wetness point was reached. The incipient wetness point can be identified visually when the support began to glisten, but before the support was completely wet. The difference in weight of the solvent vial

before and after IWI gave the mass of solvent to attain the incipient wetness point of the support. The mass of solvent used was converted to volume using the solvent's density. This volume was then divided by the sample mass to attain the pore volume. This process was repeated until an average value of the pore volume, with an acceptable relative standard deviation, RSD $\leq$ 5.0%, was measured.

2.3 Incipient Wetness Impregnation

All metal supported on TiO_2 were synthesized with calcined TiO_2. The TiO_2 was calcined in a tube furnace at 773 K. Incipient Wetness Impregnation (IWI) is a method used to modify the $_{TIO2}$via supporting metals on the $_{TIO2}$nanoparticles. During IWI, a desired mass of calcined $_{TIO2}$support was measured out. The mass of solvent needed was determined via the calculated pore volume of the support. A vial of the required mass of solvent was prepared. The mass of metal salt needed to achieve the desired loading weight percent was determined via the weight percent of the metal in the salt and the mass of support. The desired amount of the metal salt was added to the solvent vial. Once the metal salt had completely dissolved, the solution was added to the support drop wise under constant stirring until the incipient wetness point was reached. The sample was dried in the oven 24 hours at 883 K. After 24 hours, the sample was removed from the oven and scraped into a mortar for grinding. The sample was lightly ground with a mortar and pestle until it appeared homogeneous. The ground sample was stored in a vial in the desiccator until calcination.

2.4 Reduction and Passivation

Prior to conducting the methanol conversion reaction, each calcined metal-modified TiO_2 sample was reduced in situ. Each sample was reduced under separate conditions pertaining to the oxophilicity of the supported metal (**Table 2.1**).

Table 2.1 Reduction Conditions for Various Supported Metals

Metal	Temperature (K)	Time (hours)	Percent H_2 in N_2 (%)	Ramp Rate (K min^{-1})	Total Flow Rate (ml min^{-1})
Cu	473	2	10	2	50
Ag	473	2	10	2	50
Ni	773	5	5	2	50

Copper modified TiO_2 samples were reduced at 473 K for 2 hours at a ramp rate of 2 K per minute under 50 ml/min of 10% H_2 in N_2 [20]. Silver modified TiO_2 was reduced at 473 K for 2 hours at a ramp rate of 2 K per minute under 50 ml/min of 10% H_2 in N_2. Platinum and Palladium modified TiO_2 samples were reduced at 573 K for 5 hours at a ramp rate of 2 K per minute under 50 ml/min of 5% H_2 in N_2 [21]. Nickel modified TiO_2 samples were reduced at 773 K for 5 hours at a ramp rate of 2 K per minute under 50 ml/min of 5% H_2 in N_2 [21]. After reduction, each metal modified catalyst was passivated in situ under 50 ml/min of 2% O_2 in N_2 [20].

Supporting metal nanoparticles on TiO_2 creates a synergistic effect which helps to both raise the effective position of the valence band, decrease the effective band gap, and aids in maintaining electron electron-hole charge separation. Absorbance and band gap measurements of each of the metal modified catalysts were taken both ex situ (post calcination or post HPHT), and in situ (post reduction and passivation).

2.5 UV-Visible Spectroscopy

The ex situ micro sample cup (fill volume of 0.022 ml) was weighed and tared. The plastic filling funnel was placed on top of the micro sample cup, and a small amount of catalyst sample was placed in to the funnel. The funnel was held in place while gently tapping the micro sample cup against the lab bench in order to lightly pack the sample. The funnel was then removed from the micro sample cup and the sample was smoothed by scraping off the excess sample and pressing down with the spatula end of the flattening tool. The process was repeated until the sample was smooth and flush to the micro sample cup edge. The excess powder was wiped from the sides and base of the sample cup with a Kimwipe•. The sample cup was weighed and the mass of the sample was recorded. The bulk density of the catalyst is obtained by dividing the mass of the sample in the micro sample cup by the fill volume.

2.5.1 Diffuse Reflectance

Both Specular and Diffuse reflectance measure the light reflected from a sample, as opposed to transmitted light, as seen in **Figure 2.2**. Diffuse reflection is used when the surface consists of small particles that scatter light diffusely, such that the mirror-type reflection seen in specular reflectance does not exist.[22]

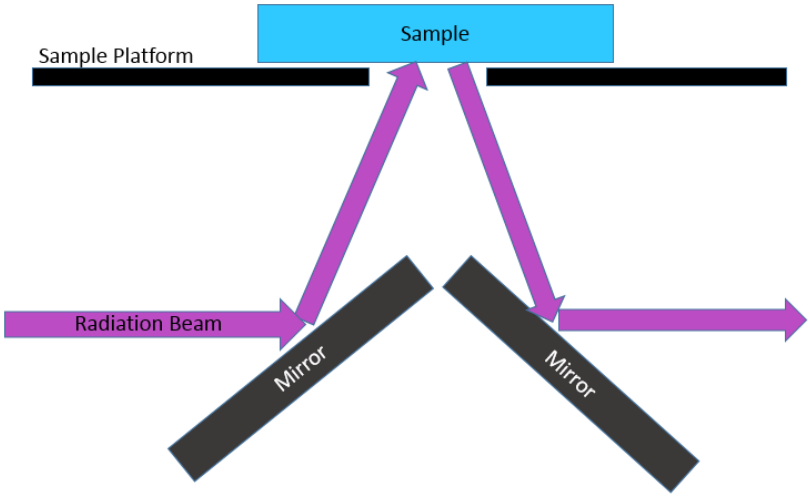

Figure 2.1 Diffuse Reflectance UV-Visible Spectroscopy Schematic

Diffuse reflectance of a sample can be measured either ex situ with the micro sample cup, or in situ in the HVC-Diffuse Reflectance Reactor. Both in situ and ex situ methods use the sample platform in the Praying Mantis Diffuse Reflectance Accessory (*Harrick Scientific*) in the Evolution 300 UV-Visible Spectrophotometer.

2.5.2 Kubelka Munk Units

For diffuse reflectance, Kubelka Munk Units (KMU) are analogous to absorbance. The KMU equation, $F(R)$, was calculated by converting percent reflectance spectra obtained from the UV-Visible Spectrophotometer to absolute reflectance, R_∞. The absolute reflectance is calculated by dividing the percent reflectance of the sample by the percent reflectance of an absolute reference, the Spectralon® disk.

$$R_\infty = \frac{\%R_{Sample}}{\%R_{Spectralon}}$$

The Spectralon® disk is an absolute reference for diffuse reflectance and therefore has a diffuse reflectance of unity, thus converting percent reflectance of a sample to

absolute diffuse reflectance. The absolute reflectance is then used to calculate the KMU function, $F(R)$.

$$F(R) = \frac{(1 - R_\infty)^2}{2R_\infty}$$

The KMU function is the square of the difference between unity and the absolute reflectance divided by the quantity two times the absolute reflectance. It is a function of absolute reflectance, and therefore the wavelength of irradiated light. Since various factors- including absorbance, particle size, bulk density of the particles, and smoothness of surface- affect the magnitude of $F(R)$, the normalized KMU is the plotted when comparing different samples. Normalized KMU is obtained by dividing $F(R)$ by the maximum value of $F(R)$.

2.6 Electron Paramagnetic Resonance

Electron Paramagnetic Resonance (EPR) is a technique that measures the Zeeman effect: the interaction between an unpaired electron in the sample and the induced magnetic field, B_0.[23] Quantitative Continuous Wave (CW) EPR measurements allows for accurate spin counting leading to quantification of measured states. The work presented in this thesis used $CuSO_4$ as a spin standard for CW EPR.

A single unpaired electron has only two allowed states, the lower energy state (M_s = -1/2) where the electron magnetic moment, μ, is aligned with the magnetic field, B_0 (parallel), and the higher energy state (M_s = +1/2) where the electron magnetic moment, μ, is aligned against the magnetic field, B_0 (antiparallel). The difference in energies of these two states, ΔE, is defined by

$$\Delta E = g\ \mu_B\ B_0\ \Delta m_s = \ g\ \mu_B\ B_0$$

Where μ_B, is the Bohr magneton (natural unit of electron's magnetic moment), g is the g-factor. The g-factor is independent of the microwave frequency is used to identify signals.[23] Thus, the energy difference is linearly dependent on the magnetic field such that when no magnetic field is applied the electron is only in the low energy state. A constant microwave frequency while varying the magnetic field was used to obtain CW spectra. The concentration of unpaired electrons in the sample in a specific environment is proportional to the integrated intensity of the EPR signal.

It is important to keep as many parameters the same between experiments due to the susceptibility of the signal intensity to change when varying parameters. The signal intensity is proportional to the square root of the microwave power (at low power levels used in this work). EPR spectra were recorded on a Bruker ESP300 equipped with an Oxford helium cryostat model 900 under the direction of Dr. Alexei Tyryshkin in the laboratory of Prof. G. Charles Dismukes, **Figure 2.2**.

Figure 2.2 Electron Paramagnetic Resonance Spectrometer Setup

The moments are randomly distributed between parallel and antiparallel states with a slightly higher concentration in the parallel (lower energy) state, thus following Boltzman Statistics:

$$\frac{n_{antiparallel}}{n_{parallel}} = e^{-\left(\frac{\Delta E}{kT}\right)}$$

On average the difference of population between the parallel and antiparallel state is 0.08%, under the same field strength the difference in population in Nuclear Magnetic Resonance (NMR) is roughly 600 times smaller. Due to this increase in difference of populated states EPR measurements can be obtained at lower spin concentrations than NMR.

Applying a magnetic field disrupts this population balance and therefore the electrons are no longer in thermal equilibrium due to the absorption of the microwave energy which heats up the spin system. When the system returns to thermal equilibrium via interaction with its surroundings spin-lattice relaxation occurs. Temperature of the sample bed is controlled in order to prevent large spin lattice relaxation in the samples. A helium cryostat was used to maintain the temperature between 12 K and 100 K depending on the element being studied.

2.6.1 Metal Supported: Hyperfine

The hyperfine interaction, the interaction between the electron and the nuclei (which has a magnetic moment) can be used to characterize the samples, such as the Cu^{2+} hyperfine. The EPR absorption signal for an electron interacting with a nucleus of spin ½ splits into two signals, each B_I away from the original signal, where B_I is the magnetic field at the electron. The spacing between the two hyperfine signals, $2B_I$ is dubbed the hyperfine

splitting constant, a_H. The number of hyperfine lines is equal to $2nI$ +1 where I is the nuclear spin and n is the number of symmetry equivalent nuclei. Copper has two abundant isotopes, ^{63}Cu and ^{65}Cu.[24] Both isotopes have a nuclear spin of 3/2, therefore coupling to 1 cu ion gives four hyperfine lines. Though ^{63}Cu has a magnetic moment of μ=2.2233 (69.17%) and ^{65}Cu (30.83%) has a magnetic moment of μ=2.3817 (Winter, 2017) thus the hyperfine lines of ^{63}Cu will appear larger and at a lower field energy than those of ^{65}Cu.

Chapter 3: Unraveling the Phase Composition of Metal Oxide, Degussa P25 TiO_2 via Derivative Peak Fitting of Differential Diffuse Reflectance

3.1 Introduction

Titanium Dioxide (TiO_2), a metal oxide semiconductor, is of particular interest in catalysis as a support for metal nanoparticles due to its abundance, stability under reaction conditions, high surface area and band positions that are well-matched with the redox potential of hydrogen evolution making it an interesting catalyst for water splitting and methane conversion.[25-27] As mentioned in section 1.4, the two most common polymorphs of TiO_2, anatase and rutile have cited electronic band gap energies (BGE) of 3.20 eV and 3.03 eV respectively,[28] indicating that they absorb primarily ultraviolet light. Anatase and rutile have been studied for photocatalytic activity both individually and as mixed-phase formulations.[26,29-31] Degussa P25 TiO_2 is a widely-used mixed-phase TiO_2 catalyst [25-26,32-34] with a marketed anatase to rutile weight ratio of 80/20.[35] The actual ratio of anatase and rutile, as well as the presence of amorphous TiO_2 is variable between batches of the material.[36-39] Many studies have shown that mixed-phase TiO_2 exhibits increased photocatalytic properties due to the synergistic effect between anatase and rutile, as mentioned in Chapter 1.[25-26, 40-41] The increased absorbance in the ultraviolet region of the spectrum for the mixed polymorph structure is attributed to the synergistic effect between the anatase and rutile band edges. P25 and mixed phase TiO_2 have been extensively studied via many techniques including X-ray powder diffraction (XRD),[36-39,40-42] Raman spectroscopy,[42-45] electron paramagnetic resonance,[26,46] X-ray photoelectron spectroscopy (XPS),[47] and molecular dynamics simulations.[30,48] Of these, XRD and Raman are able to quantify the polymorph composition of a sample, with XRD being a standard method for

quantification; both techniques usually require costly instrumentation and specialized training to obtain this information. Due to the scale at which semiconductor nanoparticles are utilized in research and in industry, the ability to analyze and quantify polymorph compositions quickly and thoroughly is important to catalyst manufacturers and users alike.[49]

UV-Visible spectroscopy is an inexpensive, quick, and readily available technique requiring minimal training. As the optical band gap of TiO_2 and many other semiconductors lies in the ultraviolet and visible light range, UV-visible spectroscopy has been used for decades to characterize BGEs. Since the first publication by Tauc, Grigorovici and Vancu[50] in 1966 and further development of the method by Davis and Mott[51] in 1970, the Tauc method has become the field-standard to analyze the optical absorbance of semiconductors using diffuse reflectance UV-Visible spectroscopy. The versatility of the Tauc method is demonstrated in its ability to calculate the energy profile for both the allowed direct transition ($Tauc^2$) and the allowed indirect transition ($Tauc^{½}$). The Tauc plot is an s-shaped curve where the BGE is determined by the x-intercept of the line tangent to the inflection point. In a more accurate approach, the inflection point should be found by taking the first and second derivatives of the curve and defining the x-intercept of the second derivative as the tangent point while using the first derivative value at the tangent point as the tangent slope. Extrapolation of the line tangent to the inflection point allows for the calculation of the BGE. A simpler method is often used at the expense of accuracy, wherein a tangent line is semi-arbitrarily drawn in the linear region of the Tauc curve. This approach can lead to large variations in the calculated BGE.[52] When using this method, one must justify the linear region, and depending on the shape and magnitude of

the low-energy tail this justification can change between both samples and analysts.[53] Recently, methods to determine the BGE, specifically the Tauc method, have received scrutiny due to the precision and variability in which the inflection point is chosen and therefore the variability of the determined BGE.[52-55] Many papers concerning the optical and photocatalytic properties of TiO_2 utilize the Tauc plot, though few justify the position of the tangent line.

A further limitation of the Tauc method is that it assumed that the sample under analysis possesses a single band gap. Due to the method of analysis, applying the Tauc method to calculate BGE for mixed-phase semiconductors could lead to erroneous results, especially if the BGE of the multiple phases are close together. This can be seen in the determination of one BGE for P25 whereas it truly has multiple BGE values, one for each phase. To address this issue an alternate method is necessary that can simultaneously measure the BGE values for the different phases or polymorphs present in mixed-phase semiconductors, such as P25.

Differential diffuse-reflectance UV-visible spectroscopy – taking first (or higher order) derivatives of the diffuse reflectance spectra or Kubelka-Munk units – has been used previously to identify the polymorphs present in mixed-phase TiO_2 samples.[55–58] The BGE of anatase has been determined from the local maxima of the first derivative of diffuse reflectance spectra,[52] with favorable comparison to Tauc method results. While differential spectroscopy has been used in analytical chemistry for quantitative analysis in transmission spectroscopy of solutions,[59-61] the authors were unable to find prior work showing that differential spectroscopy can quantify the amounts of different solid components in a mixture by diffuse-reflectance spectroscopy.

The present work establishes that peak-fitting of differential diffuse-reflectance UV-visible spectra (DPR) can be used to quantitatively measure the crystalline composition of mixed-phase TiO_2. With a single measurement, both the mass fraction and BGE of each polymorph present can be determined. Using this technique, the phase behavior of P25 subjected to different common pretreatment methods is described. As-received P25 samples were subjected to grinding, sieving, and calcination treatment, and a combination of these operations. The phase composition and BGE were measured via DPR, XRD, and Raman. Grinding and sieving samples prior to calcination played an important role in the onset temperature for rutilization. The onset temperature for rutilization of as-received P25 was just above 823 K. Grinding and sieving (between 45 μm and 53 μm) lowered the onset temperature of rutilization to 673 K, while dramatically reducing the overall amount of rutilization taking place at 973 K. This reveals that properties of P25 vary significantly with different pretreatment conditions, and indicates that care should be taken to distinguish between materials derived by pretreatment and modification of P25 and the parent material itself. The quantitative success of the DPR method in this study may lead to application in other systems of mixed semiconductors.

3.2 Experimental Methods

3.2.1 Sample Preparation

Anatase TiO_2 (98+%) and rutile TiO_2 (>95% rutile) were obtained from Acros Organics. Degussa P25 TiO_2 (Lot: 613020598) was obtained from Evonik and subjected to grinding, sieving, calcination, or a combination of these pretreatment techniques. **Table 3.1** summarizes the combinations of pretreatment operations performed on each sample. Grinding was performed using an agate mortar and pestle, applying approximately 200 kPa

of pressure during grinding for 5 minutes. Metal wire sieving trays with mesh sizes of 45 μm and 53 μm were used to sieve samples into agglomerate particle sizes with diameters between 45 μm and 53 μm (S50).

Table 3.1 Naming convention, pretreatment conditions, and order of operations for P25 samples.

Sample ID	Ground	Sieved	Calcined	Order of Operations
P25				(as-received)
C300			573 K	Calcined
C500			773 K	
C700			973 K	
G-P25	yes			Ground
G-C300	yes		573 K	Ground, Calcined
G-C500	yes		773 K	
G-C700	yes		973 K	
S50		45 μm $<d_p<$53 μm		Sieved
S50-C500		45 μm $<d_p<$53 μm	773 K	Sieved, Calcined
G-S50	yes	45 μm $<d_p<$53 μm		Ground, Sieved
G-S50-C500	yes	45 μm $<d_p<$53 μm	773 K	Ground, Sieved, Calcined

Calcination was performed in a Thermo Scientific Lindberg Blue tube furnace equipped with multi-step ramp-soak program functionality. Sample powders were loaded into quartz boats and placed inside a 2.54 cm OD quartz tube 79 cm long. The ends of the tube were fitted with UltraTorr® fittings to connect the upstream side to an air cylinder and the downstream side to a purge line. Air was flowed through the tube at 100 ml min^{-1} with a ramp rate of 2 K min^{-1} followed by a 3 hour hold at the desired calcination temperature. The furnace was then cooled to room temperature at a ramp rate of 10 K min^{-1} under constant air flow.

3.2.2 X-Ray Powder Diffraction

X-ray powder diffraction patterns were collected using a PANalytical Philips X'Pert X-ray diffractometer, and analyzed to determine crystallinity and phase

composition. The XRD measurements were carried using a Cu Kα source at 40 kV and 40 mA and angular incidence 2θ between 20° and 80° with a 0.05° step and 3.0s/step for a scan speed of 0.0167 °/s. Composition of samples was analyzed using a whole pattern fitting with Pearson-VII profile shape function using PDF# 01-073-1764 and PDF# 01-078-1510 for anatase and rutile, respectively. XRD patterns were background subtracted with a medium cubic spline with a $K\alpha_1/\alpha_2$ ratio of 3.3. Relative phase composition and corresponding error were determined via a whole pattern fitting (WPF) and Rietveld refinement where the refinement was halted to a %R below 15%. Percent error in relative composition was determined during the WPF refinement using peak width as a measure of precision as well as the number of peaks participation in the error equation. This error was then scaled during the refinement by the overall relative composition of the specific phase in the sample. Apparent crystallite size was determined during WPF refinement while removing instrumental contribution.

3.2.3 Raman Spectroscopy

A Horiba Scientific LabSpec HR Raman spectrometer was used to collect all Raman spectra. The instrument was equipped with a 532 nm solid state laser source and a 10× objective was used for focusing the incident beam. For each spectrum, 3 accumulations were used with the acquisition time between one and ten seconds depending on sample. All the Raman spectra were taken at room temperature and the laser power onto the sample did not exceed 5mW to avoid overheating.

3.2.4 UV-Visible Spectroscopy

Diffuse-reflectance UV-visible spectroscopy was carried out in a Thermo Scientific Evolution 3000 spectrophotometer equipped with a Harrick Scientific Praying Mantis

diffuse reflectance accessory. The spectra were collected between 300 nm to 600 nm in intervals of 0.5 nm. Ex situ diffuse reflectance spectra were collected by loosely filling a micro sample cup (0.022 ml), with excess powder scraped off to ensure a full sample cup with a flat surface. The bulk density of each sample was determined by dividing the mass of the sample in the micro sample cup by the fill volume. A Spectralon® disk was used as the absolute reflectance standard.

Diffuse-reflectance spectra of samples at elevated temperatures while exposed to different atmospheres (i.e. in situ conditions) were acquired using a Harrick High Temperature Reaction Chamber equipped with three quartz windows, temperature control via electrical heating cartridge and K-type thermocouple, and high-pressure dome.

3.2.5 Derivative Peak Fitting of Diffuse Reflectance Spectra

The first derivatives of the absolute reflectance were calculated by taking the instantaneous slope of the reflectance with respect to wavelength at each data point in the original spectrum.

$$\frac{dR_\infty}{d\lambda} = \frac{R_{\infty i} - R_{\infty i+1}}{\lambda_i - \lambda_{i+1}} \quad (1)$$

The deconvolution and peak fitting of spectra was carried out using Fityk software.[62] The peaks in the derivative spectra were fit to Gaussian functions, with one Gaussian per phase present by minimizing the weighted sum of the square residuals using the Levenberg-Marquardt method. In all samples, no more than two phases were present. Additional functions added to the fitting did not improve the quality of the fit and were therefore not considered. Mathematically, a Gaussian function, g(x), is an exponential function given by equation (2), where a, b, and c are constants.

$$g(x) = ae^{-(x-b)^2/(2c^2)} \quad (2)$$

Absolute reflectance measures the excitation of electrons from the ground state (valence band and fermi level) to the exited state (conduction band). Integrating the derivative of the absolute reflectance yields the population of electrons excited by all photons with energy less than the limits of the integral. The concentration of electrons in the conduction band, $n_{c,}$ is proportional to the exponential of the difference between the fermi level, E_F, and the conduction band energy, E_c, as shown in equation (3),[63] where N_c is the total density of the electrons in extended states, and k_BT is thermal energy.

$$n_c = N_c e^{(E_F - E_c)/k_B T} \quad (3)$$

As the mathematical form of equation (3) resembles a Gaussian function, Gaussian functions were chosen to fit the peaks in the deconvolution of the derivative of the reflectance spectra of anatase and rutile semiconductors. The BGE of each phase present was determined from the peak center position of the Gaussian function, which corresponded to the inflection point of the optical reflectance spectrum.

The absolute response factors (ARF) for anatase and rutile for diffuse reflectance were not known a priori, and a relative response factor (RRF) for diffuse reflectance between the two phases was obtained via linear regression of samples of known mass fraction. Assuming that anatase and rutile each possess a unique absolute response factor corresponding to a specific peak area (PA_i) per mole of TiO_2 (ARF_i,= $PA_i/mole_i$), the mass fraction in the mixture of the two phases can be obtained by (4), were A = anatase, R = rutile, and RRF = ARF_R/ARF_A. The equation simplifies as the molecular weights of anatase and rutile TiO_2 are the same.

$$\frac{\text{wt\%}_{\text{anatase}}}{100} = \frac{\text{mole}_A \cdot \text{MW}_A}{\text{mole}_A \cdot \text{MW}_A + \text{mole}_R \cdot \text{MW}_R} = \frac{\frac{\text{PA}_A}{\text{ARF}_A}}{\frac{\text{PA}_A}{\text{ARF}_A} + \frac{\text{PA}_R}{\text{ARF}_R}} = \frac{\text{PA}_A \cdot \text{RRF}}{\text{PA}_A \cdot \text{RRF} + \text{PA}_R} \quad (4)$$

The value of RRF was determined from peak area measurements for a series of anatase/rutile mixtures of known composition. Using linear regression, a value of RRF = 1.34 was found to minimize the residuals between the calculated and known mass fractions of anatase in the mixtures. That RRF > 1 indicates that the response factor for rutile is stronger than that for anatase.

3.3 Results and Discussion

3.3.1 Limitations of the Tauc Method

The UV-Visible diffuse-reflectance spectra of commercially obtained samples of anatase and rutile powders were collected and compared to the spectrum of P25. These are plotted using the Tauc method in Figure 3.1. The indirect BGE values were obtained by (5), where $F(R_\infty)$ is the Kubelka-Munk function and $E(\lambda)$ is the photon energy at the specific wavelength.

$$Tauc^{1/2} = \sqrt{F(R_\infty) \cdot E(\lambda)} \quad (5)$$

The apparent band gap energies of the three samples were obtained by calculating the location of the inflection point and the slope of the tangent line using the first (6) and second derivatives (7) of the Tauc function.

$$\frac{d(Tauc^{1/2})}{d\lambda} = \frac{\sqrt{F(R_{\infty i}) \cdot E(\lambda_i)} - \sqrt{F(R_{\infty i+1}) \cdot E(\lambda_{i+1})}}{\lambda_i - \lambda_{i+1}} \quad (6)$$

$$\frac{d^2(Tauc^{1/2})}{d\lambda^2} = \frac{\left(\frac{d(Tauc^{1/2})}{d\lambda}\right)_i - \left(\frac{d(Tauc^{1/2})}{d\lambda}\right)_{i+1}}{\lambda_i - \lambda_{i+1}} \quad (7)$$

The resulting BGEs for pure anatase and rutile, 3.22 eV and 2.98 eV respectively, were in good agreement with literature values of 3.20 eV and 3.03 eV, as discussed in chapter 1. [28]

This method predicts a single BGE of 3.27 eV for P25, despite the fact that P25 is a mixed-phase material and therefore is expected to possess two BGEs – one for each phase. The application of the Tauc method to a multi-phase spectrum results in a tangent line intersects the curve formed by the data twice – once at the tangent point and again at 4.04 eV, which is inconsistent with a semiconductor band-edge electronic excitation model. Despite these limitations, single-valued BGEs for P25 have been reported previously, often with the caveats listed above, such as a value of 3.15 eV.[28]

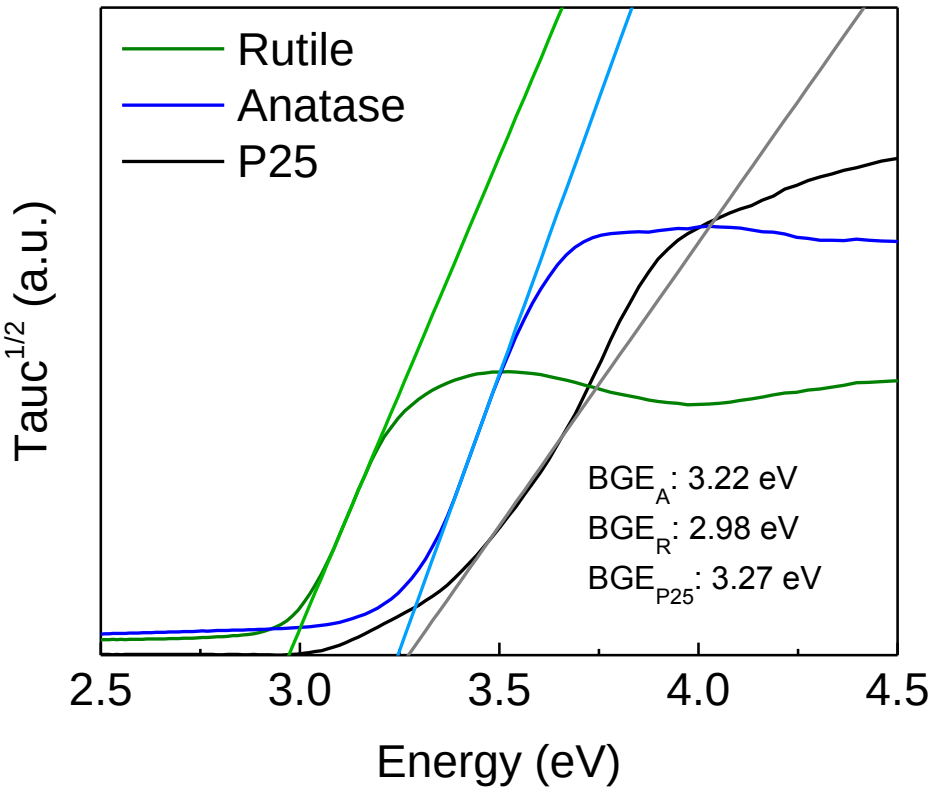

Figure 3.1 Tauc^{½} plot of standard materials; anatase (blue), rutile (green), P25 (black). Lines tangent to inflection point are shown, and apparent BGE values from x-intercepts are given; BGE_A for anatase, BGE_R for rutile, BGE_{P25} for P25.

3.3.2 Anatase and Rutile Mixture Phase Calibration

In order to quantify the composition of mixed-phase TiO_2 samples, a calibration was made using physical mixtures of anatase and rutile. The samples prepared were 100 wt% anatase, 82 wt% anatase, 75 wt% anatase, 67 wt% anatase, 50 wt% anatase, and 25 wt% anatase, with the balance being rutile in all cases. The final sample tested was rutile, sold as >95% purity. XRD powder diffraction patterns were obtained for these physical mixtures and used to verify the anatase and rutile weight fractions for the prepared samples. XRD revealed that the rutile sample contained an anatase-phase impurity of 3.0%. The XRD compositional analysis shows very good quantitative agreement with the nominal compositions, Table 3.2.

Table 3.2 Weight-percent anatase in prepared mixtures of pure anatase and rutile powder as determined by XRD and UV-Vis DPR

Nominal Anatase wt%	XRD wt%[a]	UV-Vis DPR wt%
100[b]	100	100
82	81.9 (5.5)	82.0
75	75.4 (5.1)	74.9
67	67.1 (4.3)	66.5
50	49.9 (4.2)	49.0
25	25.6 (2.3)	28.2
0[c]	3.0 (0.6)	4.7

[a] Values in parentheses are estimated standard deviation between the peak profile and the refined peak profile function.
[b] Pure anatase powder showed no peaks for any other phases in either method
[c] Rutile powder showed peaks for the presence of an anatase impurity by both methods

The composition of these physical mixtures was measured using UV-Visible spectroscopy by plotting the derivatives of the diffuse-reflectance spectra with respect to wavelength and fitting the resulting peaks to Gaussian functions. The results of this DPR analysis are shown in Figure 3.2. All the prepared mixtures where fitted with two Gaussian functions, one each for anatase and rutile. There was no evidence for trace rutile

in the pure anatase powder, so only one Gaussian was used. As with XRD, DPR revealed that the rutile powder contained an anatase impurity, and so two Gaussian functions were used. The peak center position of each Gaussian function corresponds to the BGE of that phase. The measured BGE values via DPR and their respective standard error can be found in Table 3.A1. The BGE of anatase was 3.31±0.01 eV for the pure material and 3.34-3.37±0.01 eV for the physical mixtures. The BGE of rutile was measured as 3.03±0.01 eV in the parent sample, and was 3.04-3.08±0.01 eV in the mixtures. The BGE of the rutile phase increased slightly with increasing anatase content, while there was no significant effect on the BGE of anatase. The change in the rutile BGE is likely due to fermi level band-bending from synergistic effects between the bands in anatase and rutile particles.[64,65] Band bending occurs when there is a junction of two different semiconductors (or a semiconductor and a metal), the difference in band energies along the junction causes the bands to bend and meet. The increase in rutile BGE with increasing anatase content suggests that the conduction band of rutile bends up towards the anatase conduction band while the rutile valence band bends down toward the anatase valence band. The conduction band of rutile is more positive than that of anatase, allowing for a slight band bending in anatase-rutile mixtures.[65,66]

The mass fraction of anatase in each sample was calculated from the peak areas of the Gaussian functions using equation 2. These values are compared to the values obtained from XRD in Table 3.2. The agreement shows that the value of 1.34 obtained for the relative response factor of rutile to anatase is reasonable and gives a good linear fit to the data.

While Raman spectroscopy successfully produced reliable and accurate estimates of composition in P25 and pretreated derivatives thereof, as discussed in section 3.4, Raman analysis of the physical mixtures of commercial anatase and rutile used in Table 3.2 resulted in highly variable weight percent anatase measurements. This was likely due to the use of a Raman microscope with a narrow focal spot (relative to other techniques) – such that the measurements of composition varied if the spot was moved within a given sample. It is possible that agglomerates of rutile particles, being larger in size than those of anatase particles, were not uniformly distributed spatially within the narrow focal spot of the Raman microscope, while the larger sampling area of the XRD and DPR techniques were insensitive to this spatial variation.

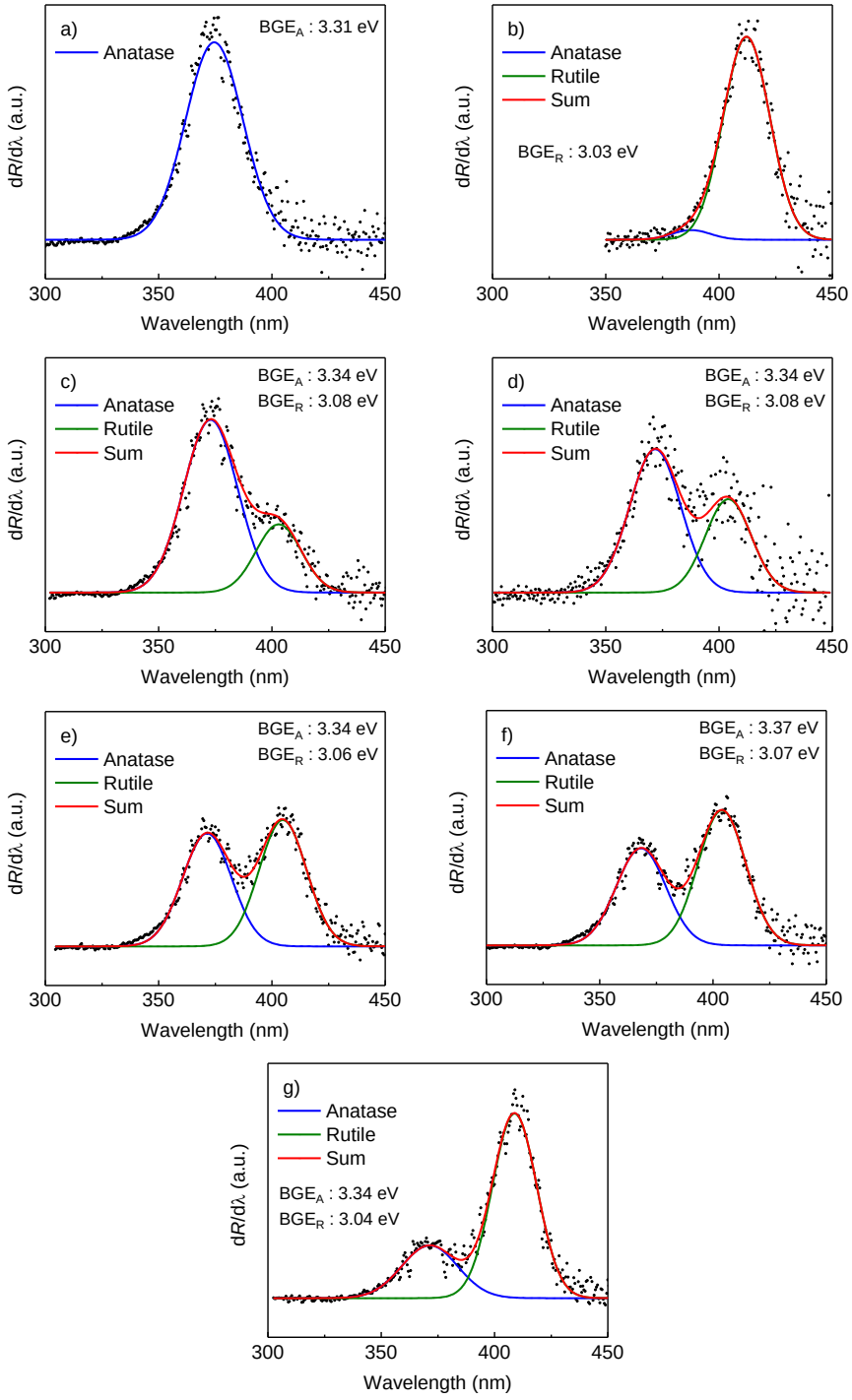

Figure 3.2 DPR analysis of anatase/rutile physical mixtures; a) anatase, b) rutile, c) 82 wt% anatase, d) 75 wt% anatase, e) 67 wt% anatase, f) 50 wt% anatase, g) 25 wt% anatase. Balance is rutile in c)-g). Peak fitting of anatase (blue curve), rutile (green curve), and sum (red curve) shown superimposed over the experimental data (black points). BGE values of each polymorph measured by position of peak maxima are given: BGE_A for anatase, BGE_R for rutile.

3.3.3 DPR Analysis of P25

Having established that DPR is able to quantitatively measure the composition of mixed-phase TiO_2 samples, the technique was applied to the diffuse-reflectance spectrum of P25. The peak fitting is shown in Figure 3.2a). While the Tauc method measured only a single BGE for P25, DPR identified two phases with BGE of 3.33 eV for anatase and 3.12 eV for rutile. The deviation in BGE from the pure-phase materials (3.31 eV for anatase and 3.02 eV for rutile) arises from band bending due to synergistic interaction between the bands of the two phases – this same effect was seen to a lesser extent with the physical mixtures and is more intense with P25.[64] The composition of P25 as calculated by DPR was 86.1 wt% anatase and 13.9 wt% rutile. While P25 is marketed as approximately 80 wt% anatase, XRD determined that anatase comprised 84.6 wt% of the material – once again showing good agreement between the XRD and DPR values. The XRD pattern for P25 is shown in Figure 3.4.

There have been several reports of the presence of amorphous TiO_2 in as-received P25 in variable amounts in some batches while being absent in others.[36-39] If present, amorphous TiO_2 in P25 would not be directly detectable by XRD, and neither UV-Vis nor Raman analysis was able to detect the presence of such a phase in P25 or any sample in the present study. These three techniques are relatively insensitive to amorphous phases, and as such the amorphous composition is neglected in all following analysis.

3.3.4 Effect of Pretreatment Conditions on Rutilization of P25

It has been shown that when anatase TiO_2 is heated at ambient pressure, it will convert to rutile.[67–69] The temperature at which this process begins for pure TiO_2 has been reported as low as 673 K,[67,69] and as high as 873 K.[67,68] Contaminants, raw materials used,

and varying methods of processing can influence this temperature.[70] This phase transformation may also depend on particle size, surface area, particle shape/aspect ratio, gas atmosphere, volume of sample heat treated, nature of heat treatment container, impurities, dopants, measurement techniques, as well as ramp rate and soak time for heat treatment.[70] Due to the influence of these multiple factors, all controllable factors were kept constant (i.e. atmosphere, container, ramp and soak, measurement technique, and P25 lot). Apparent crystallite size from XRD patterns (Table 3.A1) indicated a minimal change in anatase particle size for all treatments of P25. Therefore the changes in particle shape/aspect ratio of the P25 samples were investigated to aid in the explanation of the change in anatase to rutile transformation for ground and sieved samples.

Several prior publications have reported on phase transformation of titanium oxides upon mechanical treatment.[71-76] Ball milling anatase transforms it into denser rutile, where srilankite (TiO_2-II: an orthorhombic, α-PbO_2 type modification, high pressure phase) is an intermediate.[71-72] Additionally, shearing anatase[75] and shearing rutile along the (011) hcp plane[76] can form the metastable srilankite phase. Milling has also been shown to increase photocatalytic activity.[77]

The effect of pretreatment conditions on rutilization of P25 was investigated by subjecting as-received P25 samples to calcination, grinding, sieving, and combinations of these operations. The resulting powders were analyzed by XRD, Raman, and DPR to determine polymorph composition. The results are summarized in Table 3.3. The DPR measurements of phase composition were in good agreement with the XRD values. Typically, the agreement between the XRD and DPR values was within 8 wt% (ten samples), and two samples showed deviations of approximately 11 wt%. The Raman

analysis also showed good quantitative agreement with the XRD measurements, as the particles of anatase and rutile were presumably more uniformly distributed within the microscope focal spot in P25-derived samples. The largest error between Raman and XRD estimates was 15 wt% (two samples). Out of the twelve samples analyzed, XRD, DPR, and Raman close quantitative agreement with for eight of them, while G-C300 was accurate with Raman but not DPR. Three samples (G-C700, S50, G-S50) gave poorer quantitative agreement by both methods.

Table 3.3 Weight percent anatase in ground, sieved, and calcined P25 as determined by XRD, Raman, and UV-Vis DPR.

Sample	XRD[a] wt%	Raman wt%	UV-Vis DPR[b] wt%
P25	84.6 (5.6)	85.2	86.1 (0.4)
C300	84.0 (5.6)	80.0	85.1 (0.9)
C500	82.7 (5.5)	84.7	84.8 (2.0)
C700	11.7 (1.1)	7.2	17.0 (1.3)
G-P25	84.2 (5.7)	88.9	80.4 (1.3)
G-C300	85.9 (0.7)	86.4	74.6 (2.3)
G-C500	84.6 (5.6)	85.8	81.1 (2.7)
G-C700	73.3 (0.6)	58.7	66.1 (0.2)
S50	85.6 (5.7)	71.0	77.7 (1.0)
S50-C500	83.8 (5.6)	82.3	80.6 (1.2)
G-S50	85.7 (5.8)	76.0	74.2 (1.1)
G-S50-C500	71.6 (5.1)	77.4	74.5 (2.2)

[a] Values in parentheses are estimated standard deviation between the peak profile and the refined peak profile function.
[b] Standard deviation for triplicate samples given in parentheses.

3.4.1 Calcination

The calcination temperature of P25 had a strong effect on composition. When calcined at 573 K or 773 K (C300 and C500) the wt% anatase and rutile in the samples were unchanged relative to the parent P25, within experimental error, by all three analytical techniques. By contrast, calcination at 973 K converted a majority of the

anatase in the sample into rutile, such that the anatase measured via XRD dropped from 84.6 wt% in P25 to 11.7% wt% in C700, in good agreement with prior results.[41] The XRD patterns are given in Figure 3.4. In as-received and lower-temperature calcination P25, the (101) peak of anatase at $2\theta = 25.4°$ was the most intense, while the (110) peak of rutile $2\theta = 27.5°$ was small due to its low concentration in the samples. The XRD pattern for C700 reversed this, with the rutile (110) peak becoming the dominant peak and the anatase (101) peak becoming a minor speak. This dramatic change in composition over a range of 200 K, with no change at 773 K and near-total composition change at 973 K, points to the importance of understanding these phase-transitions in mixed-polymorph TiO_2 samples.

In addition to the composition analysis, XRD was used to characterize the apparent crystallite sizes of the anatase and rutile crystallites in the samples using the full-width at half-maximum of the diffraction pattern peaks. The results are shown in Table 3.1. Calcination showed little change in anatase crystallite size, from 20 nm as-received and calcined at 573 K, and increasing to 23 nm and 26 nm when calcined at 773 K and 973 K respectively. Indeed, spherical particles of anatase would be expected to be stable relative to other polymorphs up to diameters of 30 nm,[78] so larger particles may not be expected. The rutile crystallite sizes were more variable. The as-received and 573 K calcination samples were once again indistinguishable at approximately 30 nm, but this increased to 37 nm at 773 K and further to 51 nm at 973 K. Rutile is the more stable phase at larger particle sizes.[78]

The DPR analysis and peak deconvolution of calcined P25 samples is shown in Figure 3.3. As was seen with the physical mixtures, distinguishing between anatase and

rutile phases was possible due to the Gaussian peak-fitting of the two polymorphs present in the same sample. P25, C300, and C500 show nearly indistinguishable DPR patterns. C700 shows a very different pattern, with a greatly reduced peak for anatase and with the rutile peak now dominant.

Using DPR for composition analysis allows for the simultaneous measurement of the BGE of each phase present in the mixed-phase samples from the same experimental data. This analysis revealed that calcination played no role in the BGE values of each phase present. The BGE of rutile remained within a small range of values between 3.12 and 3.13 eV upon calcination up to 773 K, and dipped slightly to 3.09 eV at 973 K. The BGE of anatase remained unchanged (3.32-3.33 eV).

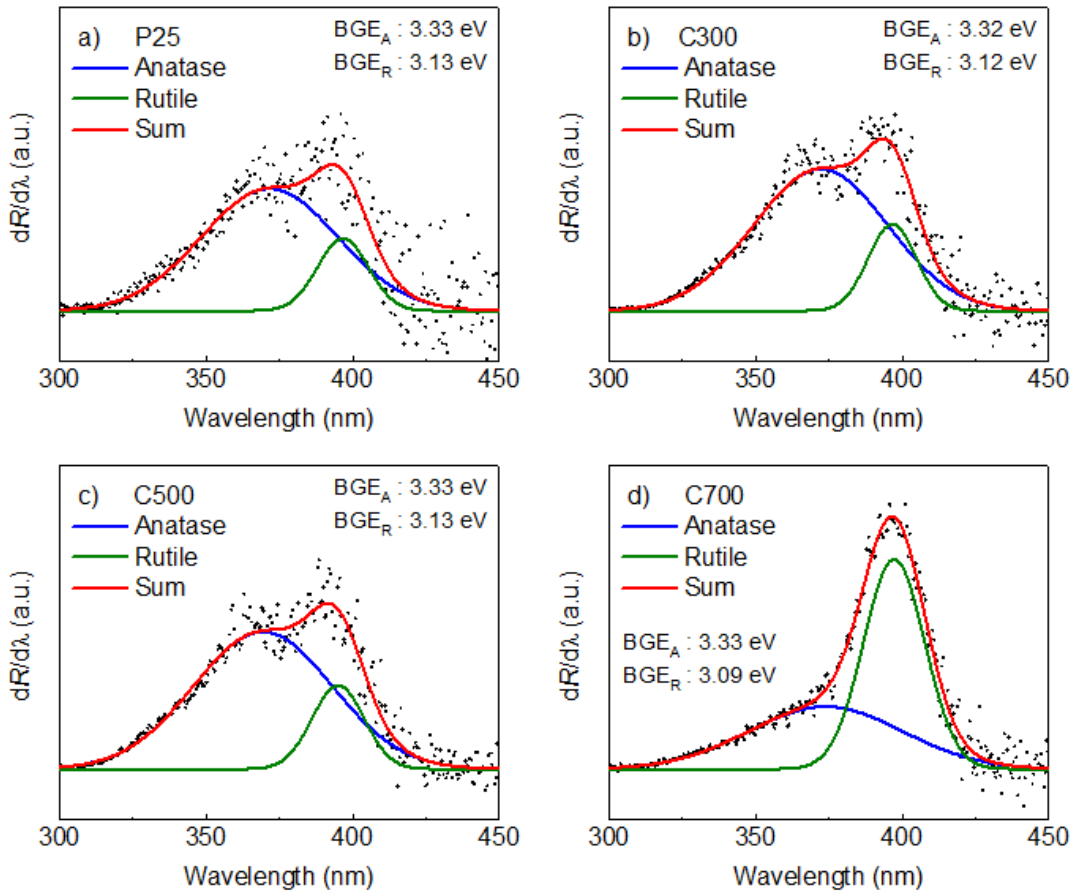

Figure 3.3 DPR analysis of P25 calcined to various temperatures; a) as-received P25, and calcined at b) 573 K (C300), c) 773 K (C500), d) 973 K (C700). Peak fitting of anatase (blue curve), rutile (green curve), and sum (red curve) shown superimposed over the experimental data (black points). BGE values of each polymorph measured by position of peak maxima are given: BGE_A for anatase, BGE_R for rutile.

The Raman spectra (normalized with respect to the total area of each spectrum) of the phonon modes of the TiO_2 lattices present in the as-received and calcined P25 samples are shown in Figure 3.5. As with XRD and DPR, distinguishing between the anatase and rutile phases was facile with Raman. Quantifying the phase composition was achieved using the peak height of the anatase band at 639 cm^{-1} and the rutile band at 610cm^{-1}. Below 973 K, no significant changes in the spectra could be identified. The spectra indicate that upon calcination at 973 K there was significant rutilization and the

dominant polymorph was rutile. The peak height of the Eg band of anatase at 143 cm^{-1} and the full-width at half maximum of the remaining peaks increased following calcination, while there was no shift in the band positions, thus indicating a small increase in crystallite size, in agreement with the apparent crystallite size from XRD.

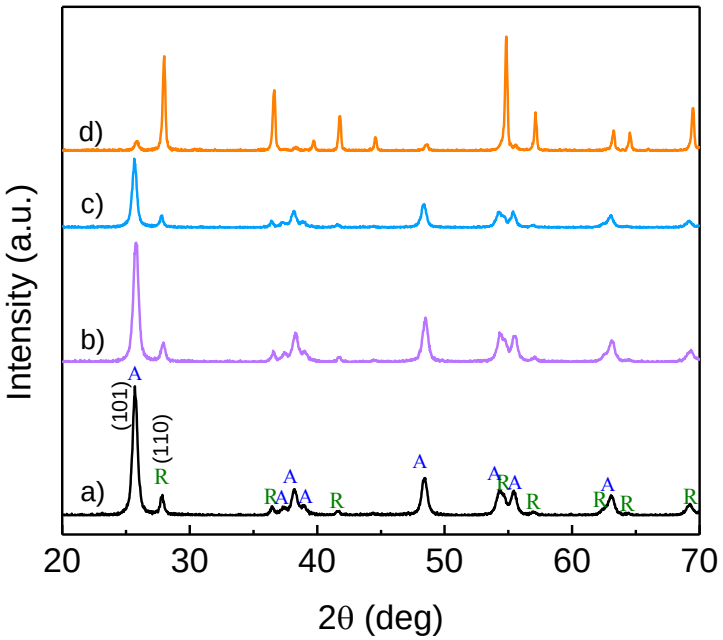

Figure 3.4 XRD patterns of P25 calcined to various temperatures; a) as-received P25, and calcined at b) 573 K (C300), c) 773 K (C500), d) 973 K (C700). Peak assignments for anatase phase (A) and rutile phase (R) are labelled on a).

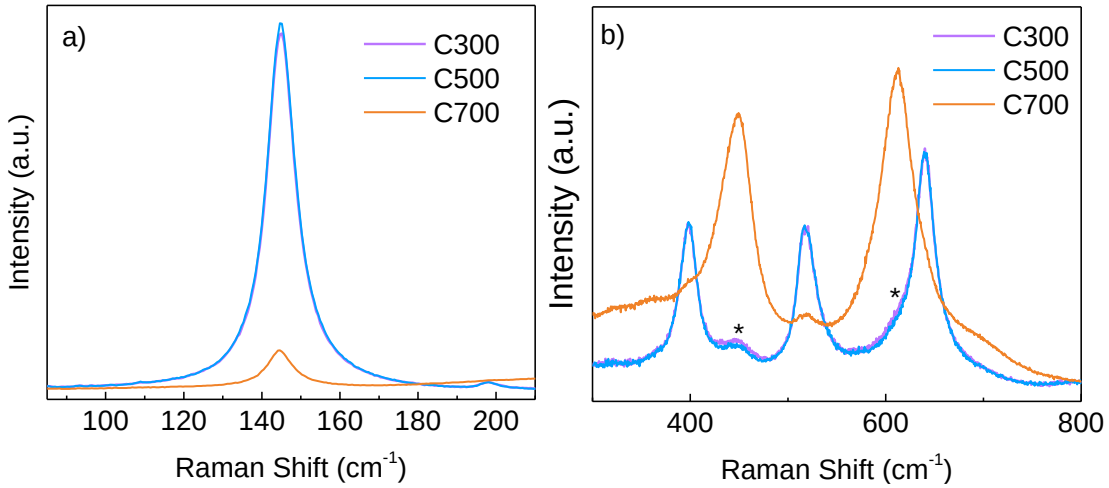

Figure 3.5. Raman spectra of P25 calcined 573 K (C300), 773 K (C500), 973 K (C700). Phonon modes of rutile phase are labelled with an *. All other phonon modes are assigned to anatase.

3.4.2 Grinding and Sieving

Grinding and sieving are common practices when handling powdered metal oxides to achieve uniform agglomerate particle sizes. Typically, they would not be expected to affect the composition of the material. The effects of these pretreatment conditions, together with calcination, are given in **Table 3.3**.

Grinding P25 (G-P25) did not have a significant effect on the phase distribution of the sample as measured by XRD, Raman, and DPR. Sieved P25 particles belonging to agglomerates between 45 μm and 53 μm (S50) similarly showed little change in composition by XRD. A combination of grinding and sieving (G-S50) also produced no appreciable composition change by XRD.

Though shearing of anatase and rutile can produce the high pressure metastable srilankite phase, no characteristic peaks for srilankite were seen in XRD, and no additional BGE was seen in DPR.

3.4.3 Calcination after Grinding and Sieving

While grinding and sieving did not themselves affect the phase composition, these pretreatment techniques influenced the behavior of the samples under calcination (Table 3.3). Calcining as-received P25 at 973 K led to the conversion of most of the anatase to rutile. Grinding P25 prior to calcination (G-P25) led to a stabilization of the anatase phase with respect to temperature. Calcination at 573 K and 773 K led to no change in composition (G-C300, G-C500), as seen with as-received P25, but calcination at 973 K only converted a small fraction of the anatase to rutile (G-C700). The reduction in anatase wt% was only 13% in G-C700 compared to 73% in C700.

Grinding and sieving (G-S50) did not affect the composition, but subsequent calcination to 773 K (G-S50-C500) showed a reduced onset temperature for rutilization. While as-received P25 showed no appreciable difference in composition upon calcination to 773 K (C500), G-S50-C500 showed a reduction in anatase wt% of 11%.

3.4.4 Analysis of the Impact of Processing Conditions by XRD

The amount of pressure and shear from simple grinding with a mortar and pestle were insufficient to induce phase change in the TiO_2. However, it is conceivable that grinding could cause changes in the exposed facets or shape of the crystallites in a powder. This is feasible as the hardness of the mortar and pestle (agate quartz, Mohs hardness = 7)[79] exceeds that of the powder material (Mohs hardness = 6-6.5 for rutile, 5.5-6 for anatase).[79] As anatase is softer than agate and even rutile, the greatest impact on the crystallites from grinding P25 is expected to be on the anatase particles, and the presence of rutile will increase this effect relative to grinding powders of pure anatase. The effects on rutilization onset temperature and extent of rutilization upon grinding and sieving were investigated by analysis of the (hkl) facets in the anatase crystallites measured by XRD.

The XRD patterns of several samples normalized to the maximum intensity of the anatase (101) peak at $2\theta = 25.4°$ shown in Figures 3.6. The intensities of anatase (hkl) peaks relative to the anatase (101) peak are given in Figure 3.7 and 3.8. The relative size of different exposed facets of anatase crystallites determines the particle shape. The Wulff construction for anatase in vacuum suggests that a slightly truncated bipyramid with a majority of (101) exposed facets to be most stable.[80] Other authors have reported changes in (hlk) peak intensities relative to the anatase (101) peak as indicators for both changes

in exposed facets and particle shapes in their samples, including increased (103) intensity indicating hexadecahedra with exposed (103) and (101) facets,[81] increased (211) intensity for anatase thin films with preferential (211) facet growth,[82] and increased (105) intensity in anatase single crystals bounded by (105) facets.[83]

Qualitatively, the XRD patterns (Figure 3.6) showed little variation between samples (except for G-S50-C500, discussed separately below), which also corresponded to the similar polymorph composition of these samples. Quantitative comparison of the (hkl) peak intensities (Figure 3.7) revealed some variation between samples. Sieving by itself did not have much of an effect on the observed XRD patterns, with a small increase in the intensity of the (004) peak relative to as-received P25. Grinding showed a stronger effect on the (004) peak, as well as a small increase in the (200) peak, a larger increase in the (215) peak, and a reduction in the (105) peak. Grinding the clearly had a small but detectable effect on the shapes of the anatase crystallites. Sieving the ground sample separated out agglomerates of different sizes, and the anatase particles contained within agglomerates between 45 μm and 53 μm in diameter contained a slightly different distribution of particle shapes than the entire ground sample. The increase in the (200) peak was more prominent, and an increase in the intensity of the (211) peak was also observed. The crystallites in the ground and sieved particles where therefore distinct in their XRD patterns and particle shapes compared to as-received P25.

Comparing the (hlk) intensities of C500 to P25 and the ground and sieved samples, the patterns are nearly identical, with only a small increase in the (200) peak. This shows that grinding and sieving has a more significant impact on exposed facets and

crystallite shapes than calcination to a temperature below the anatase-rutile transition in P25.

Comparing the XRD pattern for G-S50-C500 to the other patterns in Figure 3.6 shows a qualitative difference as several peaks are immediately noticeable as having increased intensities relative to the (101) peak. Quantitative comparison in Figure 3.8 reveals that nearly all peak intensities are enhanced relative to the (101) peak as compared to as-received P25 and C500. Despite the identical calcination temperature for C500 and G-S50-C500, small changes in particle shape induced by grinding and sieving lead to very different particle shapes upon calcination. Some of the particles in ground and sieved samples were susceptible to rutilization at a lower temperature, but the G-C700 data and Section 3.5 suggests that the particle shapes achieved by the remaining particles at 773 K were more resistant to rutilization. It also indicates that all particles in the mixture undergo some physical change, but that the pre-calcination shape determines the outcome. One population of particles transforms into rutile, while another population changes into a shape that is resistant to rutilization. The as-received particles underwent neither transformation at 773 K, but at 973 K, the majority of anatase particles transformed to rutile. The remaining anatase particles had significantly different shapes from the as-received P25, as well as from G-S50-C500 (Figure 3.8), but once again the relative intensity of the (101) peak was significantly reduced, as indicated by the growth of the other peaks. In both cases, these resulting particles were resistant to further rutilization (Section 3.5), but the temperatures at which these particles were obtained were 200 K apart

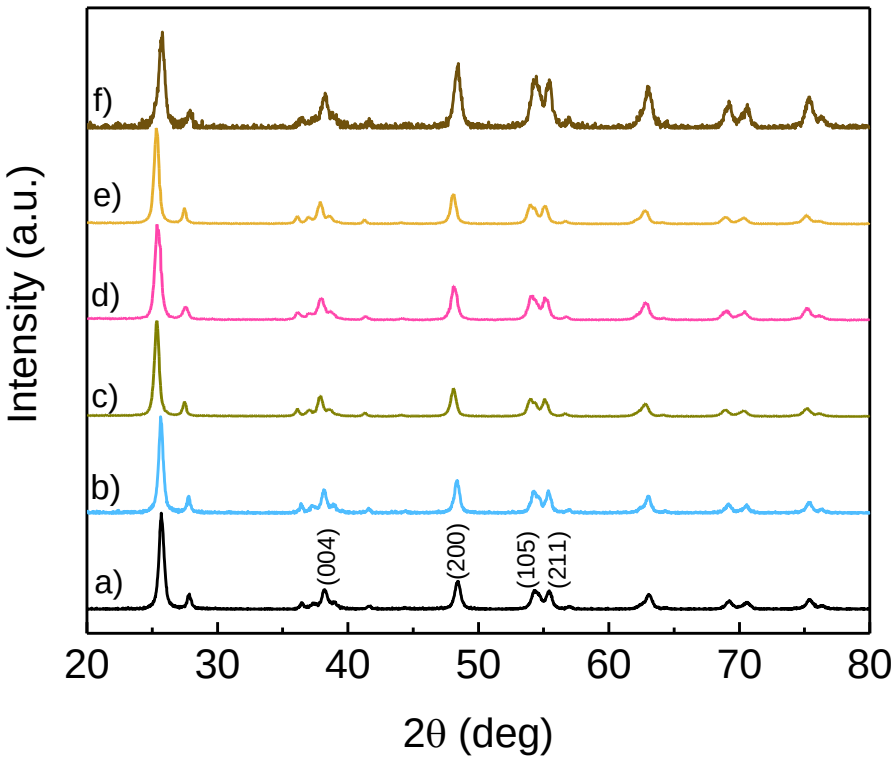

Figure 3.6 Normalized XRD patterns of P25 subjected to different pretreatments conditions; a) P25, b) C500, c) S50, d) G-P25, e) G-S50, f) G-S50-C500. Samples identified in Table 3.1.

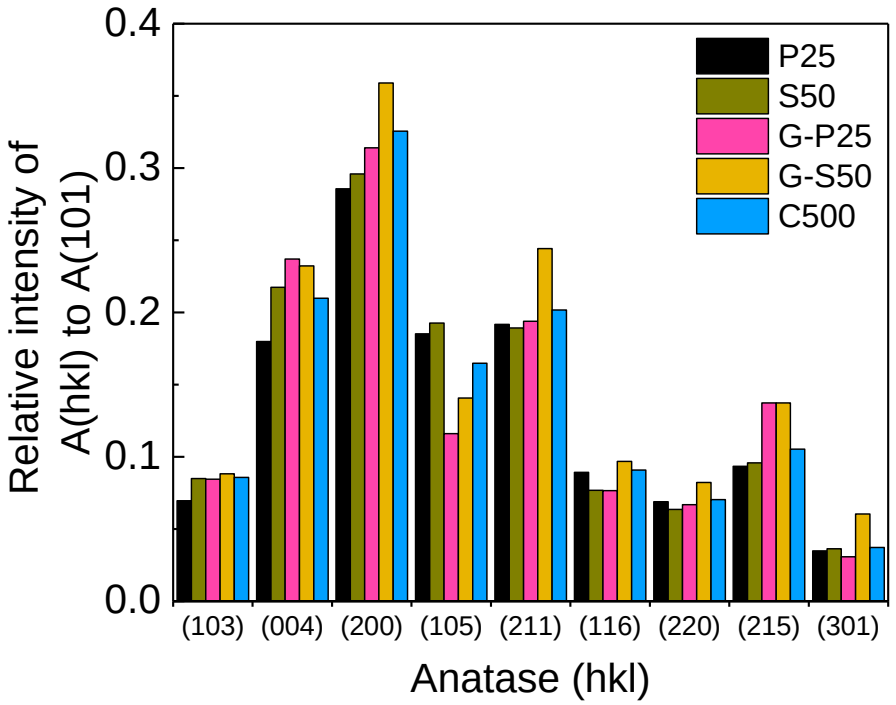

Figure 3.7 Relative intensities of each (hkl) anatase peak to the anatase (101) peak for sieved and ground samples compared to C500. Samples identified in Table 3.1.

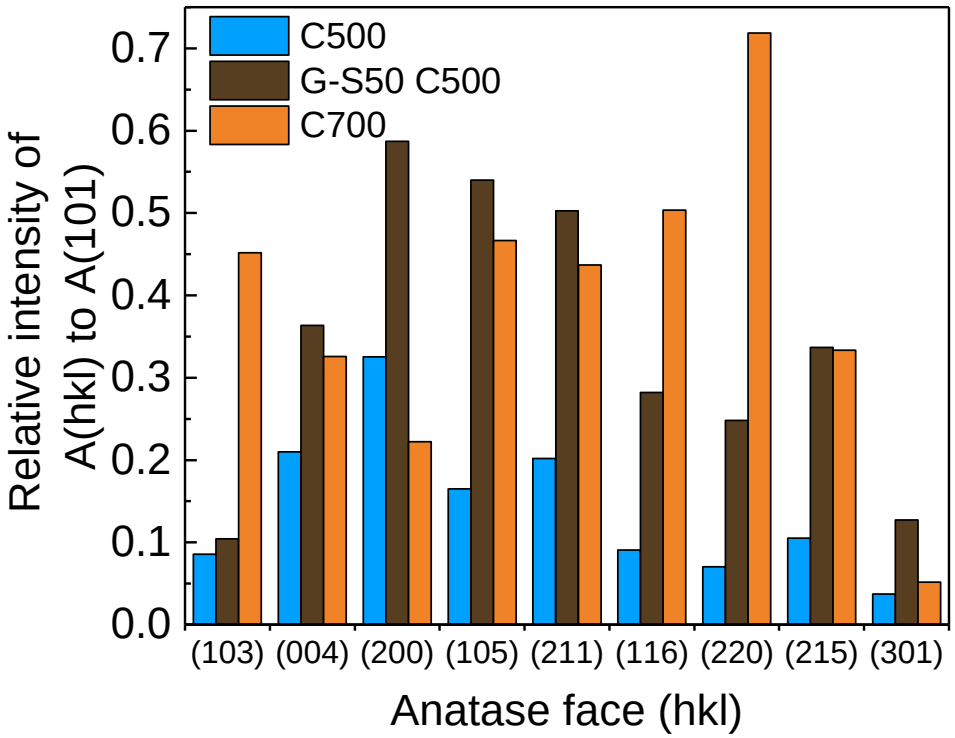

Figure 3.8 Relative intensities of each (hkl) anatase peak to the anatase (101) peak for calcined samples. Samples identified in Table 3.1.

The anatase structure is controlled by a balance between the anion-anion (O-O) repulsions and the cation-anion (Ti-O) attractions.[84,85] Therefore the increased ratio of anions to cations on the surface of the (200) facet may lead to increased stability of the G-S50 sample with an anatase phase that has an increased amount of (200) faces. Additionally, it has been shown using first-principles calculations that the (200) surface is the second most stable face of anatase.[86] While the anatase (101) has a surface energy of 0.44 J/m^2 the anatase (200) surface is close in energy, 0.53 J/m^2.[86] This suggests that the increased intensity in the (200) peak in the XRD pattern for G-S50 is at least partly responsible for the stabilization effect.

As grinding alone (without sieving) had an effect on particle shapes, an effect on stabilization would be expected as well. This was observed in comparing C700 and G-

C700, where the ground sample remained majority anatase phase (73 wt%) while the unground sample was mostly converted to rutile.

Despite these changes in particle shape and resistance in rutilization, no pretreatment method had any significant effect on the BGE of either TiO_2 polymorph present (Table 3.A1). While anatase and rutile in as-received P25 had BGE values of 3.33 eV and 3.13 eV, the most of the treated samples had anatase BGE between 3.28 eV and 3.33 eV and rutile BGE between 3.09 eV and 3.13 eV. Only one sample (G-S50-C500) had an anatase BGE outside this narrow range, and then at 3.25 eV was still within 0.1 eV of the parent sample. This supports that the phase and crystallinity of the particles was essentially unchanged.

3.4.5 In Situ Monitoring of Rutilization during Calcination

While both XRD and UV-visible spectroscopy were able to give good quantitative measurements of the composition in mixtures of anatase and rutile, ex situ XRD is limited to analyzing samples exposed to a single set of conditions at a time. In situ XRD would provide more insight into rutilization by allowing for direct observation of phase change with temperature, but requires specialized equipment and significant resource commitment to lengthy XRD data collection. By comparison, in situ UV-visible spectroscopy is a low-cost and accessible technique that can potentially provide similar information.

In order to further investigate the onset temperature for and extent of rutilization, the DPR method was applied to an in situ UV-visible spectroscopic experiment where sample powders were calcined at elevated temperatures while continuously measuring their phase composition. Figure 3.9 shows the composition of P25 and G-S50 samples

that were exposed to calcination conditions at a ramp rate of 2 K min^{-1}. Data below 573 K are not shown, and did not vary significantly from the pre-calcination measurements.

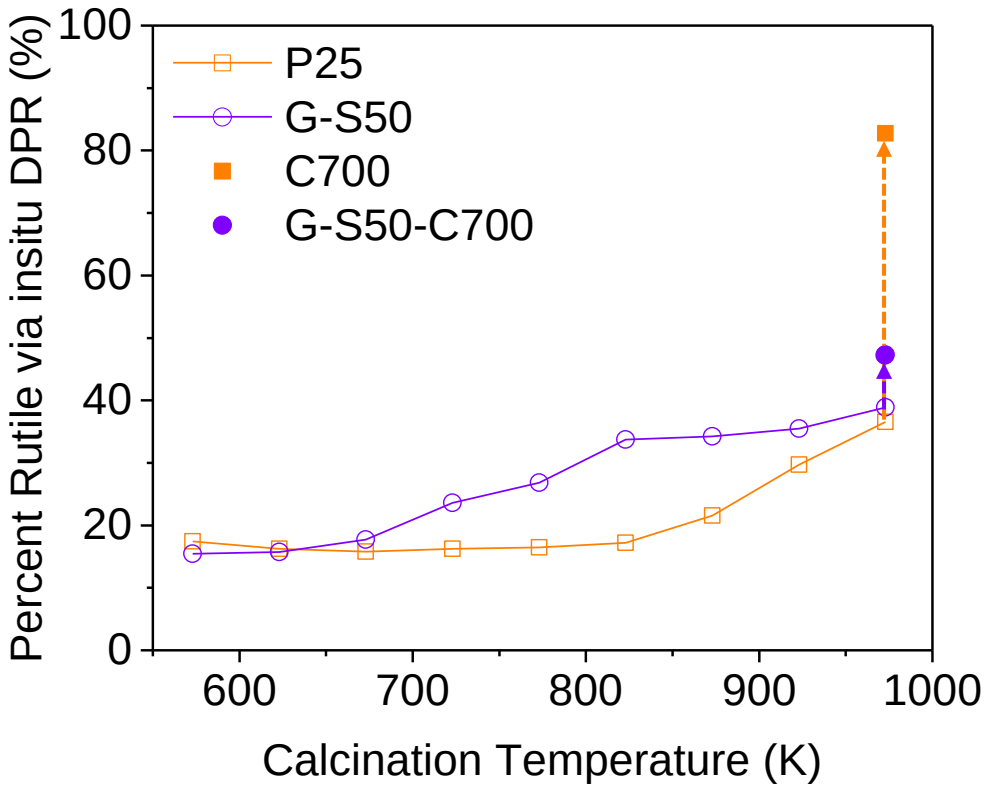

Figure 3.9 Weight-percent rutile in P25 and G-S50 determined via in situ diffuse-reflectance UV-visible spectroscopy during calcination from 573 K to 973 K with a ramp rate of 2 K min^{-1}. The wt% rutile values after three hours of calcination at 973 K (C700 and G-S50-C700) are also shown.

For the treated P25 sample, the composition remained unchanged up to 823 K (in agreement with the ex situ measurements on C300 and C500), followed by an increase in rutile content up to 37 wt% at 973 K. At this point the temperature was held constant for three hours, (as for C700), and the percent rutile reached 83 wt%, which was the comparable to the value obtained for C700. Through in situ DPR analysis, the onset temperature for rutilization could be more accurately identified as being just above 823 K. As expected, G-S50 experienced an earlier onset of rutilization; the composition was

unchanged up to 673 K. The percent rutile measurement at 773 K was consistent with the ex situ measurement at 27 wt% rutile. After this, the rutile content grew linearly with time and temperature up to 823 K (34 wt%). Above 823 K, the rutile content was nearly constant, growing slightly to 39 wt% by 973 K. At this point in the experiment, the wt% rutile in both the treated P25 and treated G-S50 were nearly the same, but the behavior following further calcination for three hours was drastically different. The G-S50 sample only reached a maximum rutile wt% of 47%, compared to 83% for P25. The effect of grinding on particle shape prior to calcination discussed in section 3.4.2 can be interpreted here as imparting a higher rutilization resistance on the particles that were both ground and sieved.

In situ DPR presented a facile means of measuring the phase composition during rutilization, and provided direct evidence in a single experiment of the lower onset temperature of rutilization and the lower overall extent of rutilization of ground and sieved samples. To obtain the same results by XRD alone would require a much larger set of calcination experiments, with samples collected from each experiment giving a single XRD data point.

3.5 Conclusions

Derivative peak fitting of differential diffuse reflectance spectra obtained from UV-visible spectroscopy was performed in conjunction with Raman Spectroscopy and X-ray Diffraction to determine the effect of grinding, sieving, and calcination on the phase transition of anatase to rutile in P25 titanium dioxide.

DPR UV-visible spectroscopy was able to quantify phase composition in as-received P25 as well as post-treatment samples, with good agreement with XRD and

Raman measurements. Additionally, DPR gave direct measurement of the individual band gap energies of each polymorph within the mixture. These measurements established that pretreatment conditions did not change the optical band gaps of the anatase and rutile polymorphs in the samples.

Through in situ DPR measurements during calcination, the onset temperature for rutilization of the anatase phase could be identified as just above 823 K, eventually leading to nearly complete conversion of the anatase to rutile after three hours of treatment at 973 K – a reduction from 86 wt% anatase to 17 wt% anatase by DPR (85 wt% down to 12 wt% by XRD). Grinding P25 prior to calcination reduced the total extent of rutilization, as measured by both XRD and DPR. Sieving of ground particles led to selection of a population of anatase particles that showed a lower onset temperature for rutilization, down to 673 K. Changes in particle shape, as suggested by changed in the XRD patterns of the ground particles prior to calcination, seem to impart both the greater overall resistance to rutilization as well as reduce the onset temperature.

The analysis in this paper aims to support DPR as both a method for measuring polymorph band gap energy and concentration in a multiphase semiconductor. The analysis is facile and could be easily used as a supplementary technique combined with a more established methods of analysis, such as XRD or Raman. Additionally, in situ DPR allows for on-stream analysis of polymorph composition. DPR has also been shown in this work to be a more accurate method for determining BGE for multi-phase samples, such as P25, compared to the traditional Tauc method. The approach described here for compositional and BGE analysis for mixed-phase semiconductors may find application in other systems beyond the anatase/rutile mixtures presented here.

3.A Appendices

3.A.1 XRD patterns of anatase/rutile physical mixtures

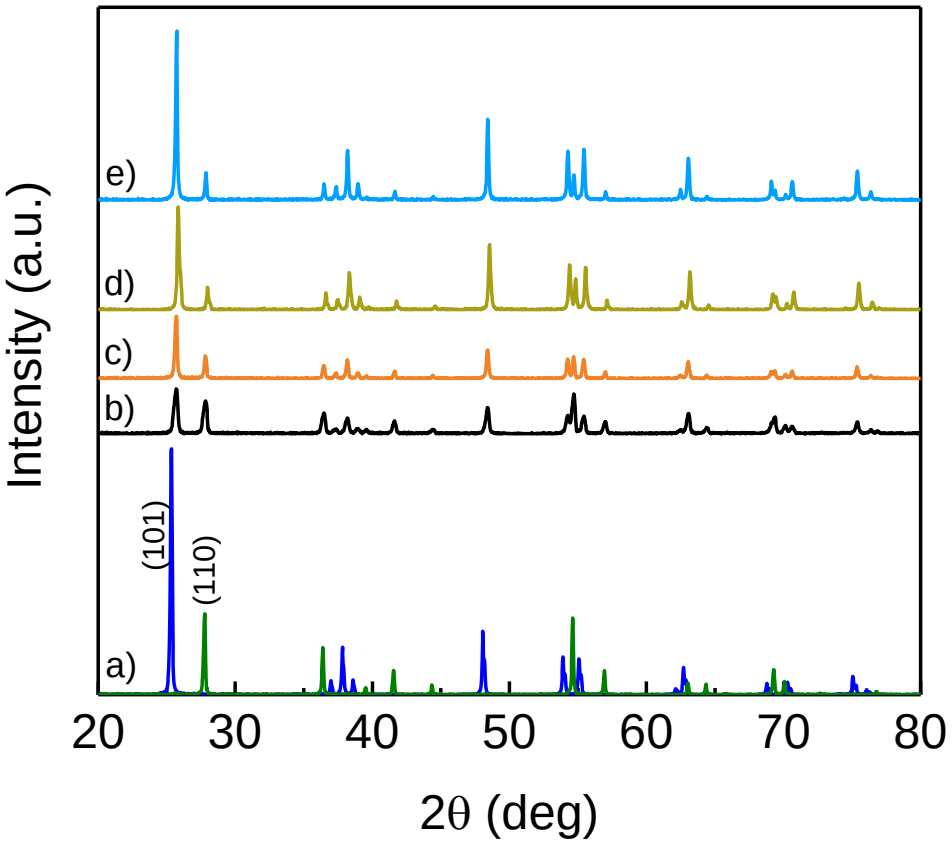

Figure 3.A1 XRD patterns of anatase/rutile physical mixtures. a) pure anatase and pure rutile, b) 50 wt% anatase, c) 66 wt% anatase, d) 75 wt% anatase, e) 82 wt% anatase. Balance is rutile in b)-e).

3.A.2 Crystallite size, BGE, and bulk density of analyzed samples

Grinding and sieving did have an effect on the crystallite sizes of the crystallite particles present in each sample (Table 3.A1). Anatase showed little effect from pretreatment conditions, but rutile was more variable. Rutile showed a large increase in particle size upon calcination of P25 at 973 K (C700), from 31 nm to 51 nm. Grinding (G-P25) showed a significant reduction in rutile particle size from 31 nm to 20 nm.

Table 3.A1 Crystallite size (XRD), BGE (DPR), and bulk density of analyzed samples.

Sample	Crystallite Size by XRD[b] (nm)		BGE by DPR (eV)		Bulk Density[a] (g cm^{-3})
	Anatase	**Rutile**	**Anatase**	**Rutile**	
Anatase	58 ±17	-	3.31 ±0.01	-	0.88
Rutile	-	>100	3.21 ±0.01	3.03 ±0.00	1.35
Anatase (82%)	-	-	3.34 ±0.01	3.08±0.00	-
Anatase (75%)	-	-	3.34 ±0.00	3.08±0.00	-
Anatase (66%)	-	-	3.34 ±0.00	3.06±0.01	-
Anatase (50%)	-	-	3.37 ±0.01	3.07±0.01	-
Anatase (25%)	-	-	3.34±0.01	3.04±0.01	-
P25	20 ±1	31 ±3	3.33 ±0.01	3.13 ±0.00	0.13
C300	20 ±1	28 ±2	3.32 ±0.00	3.12 ±0.00	0.18
C500	23 ±2	37 ±3	3.33 ±0.00	3.13 ±0.00	0.18
C700	26 ±3	51 ±2	3.33 ±0.00	3.09 ±0.00	0.33
G-P25	23 ±2	20 ±4	3.29 ±0.03	3.10 ±0.02	0.68
G-C300	-	-	3.30 ±0.01	3.10 ±0.00	0.24
G-C500	26 ±6	25 ±5	3.33 ±0.01	3.12 ±0.00	0.23
G-C700	-	-	3.33 ±0.01	3.11 ±0.00	0.33
S50	24 ±2-	33±11	3.32 ±0.01	3.11 ±0.00	0.16
S50-C500	22 ±2	27 ±10	3.32 ±0.01	3.12 ±0.00	0.19
G-S50	23 ±1	32 ±6	3.28 ±0.02	3.11 ±0.00	0.43
G-S50-C500	18 ±1	27 ±3	3.25 ±0.01	3.12 ±0.00	0.42

[a] bulk density calculated from the mass of sample required to loosely pack a 0.022 mL sample cup.
[b] Apparent crystallite size from whole pattern fitting Rietveld refinement

3.A.3 Derivative Peak Fitting of the Kubelka-Munk Function

For transmission UV-Visible spectroscopy – such as with liquid samples– light absorbance follows Beer's law, $A = \varepsilon\, l\, c$, where the absorbance, A, is the product of the extinction coefficient, ε, path length, l, and concentration of the absorber, c. For a given species and experimental setup, both path length and the extinction coefficient are constant such that absorbance is proportional to concentration. Differential analysis of absorbance spectra has been used to successfully determine the concentration of different species in solution by measuring the area of the fitted peaks.

In diffuse-reflectance spectroscopy, the Kubelka-Munk function, $F(R_\infty)$, is analogous to absorbance, and as such the Kubelka-Munk function may be expected to be proportional to concentration. It is however much more difficult to ensure a constant path length in diffuse-reflectance spectroscopy due to the different light-penetration depths that might exist in different samples.

$$F(R_\infty) = \frac{(1 - R_\infty)^2}{2R_\infty}$$

Despite these limitations, we evaluated derivative peak-fitting using the Kubelka-Munk function. To measure the concentrations of the polymorphs in physical mixtures of anatase and rutile, the first derivative of $F(R_\infty)$ was calculated. Take the first derivative and deconvolute the $F(R_\infty)$ spectrum into multiple peaks, with each corresponding to a single polymorph.

$$\frac{dF(R_\infty)}{d\lambda} = \frac{F(R_\infty)_i - F(R_\infty)_{i+1}}{\lambda_i - \lambda_{i+1}}$$

Correlating the peak areas obtained in this manner to the known concentration in the prepared anatase/rutile mixtures presented a challenge. The assumption that the peak area fraction in the two polymorphs corresponded to the mass fraction linearly did not apply. The parity plot between the calculated wt% anatase using this assumption (Figure S2) deviated significantly from the parity line, indicating that the relationship between the peak areas in the derivative of the Kubelka-Munk function and the concentration of the TiO_2 polymorphs was either non-linear, or the extinction coefficients were not equal for anatase and rutile, or the path lengths were not equal for anatase and rutile, or some combination of these factors. Additionally, since the relationship between $F(R_\infty)$ and R_∞ is

known the relationship can be expanded and the derivative compared to that of the reflectance

$$\frac{d(F(R_\infty))}{d(\lambda)} = \frac{\left({R_\infty}^2 - 1\right)}{2{R_\infty}^2}\frac{d(R_\infty)}{d(\lambda)}$$

Where the derivative of the $F(R_\infty)$ is not linear with respect to the derivative of the absolute reflectance $\frac{dR_\infty}{d\lambda}$. It would therefore be expected that if the integral of the derivative of absolute reflectance of mixed samples was linear with respect to concentration that the integral of the derivative of the Kubelka-Munk function of mixed samples would not be linear with respect to concentration, which is seen in Figure 3.A2. Peak-fitting the derivative of the Kubelka-Munk Function (DPA), gives a non-linear response with concentration. For this reason, we suggest that derivatives of the Kubelka-Munk function are not suitable for compositional analysis, unlike the DPR analysis used in the remainder of the present work.

Figure 3.A2 shows the raw peak area fractions and assumes that the absolute response factors of the two TiO_2 polymorphs are equal. Using the DPR data, the response factor of rutile relative to anatase was 1.34. This value is intuitively close to 1 for two similar materials. By contrast, the DPA method calculates a response factor of 0.14 for rutile relative to anatase, which is an unexpectedly large difference between polymorphs, and further suggests that DPA is not suitable for composition analysis.

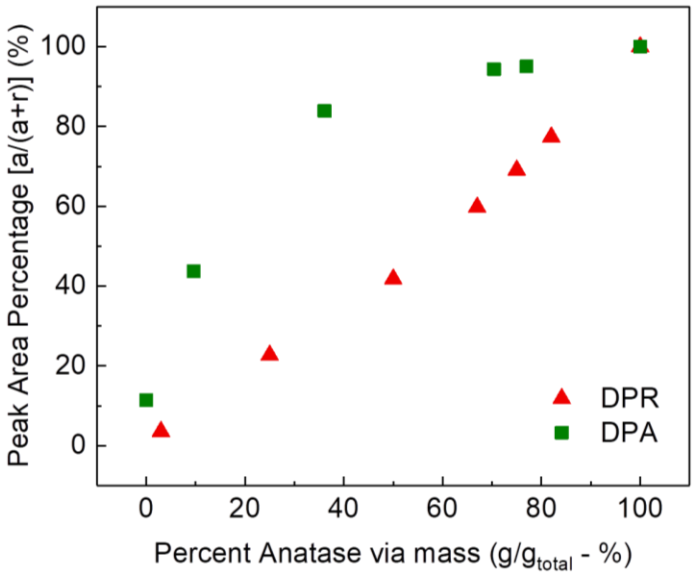

Figure 3.A2 Raw peak area % response for composition (wt% anatase) in physical mixtures of anatase/rutile determined via derivative peak fitting of the Kubelka-Munk function (DPA - green squares) and the absolute diffuse reflectance (DPR - red triangles).

3.A.4 Raman Analysis of pure anatase and pure rutile

Raman Analysis of pure anatase and pure rutile (Figure 3.A3) was used with pure samples and physical mixture to generate a calibration curve that allowed the use of Raman to determine sample composition.

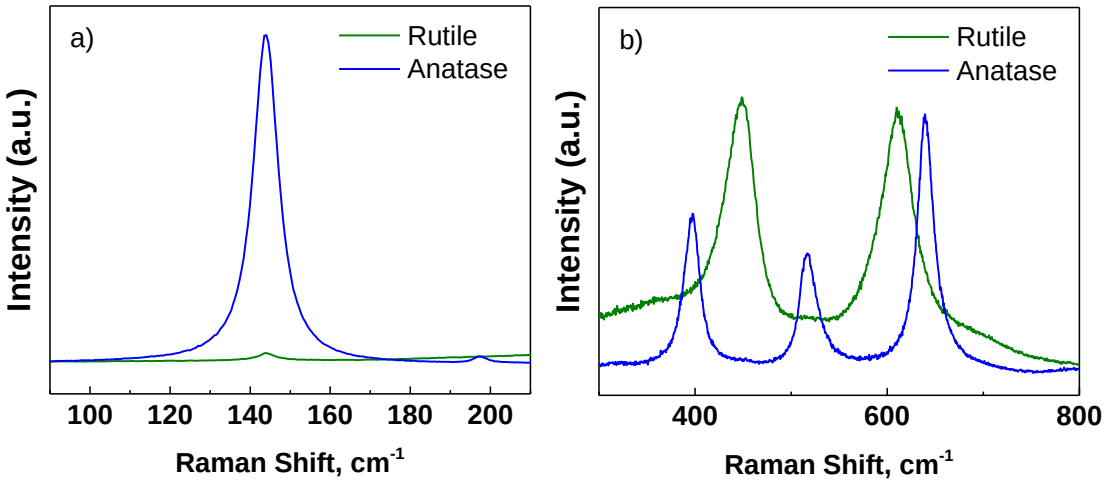

Figure 3.A3 Raman analysis of pure anatase and rutile received from Acros Organics. Peak at 141 cm-1 is consistent with anatase phase.

3.A.5 Derivative Peak Fitting of a) G-P25, b) G-C300, c) G-C500, d) G-C700

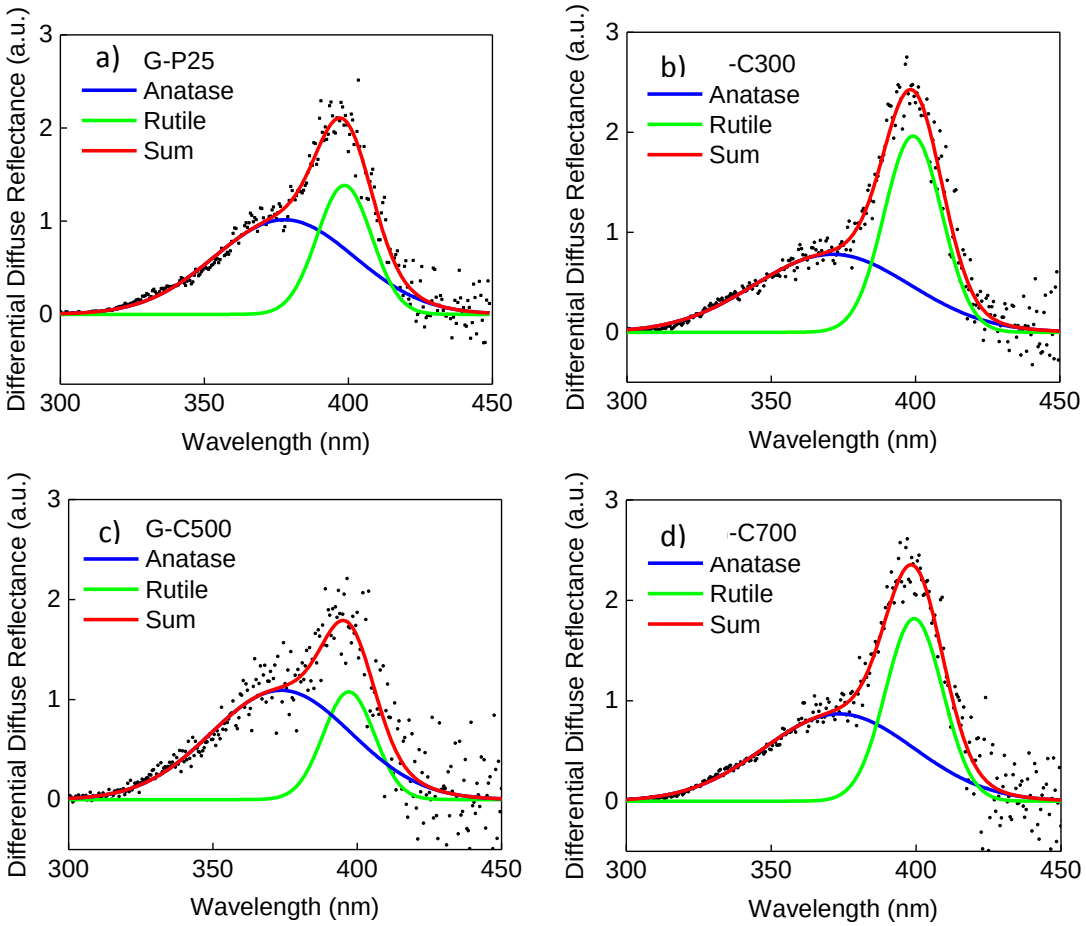

Figure 3.A4 Derivative Peak Fitting of a) G-P25, b) G-C300, c) G-C500, d) G-C700.

3.A.6 Raw diffuse reflectance spectra

The raw diffuse reflectance spectra (absolute reflectance) of samples discussed in the manuscript are included in Figure 3.A5.

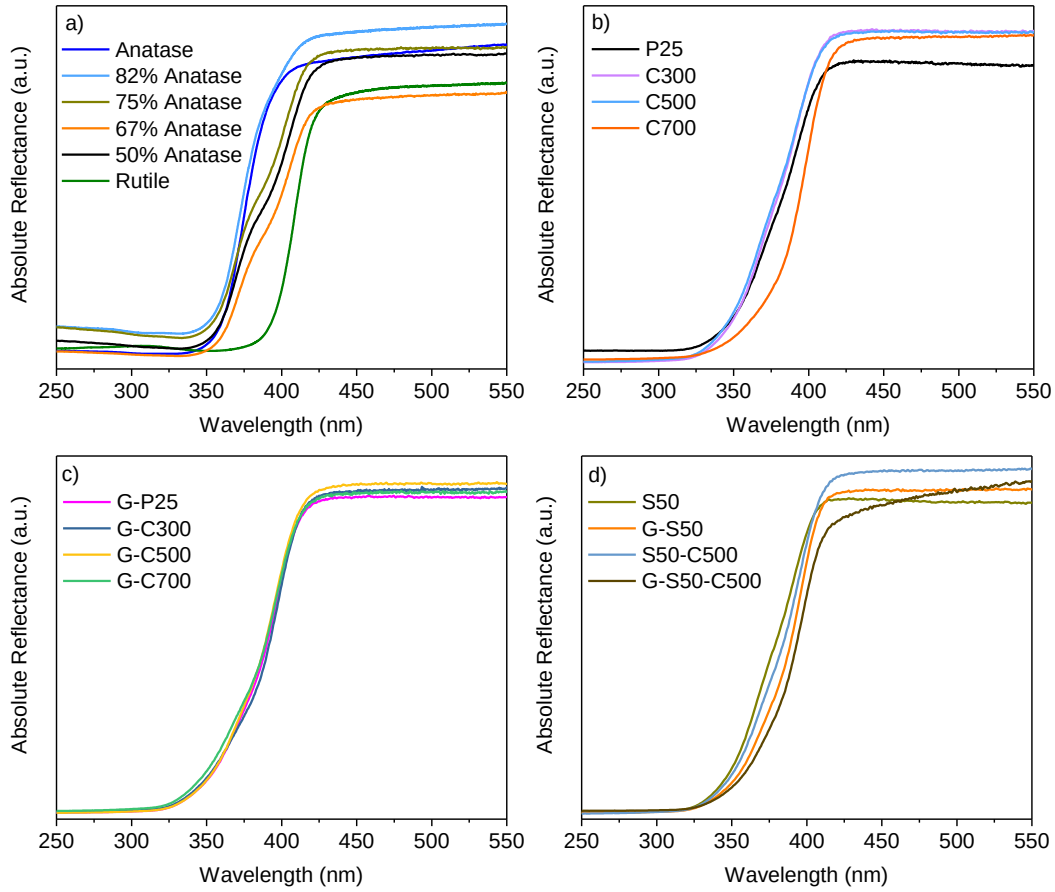

Figure 3.A5 Raw absolute reflectance of a) anatase and rutile physical mixtures, b) P25, calcined P25, c) ground, and calcined P25, d) sieved, ground, and calcined P25.

3.A.7 Spectra collected during in situ calcination

The spectra collected during in situ calcination of C300 are given in **Figure 3.A6**. **Figure 3.A6a**) shows all the raw diffuse reflectance spectra (absolute reflectance) **Figures 3.A6b)-d)** show the deconvoluted DPR spectra for data collected at 573 K, 773 K, and 973 K. The increase in spectral noise at 973 K is due to a roughening of the powder sample surface. The powder sample loaded at room temperature has a flat surface. Above the anatase-rutile transition temperature, the lower density anatase particles are replaced with higher density rutile particles, leading to a higher bulk density of the powder bed and volume reduction. As the volume shrinks, the surface of the powder bed becomes less

smooth and reduces the reflectance of the sample. Despite the added noise, the samples are still reliably analyzed by DPR for quantitative measurement of the anatase and rutile phases present.

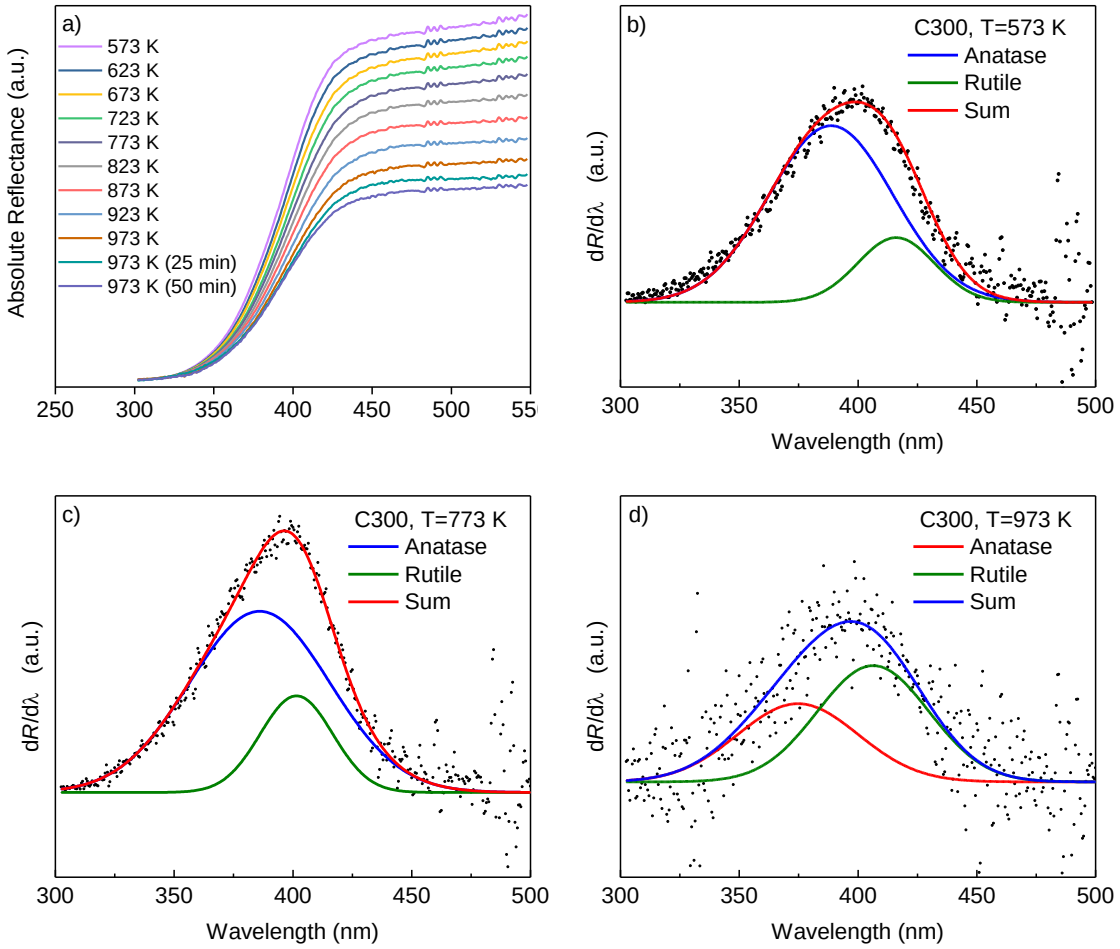

Figure 3.A6 UV-Visible diffuse-reflectance spectra collected during in-situ calcination (a) and derivative peak fitting of samples at 573 K (b) 773 K (c), and 973 K (d).

Chapter 4: Metal-Free Hydrogen Evolution over Defect-Rich Anatase Phase Titanium Dioxide

4.1 Introduction

As mentioned in section 3.1, Titanium dioxide (TiO_2) has been a favored material for applications in catalysis and photocatalysis due to its stability, redox properties, and low cost.[87,88] Photocatalysis for hydrogen generation has generated significant scientific interest since the 1972 example of water splitting over TiO_2 under ultraviolet light illumination.[89] TiO_2 has two very desirable properties for a photocatalyst. First, it is photoactive in near-visible ultraviolet light while maintaining stability under catalytic conditions. Second, its band energies are well-aligned with reactions such as water splitting, namely the conduction band energy is higher than the reduction potential of the proton. Perhaps due to the potentially limitless material feedstock (water) and energy input (sunlight), solar water splitting for hydrogen production has received much attention, but there are other hydrogen-containing feed stocks from which liberating hydrogen gas is thermodynamically easier, including methanol[90–101] and biomass.[102–107]

Hydrogen gas is touted as a clean-burning energy carrier that has potential applications in both stationary and mobile power generation and energy storage at higher efficiency than conventional internal combustion engines.[108–110] However, the majority of hydrogen produced commercially is derived from an unsustainable process: Methane steam reforming (MSR) of fossil-fuel derived methane.[111-113] MSR is used to convert fossil methane to hydrogen gas and carbon monoxide as syngas at high temperature. Not only does this process use an unsustainable feedstock, but it also suffers from being an endergonic and endothermic reaction that operates at poor atom efficiency based on C and

H. This poor efficiency is due in part to the need to burn half of the methane feed to provide heat for the process, which releases CO_2, a greenhouse gas, into the atmosphere.[114]

Photocatalytic methane steam reforming by contrast offers several advantages for hydrogen generation. For reaction to proceed spontaneously, the following inequality must hold, $\boldsymbol{\Delta G < W_e}$, where W_e is the external input of non-PV work. For a thermochemical reaction, there is no external work function ($W_e = 0$), so the reaction proceeds only when $\boldsymbol{\Delta G < 0}$. In a photochemical reaction, photoexcitation provides external energy input in the form $W_e = hv$, where h is the Planck constant and v is the frequency of irradiated light. Therefore, for photocatalysis, the thermodynamic limitation is $\boldsymbol{\Delta G < hv}$. Since $\Delta G°$ =113 kJ mol^{-1} for MSR, this requires a semiconductor with a band gap energy of 1.17 eV or larger to absorb photons of enough energy. This minimum theoretical band gap energy is readily met by many wide-band gap semiconductors including TiO_2. As mentioned in section 1.4, the band gap energy of the anatase polymorph of TiO_2 is 3.2 eV. In this way, photocatalytic MSR bypasses the thermodynamic equilibrium limitations of thermocatalytic MSR. The addition of photon energy, *hv,* means the system is not at thermal equilibrium, therefore the equilibrium limitation is not the same as in the absence of light at the same temperature.

Once the high temperature requirement is relaxed, the process may proceed at lower temperature, and many deficiencies of industrial MSR could be addressed. At lower temperature, residual or waste heat could be used to drive the reaction, eliminating the need for external fuel burn and immediately doubling the atom efficiency and increasing the hydrogen yield of the process. Operating at these conditions would also limit the amount of coke formation, leading to longer process cycles and less reactor down time. The

elimination of the furnace when conducting MSR at low temperatures with waste heat would simplify the reactor design and materials of construction, making the process more scalable and applicable to smaller scale and point source operations. The smaller scale of operation will allow biorenewable methane to become a feasible feed stock for MSR. Biorenewable methane can be obtained from landfill gas, and the anaerobic digestion of waste streams, such as food waste and wastewater. Waste-derived biomethane can be considered a renewable and net CO_2-free hydrogen source, as the carbon in the methane was removed from the atmosphere during photosynthesis, and returns to the atmosphere after the MSR process. If the energy for the MSR reaction comes from solar photons, the hydrogen synthesized this way is renewable.[115,116] An additional benefit of biomethane utilization at point sources such as landfills and dairy farms is to incentivize capture of methane emissions, instead of releasing the potent greenhouse gas into the atmosphere. Methane has more than twenty times the global warming potential per carbon as CO_2 over 100 years.[117] Solar thermal heating for MSR[111,118] would couple well with photocatalytic reaction conditions, providing both adequate heat for the endothermic reaction at the desired elevated temperature as well as high photon flux in a solar concentrator.

Photocatalytic methane steam reforming for hydrogen production has been investigated experimentally by the group of Yoshida.[119–126] They found that supporting Pt on a variety of semiconductors is effective for hydrogen evolution from steam and methane with quantum yield up to 30%. In the reaction of water and methane over Pt/TiO_2, CO_2 was the primary carbonaceous product, with trace quantities of CO and ethane formed during an induction period. In these experiments platinum was always included as a

cocatalyst as TiO_2 is not able to evolve H_2 gas without precious metal cocatalysts due to a lack of the required active site.[127]

It is known that under certain pretreatment conditions, including exposure in vacuum and thermal treatment under reducing atmosphere,[128,129] TiO_2 can liberate dioxygen gas by losing lattice oxygen, resulting in defect-rich anatase with oxygen vacancies and reduced Ti^{3+} centers. TiO_2 is known to turn blue under ultra-high vacuum (UHV) conditions due to the high concentration of defects, but this change is reversible, as O_2 from ambient air reoxidizes the reduced TiO_2 once the vacuum is removed, making it white again. Annealing in hydrogen gas can induce oxygen vacancies both on the surface and within the lattice of TiO_2.[130-132] Studies from Mao and coworkers have shown that annealing TiO_2 under hydrogen gas at 18 bar and 473 K for five days creates black TiO_2 with an increase in surface hydroxyls.[133] Studies by other groups of hydrogen treatment at various temperatures, pressures, and annealing times have synthesized black,[134,135] blue,[129,135] and brown,[134,135,136] photoactive TiO_2, thus supporting that optical properties and photocatalytic performance of hydrogen-treated TiO_2 depends significantly on the method of preparation.[137]

The removal of one oxygen atom from the TiO_2 lattice leads to the formation of an oxygen vacancy (V_o) and two electrons, which migrate to and reduce two Ti^{4+} centers to become Ti^{3+} centers. Both X-ray Photoelectron Spectroscopy (XPS) and Electron Paramagnetic Resonance (EPR) have been used to investigate the presence and concentration of defects in anatase. XPS has been used to identify the percentage of oxygen in three bulk states: lattice oxygen, surface hydroxyl, and defect oxygen proximal to an oxygen vacancy, as mentioned in section 3.4.[136] EPR is sensitive to unpaired electrons, and

can identify a variety of paramagnetic defect structures in TiO_2, including holes trapped at O atoms (O^-), electrons trapped at oxygen vacancies (F-centers), and electrons trapped at Ti atoms (Ti^{3+} centers) in bulk and surface lattice positions. [129,136,138]

Though annealing under hydrogen has received much attention, the mechanism by which hydrogen alters the physical and chemical properties of TiO_2 are less well understood. Often, it is assumed that hydrogen is responsible for direct reduction of the metal oxide. To provide insight into the annealing process, in the present work the effect of H_2 gas is compared to annealing under different gases, including diatomic N_2, noble Ar, and oxidizing air. The concentration of defect sites was characterized in each sample by XPS and EPR. The modified anatase samples were then tested for photocatalytic hydrogen evolution under MSR conditions and UV illumination without the use of any metal cocatalyst. The defects produced by annealing under oxygen-excluded atmospheres were found to be highly stable to mildly oxidizing conditions and imparted metal-free photocatalytic hydrogen evolution activity to anatase TiO_2.

4.2 Materials and Methods

4.2.1 Sample Preparation

As-received anatase TiO_2 (Acros Organics, #213581000, 98+% anatase) was calcined prior to annealing in a Thermo Scientific Lindberg Blue tube furnace equipped with multi-step ramp-soak program functionality. Samples were calcined at 773 K for three hours with a ramp rate of 2 K min^{-1} under 100 ml min^{-1} air and cooled to room temperature at 2 K min^{-1} under 100 ml min^{-1} air.

High-pressure, high-temperature annealing was carried out in a 25 ml Parr Series 4790 autoclave equipped with a PTFE gasket. 30 mg of sample was loaded into a glass liner placed inside the autoclave. The autoclave was purged with 14.6 atm of nitrogen seven times and then pressurized to 18 atm with the desired annealing gas. Annealing gases consisted of hydrogen (UHP 5.0 grade, Airgas), nitrogen (4.8, Praxair), argon (UHP 5.0, Airgas), or air (zero-grade, Praxair). Once pressurized, the sealed autoclave was ramped at 2 K min^{-1} to 473 K. After annealing for five days, the autoclave was cooled at 2 K min^{-1} to room temperature and vented. Collected samples were then stored in air-tight vials in a desiccator. Annealed samples are named after the annealing gas and are abbreviated as follows: hydrogen-annealed = HA; nitrogen-annealed = NA; argon-annealed = RA; air-annealed = AA.

4.2.2 Surface Area Characterization

Specific surface areas were measured using 11-point nitrogen physisorption isotherm at 77 K and analyzed with Brunauer-Emmett-Teller theory (BET) using a Quantachrome Autosorb1. Samples were degassed under nitrogen at 423 K for 2 hours to desorb excess water prior to surface area measurements.

4.2.3 X-Ray Powder Diffraction

X-ray powder diffraction (XRD) patterns were collected on a PANalytical Philips X'Pert X-ray diffractometer equipped with a Cu-Kα source at 40 kV and 40 mA and angular incidence 2θ between 20° and 80° with a 0.05° step and 3.0s $step^{-1}$ for a scan speed of 0.0167 ° s^{-1}. XRD patterns were analyzed to determine polymorph, crystallinity, and crystallite size using whole pattern fitting (WPF) and Rietveld refinement with Pearson-VII profile shape function with PDF# 01-073-1764 and PDF# 01-078-1510 for anatase and

rutile, respectively. XRD patterns were background subtracted with a medium cubic spline with a Ka1/a2 ratio of 3. Crystallite size was determined during WPF refinement while removing instrumental contribution.

4.2.4 Diffuse Reflectance UV-Visible Spectroscopy

Diffuse reflectance UV-visible spectroscopy was carried out in a Thermo Scientific Evolution 3000 spectrophotometer equipped with a Harrick Scientific Praying Mantis diffuse reflectance accessory. The spectra were collected between 200 nm and 1000 nm in intervals of 1 nm. A Spectralon disk was used as the absolute reflectance standard. Band gap energies were calculated using the Tauc method, first introduced in section 3.1, and the DPR method (peak center of a Gaussian peak fit to the derivative of the absolute reflectance). Peak fitting was performed using fityk software mentioned in section 3.2.

4.2.5 CHN Analysis

Carbon-hydrogen-nitrogen (CHN) elemental analysis was conducted on a Carlo Erba NA-1500 Analyzer.[139] Samples were measured in small aluminum cups to an accuracy of 1 μg to ensure reliable atomic percentages of carbon, hydrogen, and nitrogen. Loaded cups were combusted at 1773 K via flash combustion to yield quantification with high accuracy, ±0.003 wt%.[139]

4.2.6 X-Ray Photoelectron Spectroscopy

X-Ray Photoelectron Spectroscopy (XPS) was measured under UHV using a Thermo Fisher K-Alpha XPS instrument equipped with a monochromatic Al Kα line with photon energy of 1486.7 eV. The estimated depth sensitivity in this geometry is about 10 nm.[140] To obtain a quantifiable surface oxygen environment and titanium oxidation state,

the spectra were deconvoluted using the method described by Nesbitt and Banerjee.[141] All reported binding energies are in reference to the C 1s peak at 285.0 eV.

4.2.7 Electron Paramagnetic Resonance

X-band Electron Paramagnetic Resonance Spectroscopy (EPR) was performed on an Bruker Elexsys E 500 spectrometer equipped with a single microwave cavity with an X-band bridge operating at 9.2-9.9 GHz. Microwave power of 40 dB was chosen such that intensities of all observed signals varied linearly with the square root of the power thus ensuring the signal was not saturated.[142,143] EPR spectra were recorded at 12 K.[142] In order to quantify Ti^{3+} centers in the samples, a $CuSO_4$ crystal suspended in mineral oil was used to calibrate the spin counts. Samples were filled into 4 mm Wilmad EPR tubes up to 2 cm from the bottom of the tube, with the sample mass recorded to allow for quantification of moles of Ti^{3+} per gram of TiO_2.

4.2.8 Photocatalytic Reactions

Gas-phase heterogeneous photocatalytic MSR reactions were carried out in a Harrick Scientific Praying Mantis high temperature reaction chamber illuminated by a Newport 150W xenon ozone-free Arc Lamp. A dichroic mirror beamturner reflector and colored glass bandpass filter were used to restrict illumination to UV light between 280 nm and 400 nm. The gas-phase reaction mixture consisted of methane (UHP 4.0, Airgas), nitrogen, and water vapor. Water vapor was supplied by heating DI water in a bubbler to 313 K and passing nitrogen carrier gas through the bubbler. 25 mg of fresh catalyst was used for each reaction. The catalyst was heated under 100 ml min^{-1} of reactant gases to the reaction temperature of 973 K at a ramp rate of 5 K min^{-1}. Standard reaction conditions included 8 hours reaction time at 973 K under UV illumination with constant 100 ml min^{-}

[1] flow of reactant gases. The corresponding space time was 4.18×10^{-6} g_{cat} hr ml^{-1}. Reaction products were analyzed using an Agilent 7890b GC equipped with a flame ionization detector and a thermal conductivity detector and using an Agilent 5977a GCMS equipped with a mass-selective detector. Hydrogen and CO_2 were the major gaseous products detected, with additional trace quantities of formaldehyde. CO was never detected as a product.

4.3 Results and Discussion

4.3.1 Characterization

4.3.1.1 X-ray Diffraction and UV-Visible Spectroscopy

Annealing anatase samples under hydrogen, nitrogen, argon, and air produced no visible changes in the resulting powders, which all resembled the starting material. Notably, there was no significant difference in the color of the samples following removal from the annealing vessel. The lack of color change is evident in the diffuse-reflectance UV-visible spectra (**Figure 4.A1**) and the band gap energy (BGE) measurements in **Table 4.1**. BGE values calculated via the DPR method (**Figure 4.A2**) showed no change in the BGE of anatase upon annealing, and the Tauc method (**Figure 4.A3**) showed only minor variation in the calculated indirect BGE. Similarly, the valence band energies measured by XPS (**Figure 4.A4**) also showed no variation between samples (**Table 4.1**).

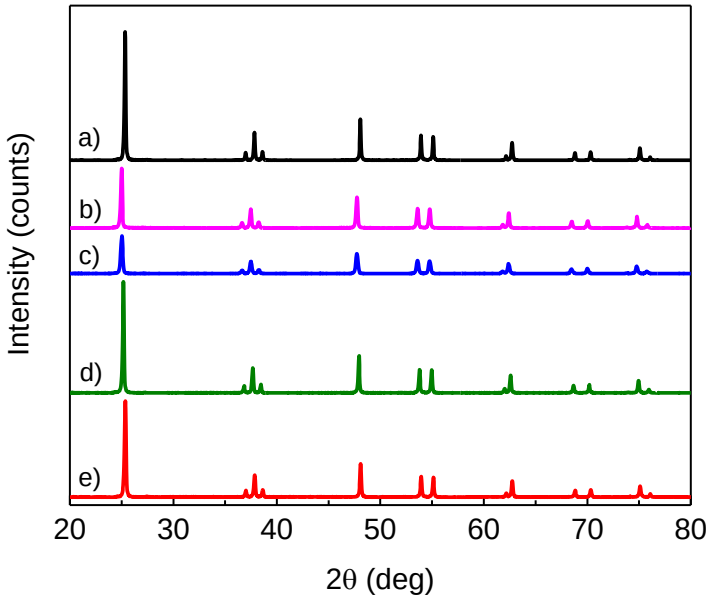

Figure 4.1 XRD powder diffraction patterns of analyzed samples. a) Anatase, b) AA-anatase, c) RA-anatase, d) NA-anatase, e) HA-anatase.

Table 4.1 Physical and optical properties of annealed anatase samples. Particle size estimated by XRD, surface area from 11-point BET, band gap energy calculated from Tauc and DPR methods, and valence band position from XPS.

Sample	Annealing Gas	Crystallite Size [nm]	BET Surface Area [m^2 g^{-1}]	Tauc^{½} BGE [eV]	DPR ($dR_\infty/d\lambda$) BGE [eV]	Valence Band Position [eV]
Anatase	-	64.2	11.5	3.22	3.31	2.7
AA-anatase	air	80.2	10.6	3.26	3.31	2.7
RA-anatase	Ar	>100	9.3	3.25	3.31	2.6
NA-anatase	N_2	100	10.9	3.26	3.31	2.6
HA-anatase	H_2	83.3	11.2	3.26	3.31	2.6

The X-ray powder diffraction patterns of the annealed samples are compared to the parent anatase material **Figure 4.1**. The patterns remain unchanged, with no new peaks appearing that would suggest the presence of new polymorphs. DPR can also reveal the presence of rutile in anatase samples by showing additional peaks during peak-fitting, but all samples were fit to a single peak for anatase (**Figure 4.A2**). Additionally, there was no loss in crystallinity, though crystallite size increased as indicated in **Table 4.1**. Though

some particles increase in diameter by 56% (40 nm or more), the surface areas measured by 11-point BET decreased by a much lesser amount upon annealing. Though RA-anatase showed the largest particle size increase and as a result had the smallest specific surface area, the sample only lost 19% of its surface area. As the particle diameters were only weakly correlated to the surface areas, annealing treatment resulted in particles that were not spherical in shape, suggesting that the annealing treatment increases surface roughness of the nanoparticles.

4.3.1.2 X-ray Photoelectron Spectroscopy

The chemical environments of surface and near-surface oxygen and titanium atoms in annealed samples were analyzed by XPS. The O1s signal of oxygen atoms in surface environments were fit with three peaks, as shown in **Figure 4.2**. The primary peak at a binding energy of 530.4 eV corresponds to the bulk/lattice oxygen in TiO_2.[136,144] The secondary peak at 531.9 eV is assigned to defect oxygen sites corresponding to an oxygen atom geminal to a lattice oxygen vacancy (V_O), and the tertiary peak at 532.9 eV is assigned to oxygen in a surface hydroxyl state.[144-146]

The peak areas of the O1s signal in defect and hydroxyl chemical environments as a fraction of all oxygen atoms ($O_{531.9}/\Sigma O_i$) are plotted in **Figure 4.3**. All annealed samples showed an increase in surface hydroxyls relative to the parent sample. While 3.8% of oxygen atoms were in the surface hydroxyl environment, this value increased to 12-13% in the annealed samples, regardless of the annealing gas. Despite the increase in particle size and slight decrease in BET surface area, the surface hydroxyl concentration increased upon annealing. This suggests that the TiO_2 particles underwent surface roughening. Larger, less spherical particles with rougher surfaces would be expected to show a smaller

decrease in surface area than smooth, spherical particles of the same diameter, consistent with the XRD, BET, and XPS measurements.

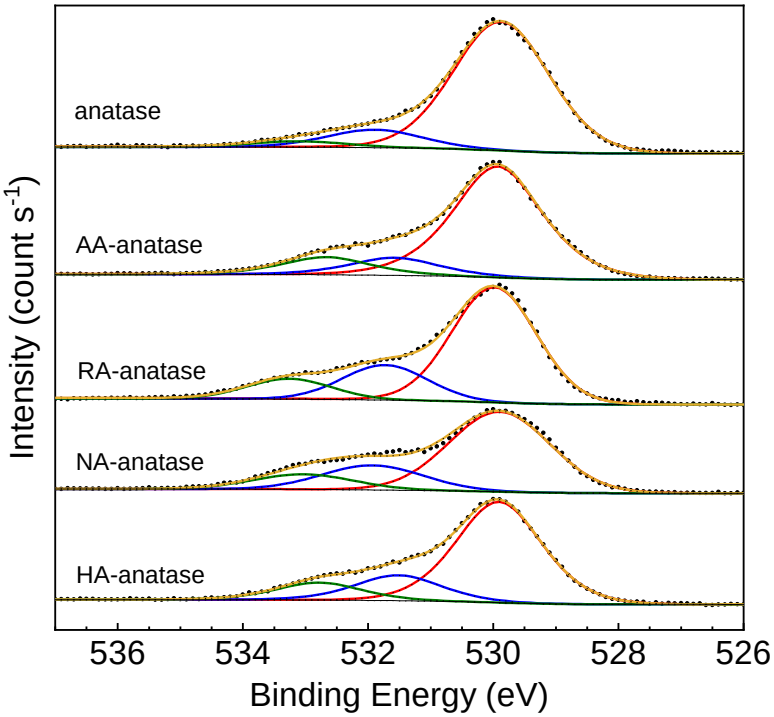

Figure 4.2 O1s region of XPS spectra with oxygen in three environments, deconvoluted to fit three peaks to bulk oxygen (red), oxygen defect sites adjacent to oxygen vacancies (blue), and surface hydroxyl (green).

Though all annealed samples showed an increase in surface hydroxyls, only samples annealed in the absence of oxygen (i.e. Ar, N_2, H_2) showed an increase in the percentage of oxygen in the defect environment. As XPS spectra are collected under UHV, some oxygen is expected when anatase particles are exposed to vacuum, leading to the formation of some oxygen vacancies.

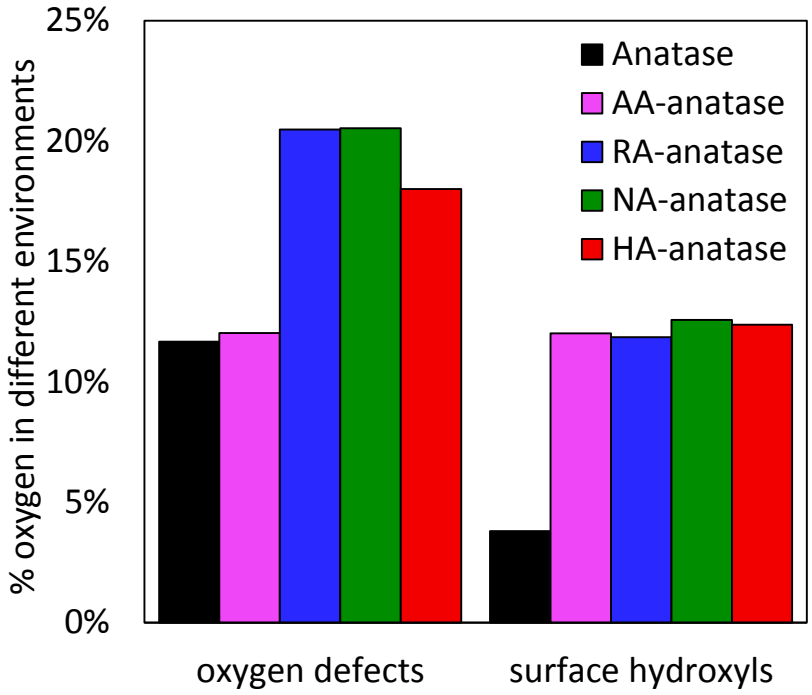

Figure 4.3 Percentage of oxygen in oxygen defects (sites adjacent to oxygen vacancies) and in surface hydroxyls as determined by deconvolution of the O1s XPS spectra for anatase (black) compared to annealed samples.

This is shown in **Figure 4.3**, as 11.7% of oxygen atoms were in defect environments, indicating nearby oxygen vacancies. The sample annealed in air showed the same concentration of oxygen defects as untreated anatase, indicating that defect oxygen formation could not be induced when annealing anatase in the presence of an oxidizing gas. Annealing in oxygen-depleted gases however showed an increase in defect oxygen signal to 18-21% of oxygen atoms near the surface of the particles. All three gases showed approximately the same enhancement in defect oxygen, indicating that a reducing environment is not necessary to induce TiO_2 reduction and oxygen vacancy formation. The absence of oxygen during annealing was enough to create high-defect anatase, while the presence of oxygen led to no enhancement in oxygen defects concentration.

Quantifiable surface titanium oxidation states were determined via deconvolution of the Ti2p XPS peaks (**Figure 4.A5**). For calcined anatase TiO_2, the experimentally obtained XPS $Ti2p_{1/2}$ and $Ti2p_{3/2}$ peak binding energies of 464.7 eV and 458.8 eV respectively agree well with literature values for Ti^{4+} in titanium dioxide. [136,144] In addition, the low energy tail with binding energy of 457.0 eV corresponded to $Ti2p_{3/2}$ in a Ti^{3+} center.[136,144,147,148] In anatase and AA-anatase, the area of this peak normalized by the total $Ti2p_{3/2}$ peak area ($Ti_{457.0}/\Sigma Ti_i$) corresponded to approximately 5% of titanium atoms reduced from 4+ to 3+ oxidation state (**Figure 4.A4**). As discussed above, some of this reduction is due to oxygen loss under UHV conditions during the XPS experiment. Just as the oxygen defect signal increased by 50% upon annealing anatase in an oxygen-depleted environment, RA-, NA-, and HA- anatase showed a 50% increase in the Ti^{3+} signal relative to anatase and AA-anatase. Approximately 7.5% of titanium centers appeared to be in the Ti^{3+} state.

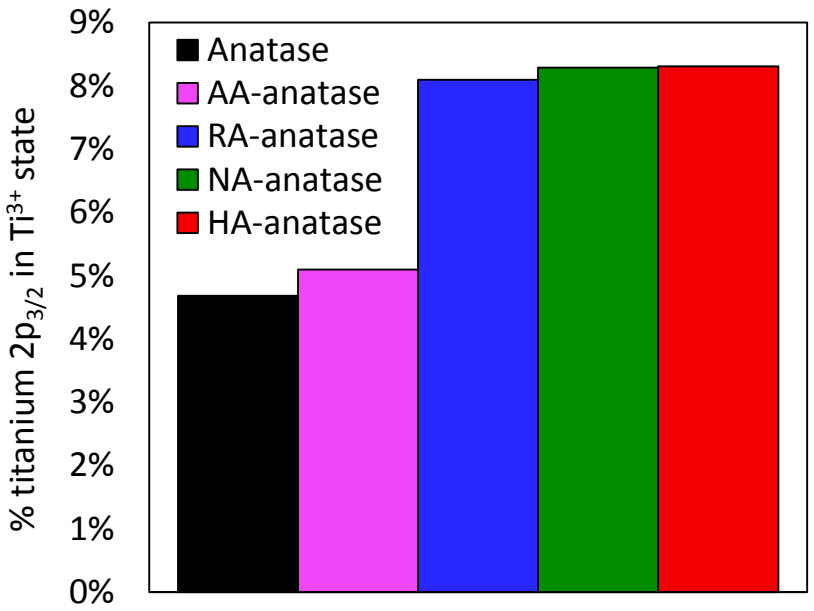

Figure 4.4 Percentage of $2p_{3/2}$ titanium in the Ti^{3+} state determined by XPS peak area ratios for commercial anatase (black), AA-anatase (pink), RA-anatase (blue), NA-anatase (green), and HA-anatase (red).

The XPS experiments established that a reducing environment was not necessary to generate Ti^{3+} centers. The role of H_2 is not to react with the TiO_2 as no difference in XPS signals between HA-anatase and either NA- or RA-anatase was observed. To ensure that N_2 was also inert during the annealing process, the N_{1s} region (395 eV to 410 eV) of the XPS spectrum was examined for samples annealed in the presence of nitrogen. No signal could be seen in the XPS spectra of in NA-anatase or AA-anatase (**Figure 4.A6**), indicating that nitrogen was not present in the surface or near-surface of the annealed samples. Additionally, CHN analysis was conducted and did not detect any nitrogen (**Table 4.A1**).

Because XPS is conducted in a vacuum which can induce oxygen vacancies in TiO_2, the true concentration of Ti^{3+} centers at ambient conditions cannot be directly measured. No effort was made to avoid exposing the annealed samples to air between the annealing procedure and the XPS measurement, so some of the Ti^{3+} centers may have been generated during annealing and some were generated under the UHV conditions. To better understand the nature and stability of Ti^{3+} centers in annealed samples, EPR spectroscopy was used as an ambient pressure technique for quantification of reduced Ti centers.

4.3.1.3 Electron Paramagnetic Resonance Spectroscopy

The Ti^{3+} concentration was further investigated via Electron Paramagnetic Resonance Spectroscopy (EPR). EPR is sensitive only to paramagnetic species. Paramagnetic Ti^{3+} gives strong signals while Ti^{4+} gives no signal, so the signal for Ti^{3+} is clearer and easier to interpret. Additionally, XPS is a surface and near-surface technique, and measurements preferentially represent surface states. EPR by contrast is able to probe the entirety of a TiO_2 nanoparticle. Finally, EPR, conducted at ambient pressure does not

employ any vacuum that would otherwise reduce TiO_2. Because no effort was made to exclude ambient air while storing samples, EPR can identify the long-term stability of reduced Ti^{3+} centers during storage and air exposure without having the measurements convoluted by the effect of UHV conditions.

The EPR spectra of the parent anatase sample and all annealed samples are shown in **Figure 4.5**. As was observed with the XPS spectra, the samples could be grouped based on the presence of oxygen during annealing. For all spectra, five features could be identified. Band positions and *g*-factors did not vary between samples, only intensities varied. The EPR peaks were assigned as follows from previous literature reports[129,136,138] electrons trapped at oxygen vacancies (F-centers) appeared at *g*-factor = 2.003, oxygen atoms with trapped holes (O^-) appeared at $g = 1.987$, and electrons trapped at bulk Ti atoms (Ti^{3+} signals) were also detected. Since Ti^{3+} centers in anatase have axial symmetry ($g_x = g_y$), a single signal at $g_{\|} = 1.97$ was observed. EPR intensity is highest for equatorial orientations, corresponding to $g_{\perp} = 1.946$, therefore the $g_{\perp}$ signal is expected to be significantly larger than that for $g_{\|}$. Surface Ti^{3+} centers gave rise to a broad signal at g=1.89 and have been reported in literature as a result of Ti^{3+} centers in a disordered surface environment.

Anatase and AA-anatase showed very similar spectral features, and HA-, NA-, and RA-anatase samples were all similar to one another. The parent anatase sample and the sample annealed in air showed weak signals for all paramagnetic species, including Ti^{3+}. By contrast, the samples annealed in hydrogen, nitrogen, and argon showed sharp signals at *g*-factor = 1.946, corresponding to bulk Ti^{3+}. Samples of different ages, and therefore exposure times, to ambient air were tested. No appreciable changes in the EPR spectra for

the high-defect annealed samples could be seen, even after nine months of air exposure, indicating very high stability to reoxidation at ambient conditions for reduced samples.

The small but finite Ti^{3+} concentration in anatase and AA-anatase likely arose from photoexcitation by ambient light. When lacking surface species to react with, generated photoelectrons can become trapped at titanium centers.

$$Ti^{4+} + h\nu \rightarrow \quad Ti^{4+} + e^- + h^+ \rightarrow Ti^{3+} + h^+$$

To evaluate the impact of annealing on the concentration of Ti^{3+} centers, a standard paramagnetic spin reference, $CuSO_4$, was used for spin counting calibration. The results are given in **Table 4.2**. Both the parent sample and the air annealed sample showed similar, low concentrations of bulk Ti^{3+}, 55 and 72 $nmol_{Ti3^+}\ g_{TiO2}^{-1}$ respectively. Samples annealed in nitrogen, argon, and hydrogen showed an 6-7 fold increase in bulk Ti^{3+} concentration, 300-400 $nmol_{Ti3^+}\ g_{TiO2}^{-1}$. The ratio of surface Ti^{3+} centers between the two groupings of samples was also similar; approximately 2 $nmol_{Ti3^+}\ g_{TiO2}^{-1}$ for the low concentration samples and 13 $nmol_{Ti3^+}\ g_{TiO2}^{-1}$ for the reduced samples. This suggests that the annealing process creates reduced titanium center defects equally well in the bulk as in the surface. A constant ratio of ~30 ± 4 was found between bulk and surface Ti^{3+} defects for all samples, regardless of the actual concentration of defects. In fact, the ratios between defect sites of different kinds did not change much with annealing treatments. The ratio between bulk Ti^{3+} and F-centers was ~125 ± 25, and the ratio between holes trapped at oxygen atoms and F-centers was ~2.3 ± 0.7. These ratios vary far less between samples (15-30%) than the variance between the magnitudes of the concentrations, which where a multiple of 4-7 times larger for the high-defect annealed samples than in anatase and AA-anatase.

Together, EPR and XPS revealed that annealing anatase in hydrogen, nitrogen, or argon greatly increased the concentration of defect sites, leading to a large concentration of bulk Ti^{3+} sites. The ratio of Ti^{3+} sites in high and low defect samples measured by XPS was convoluted with the vacuum-induced oxygen evolution, while EPR gave clear measurement of the intrinsic concentrations of these defects under ambient conditions. These reduced titanium sites were stable towards reoxidation in air over many months. Their photocatalytic activity is explored in the following sections. While the concentration of Ti^{3+} centers was enriched in annealed samples, these sites still represented a very small minority of Ti atoms in the particles. For example, HA-anatase possessed 326 nmol g_{TiO2}^{-1} of Ti^{3+} centers as measured by EPR, which corresponds to approximately one Ti atom reduced per 38,000 lattice Ti atoms.

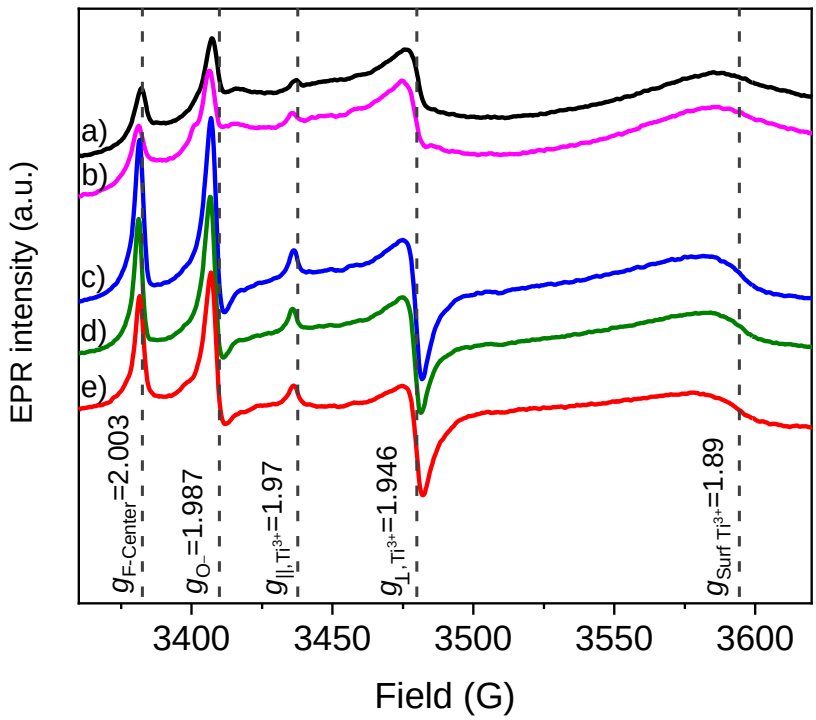

Figure 4.5 EPR spectra of a) anatase, b) AA-anatase, c) RA-anatase, d) NA-anatase, e) HA-anatase. Peaks labelled for F-center (g = 2.003), oxygen with trapped hole (g = 1.987), bulk Ti^{3+} ($g_{\|}$ = 1.97, $g_{\perp}$ = 1.946), and surface Ti^{3+} (g = 1.89).

Table 4.2 Concentration in (nmol g_{TiO2}^{-1}) of paramagnetic defects in samples measured by EPR spin counting, including bulk and surface Ti^{3+} centers, F-Centers, and O^- centers. Spin counts determined with standard reference $CuSO_4$.

Sample	Bulk Ti^{3+}	Surface Ti^{3+}	F-Center
Anatase	55	1.7	0.4
AA-anatase	72	2.0	0.6
RA-anatase	386	13	4.1
NA-anatase	323	13	2.8
HA-anatase	326	13	2.1
HA-anatase (post-reaction, UV)[a,b]	14	1.0	3.1
HA-anatase (post-reaction, UV)[a,c]	16	0.6	0.6
HA-anatase (post-reaction, dark)[a,d]	6	0	0.3
HA-anatase (calcined)[e]	9.8	17	0.5

[a] HA-anatase sample after reaction under MSR conditions (100 ml min^{-1} of 4% CH_4, 4% H_2O at 973 K). [b] 8 hours under UV illumination. [c] 36 hours under UV illumination. [d] 36 hours without illumination. [e] HA-anatase sample after 3 hours calcination (100 ml min^{-1} of air at 773 K).

4.3.2 Photocatalytic Activity

4.3.2.1 Photocatalyst Stability

A number of artifacts of catalyst preparation may lead to the apparent formation of reaction products without involving catalytic turnovers. Desorption and/or decomposition of adsorbates from catalyst preparation and consumption of trapped excitons and/or material defects could give measurable reaction rates from stoichiometric consumption of species present at the beginning of reaction conditions. Such reaction rates would be expected to decline as the stoichiometric species involved are consumed over long periods of time. A special concern may be raised for samples treated in hydrogen, in case hydrogen was adsorbed during annealing and simply released under reaction conditions. For this reason, an effort was made in the following work to allow reactions to proceed long enough

to establish steady-state hydrogen evolution activity without declines in reaction rates. Reactions were typically run for 8-44 hours under reaction conditions to establish that the reaction was truly at steady-state. In general, photocatalysts annealed in hydrogen, nitrogen, and argon showed long-term stable activity under UV illumination only, i.e. photocatalytic conditions. Reaction over these samples without illumination, i.e. "dark" or thermocatalytic conditions, showed slow decline in activity with reaction time as discussed in the following sections. Anatase, without annealing treatment or annealed in air, showed either rapid loss of activity or no photocatalytic activity towards hydrogen generation. All reported reaction rates were measured at 973 K. Catalyst was exposed to reaction gases while ramping temperature up to 973 K, and hydrogen evolution rates remained negligible below 973 K.

Non-catalytic reaction mechanisms are of special concern in metal-free hydrogen evolution reactions, as TiO_2 normally does not possess the correct active site geometry for the production of hydrogen gas.[127] Often, a metal nanoparticle cocatalyst is instead used to catalyze this reaction. The establishment of long-term steady-state hydrogen evolution from metal-free anatase particles indicates that the annealing procedure was able to generate active sites with the correct geometry for hydrogen evolution, and that these sites were stable under reaction conditions. **Figure 4.6** shows that anatase annealed under hydrogen demonstrated steady hydrogen evolution activity for 40+ hours under continuous MSR conditions under UV illumination at a steam/carbon ratio of one.

At elevated temperatures, the anatase polymorph of TiO_2 converts to the rutile polymorph. As discussed in section 3.3, the onset temperature for rutilization during calcination occurs between 673 K and 873 K, depending on the particle properties. In situ

DPR is effective for continuous monitoring of phase-change, and all photocatalytic experiments were carried out in an in situ diffuse-reflectance spectroscopy reactor. Following reaction, the diffuse-reflectance UV-visible spectra of used catalysts were measured and analyzed for polymorphism. Despite the high reaction temperature, anatase was the only phase present, and no rutile phase was found (**Figure 4.A7**). Changes in particle shape and exposed facets of the anatase crystallites has been associated with stabilization of the anatase phase at high temperature, suggesting that the annealing process imparted stabilization through similar processes to the materials studied here.

From the total accumulation of H_2 formed during the continuous-flow experiment, it is evident that HA-anatase is active for metal-free hydrogen evolution, and that the activity is not the artifact of some stoichiometric reaction. After 42 hours of reaction, 35 mmoles of H_2 had evolved per gram of TiO_2. If the most abundant defect sites, Ti^{3+} centers in the bulk, were responsible for the observed reactivity, 108 kmoles of H_2 formed per mole of Ti^{3+} centers, reaction could not be attributed to the consumption of such sites, and must therefore be catalytic.

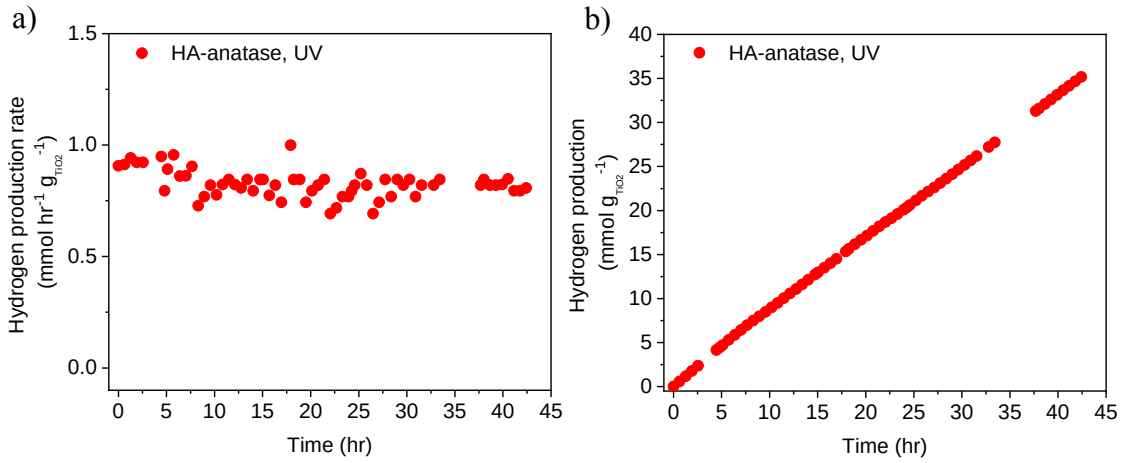

Figure 4.6 Hydrogen production from photocatalytic MSR (50 ml min^{-1} of 4 mol% CH_4, 4 mol% H_2O, balance N_2) under UV illumination at 973 K over 25 mg of HA-anatase.

Catalyst was ramped to reaction temperature under flowing reaction gases. a) reaction rates, b) cumulative hydrogen generation.

4.3.2.2 Impact of Annealing Conditions

Under photocatalytic MSR conditions, anatase showed no activity for hydrogen evolution without annealing treatment (**Figure 4.7**). This is consistent with the fact that a metal cocatalyst like platinum is required to generate H_2 from photocatalytic TiO_2.[127] Under identical conditions, HA-anatase shows stable activity for hydrogen evolution, establishing that annealing is responsible for generating the required active sites.

Comparing hydrogen evolution over HA-anatase to NA-anatase or RA-anatase shows little impact of which non-oxidizing annealing gas is used (**Figure 4.7**). Just as was found for the concentration of defects, such as Ti^{3+} centers, the important factor was annealing in the absence of oxygen, and little difference could be ascribed to the choice of oxygen-depleted gas during the annealing process. By contrast, annealing in air was unable to produce stable photocatalytic activity. While the hydrogen production rate for AA-anatase was initially comparable to that over the active annealed samples, the activity dropped to zero within two hours of reaction. As with anatase, AA-anatase lacks high concentrations of catalytically relevant defects and shows zero steady-state hydrogen evolution. The source of the initially activity is unclear. Annealing in any gas was found to increase the concentration of surface hydroxyl species, and these sites may be able to evolve hydrogen stoichiometrically. Surface hydroxyls on anatase (101) surfaces, in the form of chemisorbed water molecules, have been shown in DFT calculations to significantly reduce the activation energy barriers for C-H activation in methane.[149] The reaction produces physisorbed water, but is catalytic in water if the water molecule can be

activated, regenerating the chemisorbed water surface hydroxyls. If this is the correct mechanism, then annealing under any gas is able to generate the active surface hydroxyls. Anatase annealed in air lacks the proper active site to regenerate these surface hydroxyls, making the reaction stoichiometric. Only samples annealed in hydrogen, nitrogen, or argon are able to drive the hydrogen evolution reaction catalytically.

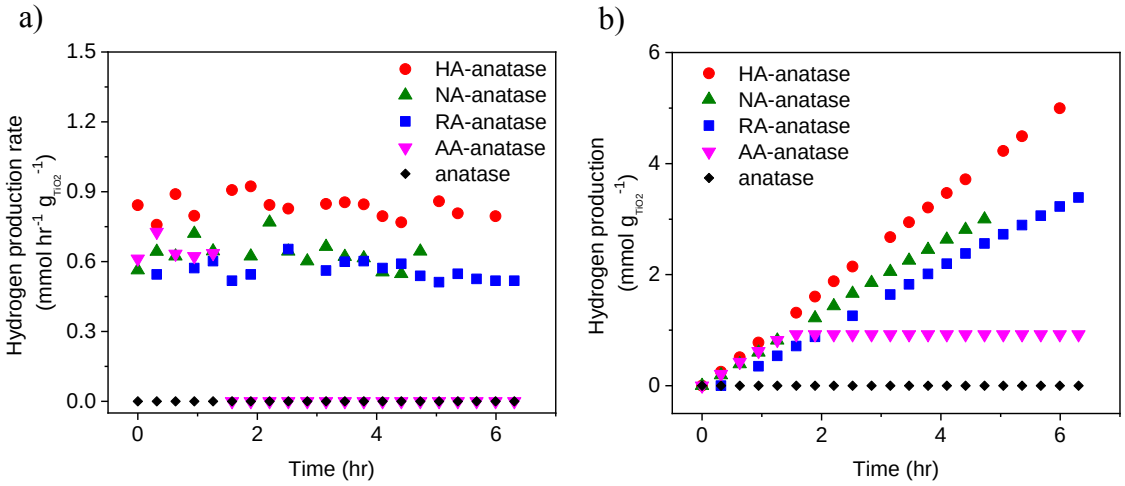

Figure 4.7. Hydrogen production from photocatalytic MSR (100 ml min^{-1} of 4 mol% CH_4, 4 mol% H_2O, balance N_2) under UV illumination at 973 K over 25 mg of catalyst. Catalyst was ramped to reaction temperature under flowing reaction gases. a) reaction rates, b) cumulative hydrogen generation.

4.3.2.3 Impact of Illumination Conditions and Role of Ti^{3+} Centers

The steady state hydrogen evolution reaction over annealed anatase required illumination and could not proceed thermocatalytically. Without illumination by UV light, there was no steady-state hydrogen production observed (**Figure 4.8**). Hydrogen productivity was measured for short reaction times but declined rapidly and fell to zero by one hour of reaction time. The initial activity likely arose from some active sites that reacted stoichiometrically to yield hydrogen and were consumed within one hour. If the nature of the hydrogen evolution reactive site is the same under UV illumination and in the

dark, then the implication is that UV light is responsible for regenerating the active site and closing the catalytic cycle. Without UV light, the reaction is only stoichiometric.

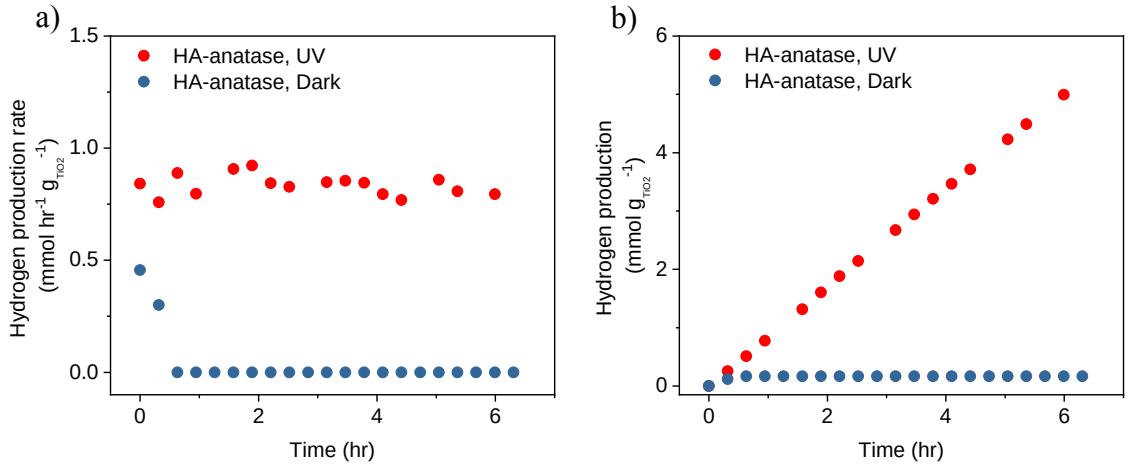

Figure 4.8 Hydrogen production from MSR (100 ml min^{-1} of 4 mol% CH_4, 4 mol% H_2O, balance N_2) at 973 K over 25 mg of HA-anatase UV illumination and dark reaction without illumination. Catalyst was ramped to reaction temperature under flowing reaction gases. a) reaction rates, b) cumulative hydrogen generation.

Reasonable candidates for the active species responsible for hydrogen evolution are the paramagnetic defect centers detected by EPR that were enriched upon annealing. For example, Ti^{3+} species were the most abundant defects upon annealing. These Ti^{3+} defects were already distinct from those in ordinary TiO_2 in that they were stable with respect to ambient air, while Ti^{3+} centers induced by exposure to UHV, e.g. during XPS spectroscopy, were reoxidized in ambient air. A small amount of Ti^{3+} centers could also be generated from ambient light photoexcitation, where the photoelectron becomes trapped at a titanium atom, reducing it from the 4+ to the 3+ oxidation state. It is therefore hypothesized that under dark reaction, the Ti^{3+} centers were consumed, while UV illumination regenerated them in the catalytic cycle. This principle is illustrated in **Figure 4.A8**, where HA-anatase was illuminated while loaded in the EPR spectrometer, and the spectrum collected during

UV illumination. The result shows an increase in all paramagnetic defects as a result of photoexcitation, including a larger concentration of Ti^{3+} centers.

EPR spectroscopy was once again utilized to determine the concentration of paramagnetic defects in annealed anatase samples after reaction. **Figure 4.9** compares the EPR spectra of HA-anatase before and after MSR reaction conditions with and without illumination. The concentrations of paramagnetic defects are given in **Table 4.2**. Compared to pre-reaction HA-anatase, after reaction in dark conditions 100% of the surface Ti^{3+} centers (g = 1.89) were consumed and 98% of the bulk Ti^{3+} centers ($g_{\perp}$ = 1.946 + $g_{\parallel}$ = 1.97) were consumed. F-centers (g = 2.003) were reduced by 86% while trapped holes (g = 1.987) were appeared to increase. These results indicate that trapped holes are unlikely to be the catalytically active species, as they are still present in significant concentration in the inactive catalyst following dark reaction.

After reaction under UV illumination, a similar increase in trapped holes was measured while the concentration of F-centers increased after 8 hours and decreased after 36 hours. As the hydrogen productivity was unchanged at these two different time coordinates, the changes in in concentration of these defect sites shows that they are not directly involved in the catalytic cycle.

The Ti^{3+} concentrations after 8 hours and 36 hours of MSR reaction under UV illumination were quantitatively very similar to one another, with approximately 95% and 94% reductions in bulk and surface Ti^{3+} concentrations respectively. Consequently, the ratio of bulk to surface Ti^{3+} centers was nearly constant as well, and unchanged relative to the parent sample. The steady-state Ti^{3+} concentrations are consistent with the hydrogen evolution rates being at steady state as well. The result further suggests that only a fraction

of the Ti^{3+} centers in the annealed samples are responsible for the steady-state catalytic activity. It should be noted that ex-situ EPR analysis may not reflect the true concentration surface and bulk Ti^{3+} defects at high temperature under reaction conditions. The concentrations may be different at room temperature or cryogenic EPR temperatures, especially if bulk/surface Ti^{3+} can react during cooldown from 973 K. The presence of water, a mild oxidant, during the initial temperature ramp and the cooldown may reduce the concentration of active Ti^{3+} centers compared to the parent HA-anatase sample. It is clear, however, that water does not impact the Ti^{3+} concentration at the reaction temperature, since neither the Ti^{3+} concentration nor the hydrogen evolution rate changes between 8 hours and 36 hours of time on stream. Any oxidizing effect of water, if present must therefore occur at lower temperatures. This effect is further explored in Section 3.2.5, where HA-anatase was heated to 973 K in nitrogen instead of water-containing reaction gases prior to MSR reaction.

The EPR measurements demonstrate that the high activity of HA-anatase is derived from Ti^{3+} sites that are stable under reaction conditions. While some Ti^{3+} sites were consumed during reaction under UV illumination, the catalytically relevant sites remained active despite contact with steam at 973 K. The Ti^{3+} sites active for catalyzing photocatalytic MSR were regenerated under reaction conditions by UV light.

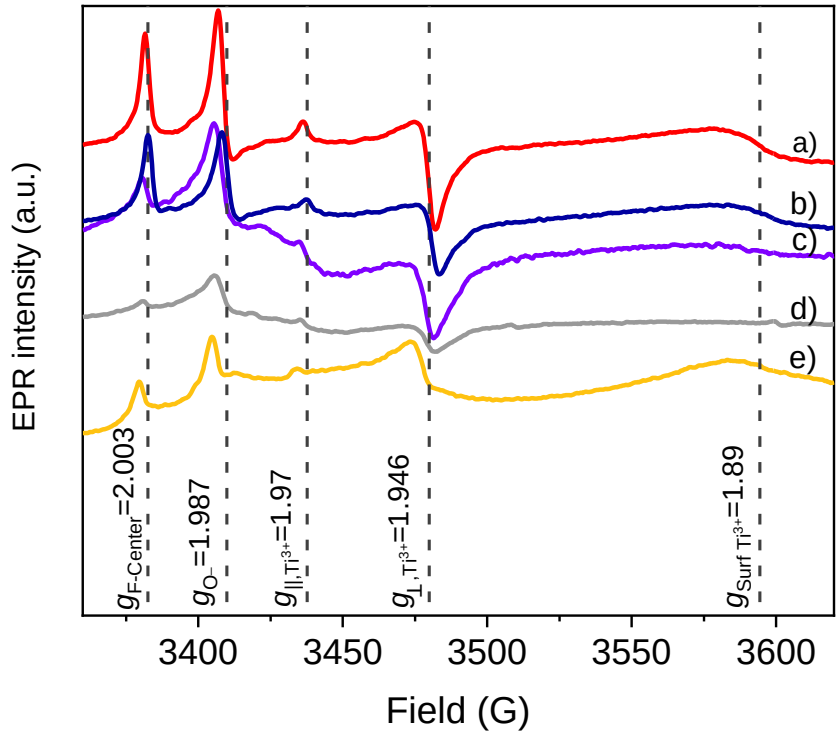

Figure 4.9 EPR spectra of a) HA-anatase, b) HA-anatase after 8 hr MSR reaction under UV illumination, c) HA-anatase after 36 hr MSR reaction under UV illumination, d) HA-anatase after 36 hr MSR reaction without illumination, e) HA-anatase calcined to 773 K in 100 ml min^{-1} air for 3 hours. MSR conditions for b)-d) 100 ml min^{-1} of 4 mol% CH_4, 4 mol% H_2O, balance N_2, at 973 K over 25 mg of HA-anatase.

To further connect the concentration of Ti^{3+} centers to photocatalytic activity, a fraction of these sites was removed via oxidation by air at 773 K. By calcining for different durations, paramagnetic defects associated with reduced metal centers and oxygen vacancies were healed to varying extent, and a fraction of the photocatalytic activity of HA-anatase was selectively eliminated. Calcining for 0.5 hours reduced steady state activity by approximately 25%, and calcining for a total of 3 hours reduced activity by 50% relative to uncalcined HA-anatase (**Figure 4.10**). Calcining HA-anatase for 3 hours was sufficient to remove a majority (97%) of the bulk Ti^{3+} centers, while the concentration of the surface Ti^{3+} centers remained unchanged (**Figure 4.9e**, **Table 4.2**). This establishes that oxygen evolution from the lattice is reversible as with other TiO_2 materials, but the long-

term stability in ambient air shows that the process is only reversible at elevated temperatures. The reduction Ti^{3+} centers in the bulk after three hours of calcination in air was almost the same as seen in the post-reaction samples which had been ramped in temperature and cooled down in the presence of steam. The impact on the catalytic activity for these very different pretreatment conditions was almost the same as well, with only a factor of two difference in hydrogen evolution rates. These few Ti^{3+} centers that persist after calcination and during reaction conditions were remarkably stable towards oxidizing conditions.

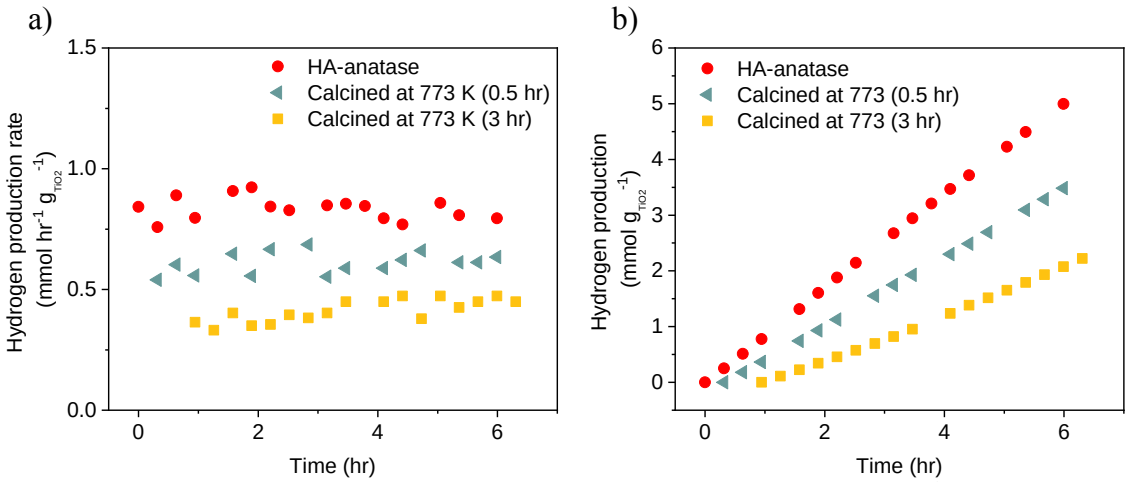

Figure 4.10 Hydrogen production from photocatalytic MSR (100 ml min^{-1} of 4 mol% CH_4, 4 mol% H_2O, balance N_2) under UV illumination at 973 K over 25 mg of HA-anatase. Catalyst was calcined at 773 K in 100 ml min^{-1} air for 0 hr, 0.5 hr, or 3 hr as indicated. Catalyst was then ramped to reaction temperature under flowing reaction gases. a) reaction rates, b) cumulative hydrogen generation.

4.3.2.4 Effect of Reactant Partial pressures

The effect of reactant partial pressures on steady state photocatalytic hydrogen evolution over hydrogen annealed anatase was investigated. Steady state hydrogen production was monitored for two hours at methane partial pressures between 0.012 atm and 0.26 atm while maintaining a constant 0.04 atm of steam. The lowest methane partial

pressure yielded 0.8 $mmol_{H2}$ hr^{-1} g_{TiO2}^{-1}, and rate increased linearly as the methane partial pressure was increased up to 0.26 atm (**Figure 4.11a**). The effect of steam partial pressure between 0.04 atm to 0.105 atm was measured at two different partial pressures of methane (0.035 atm and 0.085 atm) (**Figure 4.11b**). The hydrogen production rate was essentially independent of the water partial pressure.

The zero-order rate dependence on water partial pressure indicates that the catalyst surface is saturated in water during reaction conditions, and water adsorption rate-limiting. This is consistent with the large surface hydroxyl concentration measured by XPS. As discussed in Section 4.3.2.2, water activation to regenerate surface hydroxyls may be a more kinetically relevant step, with high-defect samples able to activate physisorbed water while low-defect samples cannot. In this case, the concentration of defects, and not the surface concentration of physisorbed water molecules, would be kinetically relevant under relevant reaction conditions. This is consistent with zero-order dependence on water pressure.

A non-zero partial pressure for methane was expected, as methane is expected to interact only weakly with the anatase surface. Methane C-H activation is a difficult reaction, and dissociative methane adsorption is predicted to have a high activation energy barrier on anatase, even when assisted by active surface hydroxyls.[149] A first-order dependence on methane partial pressure is consistent with kinetically rate-limiting methane activation.

Commercial MSR is operated at a steam/methane ratio of four to prevent the formation of coke. Lower steam/methane ratios are associated with higher risk of coke formation, leading to catalyst deactiviation, with the catalytic metal nanoparticles,

especially nickel, being responsible for the coke formation. Coke formation was not observed at all in the photocatalytic experiments with steam/methane ratio of as low as 0.4. Smaller steam/methane ratios of 0.2-0.3 did lead to some gray discoloration of the catalyst.

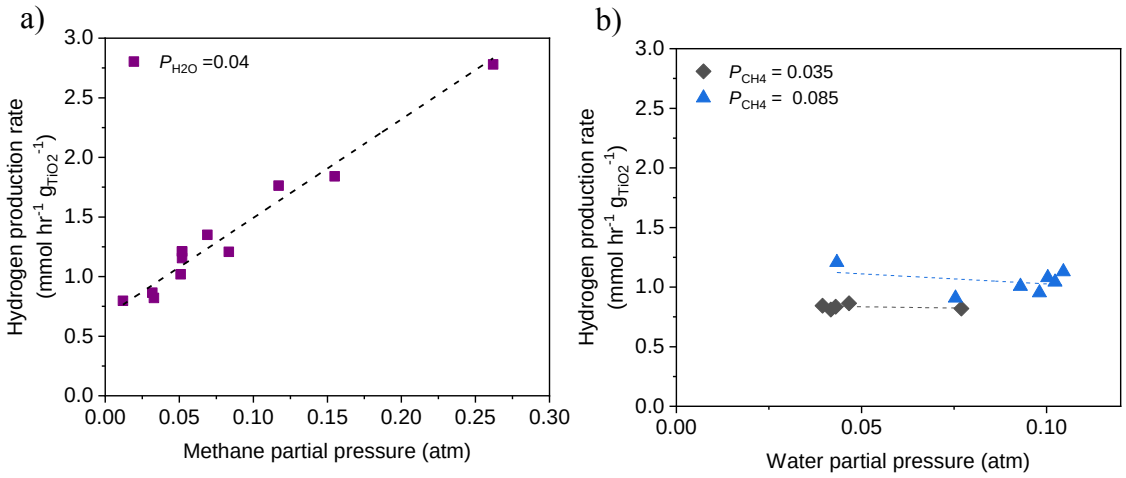

Figure 4.11 Hydrogen production from photocatalytic MSR under UV illumination at 973 K over 25 mg of HA-anatase. Catalyst was ramped to reaction temperature under flowing reaction gases. 50 ml min^{-1} of a) P_{H2O} = 0.045 atm, varying P_{CH4}, balance N_2, and b) P_{CH4} = 0.035 atm and 0.085 atm as indicated, varying P_{H2O}, balance N_2.

4.3.2.5 Impact of Atmosphere during Temperature Ramp

The reaction rates reported above were measured after catalysts were ramped to the reaction temperature under reaction gases. This means that the samples were thermally treated up to 973 K in the presence of water, a mildly oxidizing gas, while maintaining activity and without removing all the defect sites. Thermal treatment in oxygen was found to remove defects and reduce activity. The effect of thermal treatment without any oxidizing gas during the initial temperature ramp was investigated by flowing 20 ml min^{-1} of nitrogen over the catalyst in place of the reaction gases until 973 K, and then switching to methane/steam/nitrogen flow once the desired reaction temperature was reached. By heating in an inert gas, the concentration of Ti^{3+} centers is expected to increase, as

mentioned in section 4.1, but whether these would be stable defects like those generated from annealing or unstable defects like those generated from vacuum treatment was explored.

The activity of HA-anatase heated to reaction temperature under N_2 gas is shown in **Figure 4.12**. Under UV illumination, an initially high activity declined over four hours of reaction and leveled out at a steady-state hydrogen production rate of about 25% of the initial value. The majority of the additional Ti^{3+} centers generated by thermal treatment in N_2 were consumed during this initial transient, giving rise to stoichiometric H_2 production at short reaction times. Approximately 10 $mmol_{H2}\ g_{TiO2}^{-1}$ were generated stoichiometrically in this way. After the initial transient, only those stable Ti^{3+} centers generated from annealing remained, and the hydrogen generation rate remained stable for over 30 hours. The steady-state hydrogen evolution rate of 3.4 mmol $hr^{-1}\ g_{TiO2}^{-1}$ was higher than that seen in samples heated to reaction temperature under reactant gases containing water, providing further evidence that some fraction of active Ti^{3+} centers are oxidized and lost at temperatures below 973 K when heated in the presence of steam.

Thermal treatment under N_2 prior to reaction also increased the hydrogen yield from reaction carried out without illumination, but once again the reaction was stoichiometric rather than catalytic. The rate of stoichiometric hydrogen evolution was much slower than under UV illumination, requiring 12 hours to fully consume the Ti^{3+} centers, though the total amount of hydrogen formed was the same under UV and dark reaction conditions, approximately 10 $mmol_{H2}\ g_{TiO2}^{-1}$.

The formation of Ti^{3+} centers during thermal in N_2 is expected for many anatase samples. However, the ability to form hydrogen from such defects was unique to annealed

anatase. While these additional defects formed H_2 stoichiometrically, anatase (without annealing) heated to reaction temperature under N_2 was still completely inactive for hydrogen evolutions, both catalytically and stoichiometrically. The required active sites for hydrogen evolution from anatase are generated only by annealing, and inducing Ti^{3+} defects from heating in N_2 was not sufficient.

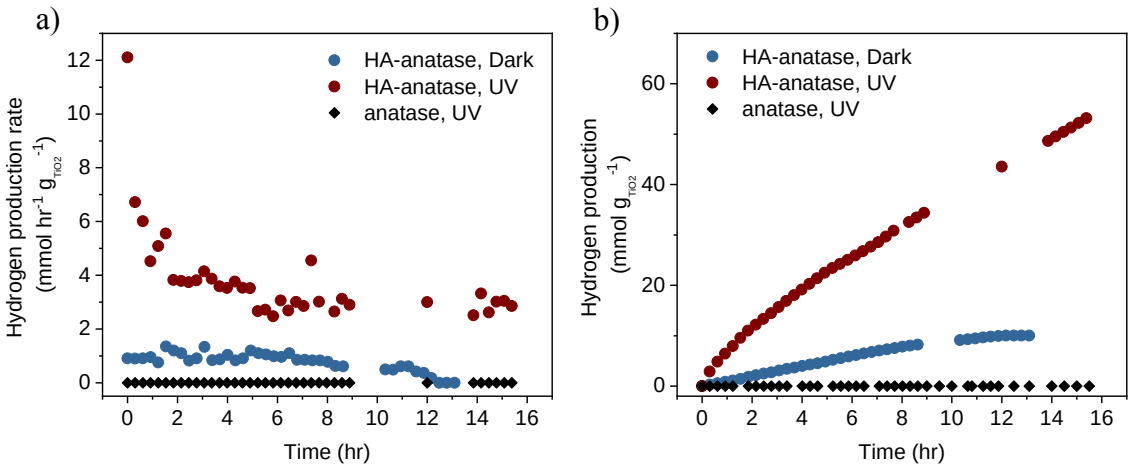

Figure 4.12 Hydrogen production from photocatalytic MSR (50 ml min^{-1} of 4 mol% CH_4, 4 mol% H_2O, balance N_2) under UV illumination (red) and dark (blue) conditions at 973 K over 25 mg of HA-anatase, and over anatase (black). Catalyst was ramped to reaction temperature under flowing N_2. a) reaction rates, b) cumulative hydrogen generation.

4.3.2.6 Proposed Reaction Mechanism

Annealing anatase in the absence of oxygen was found to effect surface structure, greatly enhancing the concentration of surface hydroxyls, and generated several types of paramagnetic defects. Together, these surface and defect sites imparted the unique ability to photocatalytically generate hydrogen from methane steam reforming to metal-free anatase particles. The concentrations of paramagnetic defects were influenced by pretreatment and reaction conditions, and only the changes in Ti^{3+} defects were consistent with the changes in hydrogen evolution rates, strongly implicating them in the catalytic

cycle. Without UV illumination, reaction was stoichiometric only (**Reaction 4.1**). A similar stoichiometric reaction was found from unstable Ti^{3+} defects generated under thermal treatment in N_2.

$$Ti^{3+} + H^+ \rightarrow Ti^{4+} + \frac{1}{2}H_2 \quad (\mathbf{4.1})$$

UV light was shown to generate Ti^{3+} centers, suggesting that photoexcitation is required to regenerate the active species (**Reactions 4.2-4.3**).

$$TiO_2 + h\nu \rightarrow h^+ + e^- \quad (\mathbf{4.2})$$

$$Ti^{4+} + e^- \rightarrow Ti^{3+} \quad (\mathbf{4.3})$$

From prior computational work, water, in the form of chemisorbed surface hydroxyls, is implicated in the methane activation mechanism.[149] With photoexcitation holes, this process generates protons and closes the catalytic cycle (**Reaction 4.4**).[150]

$$CH_4 + h^+ \rightarrow CH_3\cdot + H^+ \quad (\mathbf{4.4})$$

4.4 Conclusions

Annealing anatase TiO_2 in the absence of oxygen produced an active UV photocatalyst for hydrogen generation from methane steam reforming. The annealing process imparted metal-free hydrogen evolution activity to anatase. The latter is normally not possible without precious metal cocatalysts. Together, increased concentrations of surface hydroxyls and Ti^{3+} defects formed the active site required for hydrogen evolution. These Ti^{3+} sites possessed unusual properties, including high stability towards oxidation under air exposure and methane steam reforming reaction conditions. Ordinary Ti^{3+} sites were only capable of stoichiometric hydrogen evolution, and the unique Ti^{3+} centers from

annealing were responsible for catalytic hydrogen evolution. Without UV light, these sites were quickly consumed, as photoexcitation was essential for regenerating them.

4.A Appendix

4.A.1 Optical Property Characterization

Absolute reflectance of samples were measured via UV-Visible Spectrophotometry. The DPR method calculates the direct BGE with a much higher accuracy than the Tauc[2] method. Where in DPR analyzes the first derivative of the absolute reflectance $\frac{dR_\infty}{d\lambda}$ with respect to wavelength is fit with a Gaussian peak using a peak fitting software, Fityk. The band gap energy is the peak center, where the energy is obtained from the wavelength by multiplying Planck's constant, *h*, by the speed of light, *c*, and dividing by the wavelength, λ. The absorbance of each catalyst across the range of 200 nm to 800 nm is determined via measuring the diffuse reflectance and then converting to Kubelka-Munk units (KMU), arbitrary units analogous to absorbance for diffusely reflected samples, $F(R_\infty) = KMU = \frac{(1-R_\infty)^2}{2R_\infty}$.

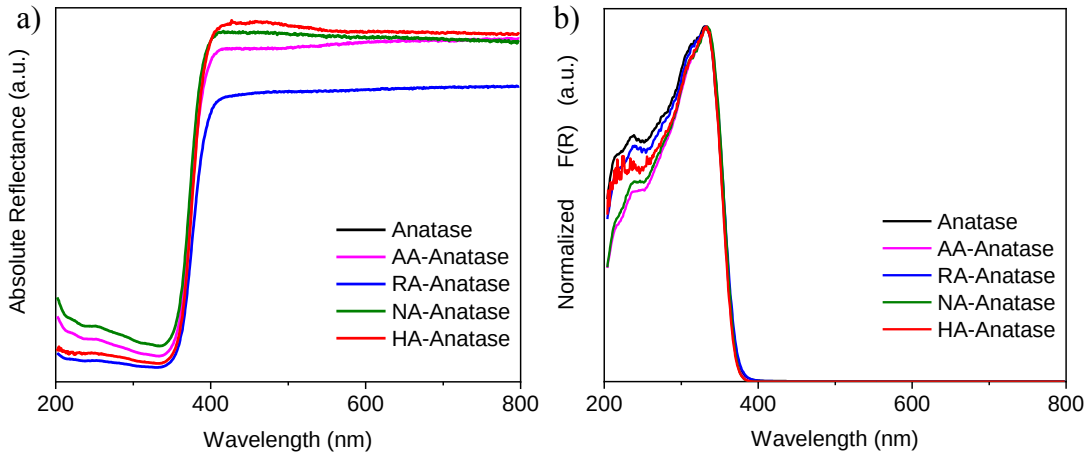

Figure 4.A1 Diffuse-reflectance UV-visible spectra of samples in a) absolute reflectance and b) Kubelka-Munk units F(R).

KMU values are normalized to the maximum value of each spectrum and plotted against wavelength. A comparison of the normalized KMU shown in **Figure 4.A1** reveals that annealed samples appear optically similar to the parent sample, with a negligible change in the onset of absorbance and a slight decrease in the normalized KMU in the UV region (200-325 nm).

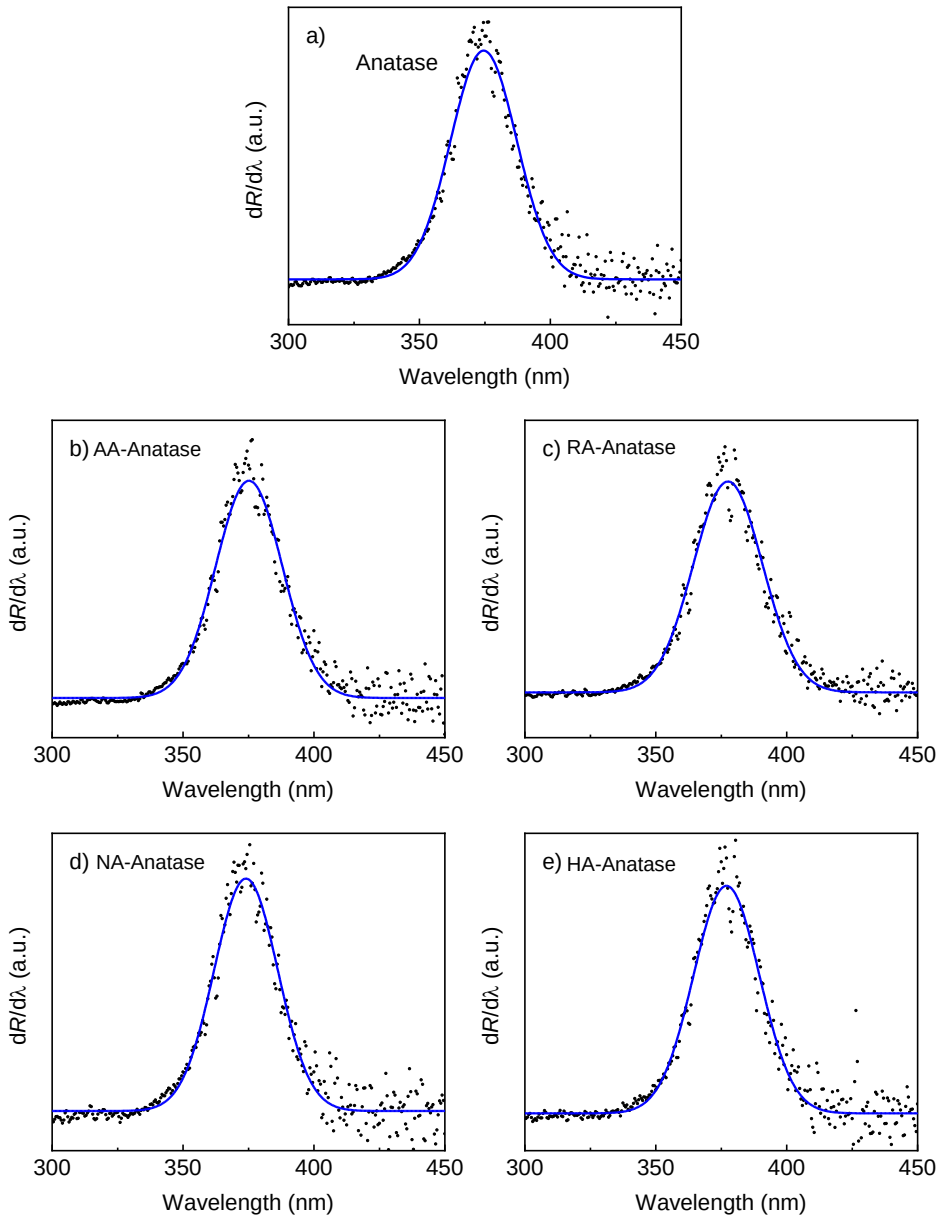

Figure 4.A2 Calculation of BGE using DPR method. Peak-center position of Gaussian curve (blue) fitted to the derivative of the reflectance spectrum (black) gives the BGE value.

The Tauc$^{1/2}$ method for determining indirect band gap energies was used where the *x*-intercept of then tangent line to the square root of [$F(R)*E(\lambda)$] gives the indirect BGE, $F(R)$ is the Kubelka Munk function and $E(\lambda)$ is the photon energy.

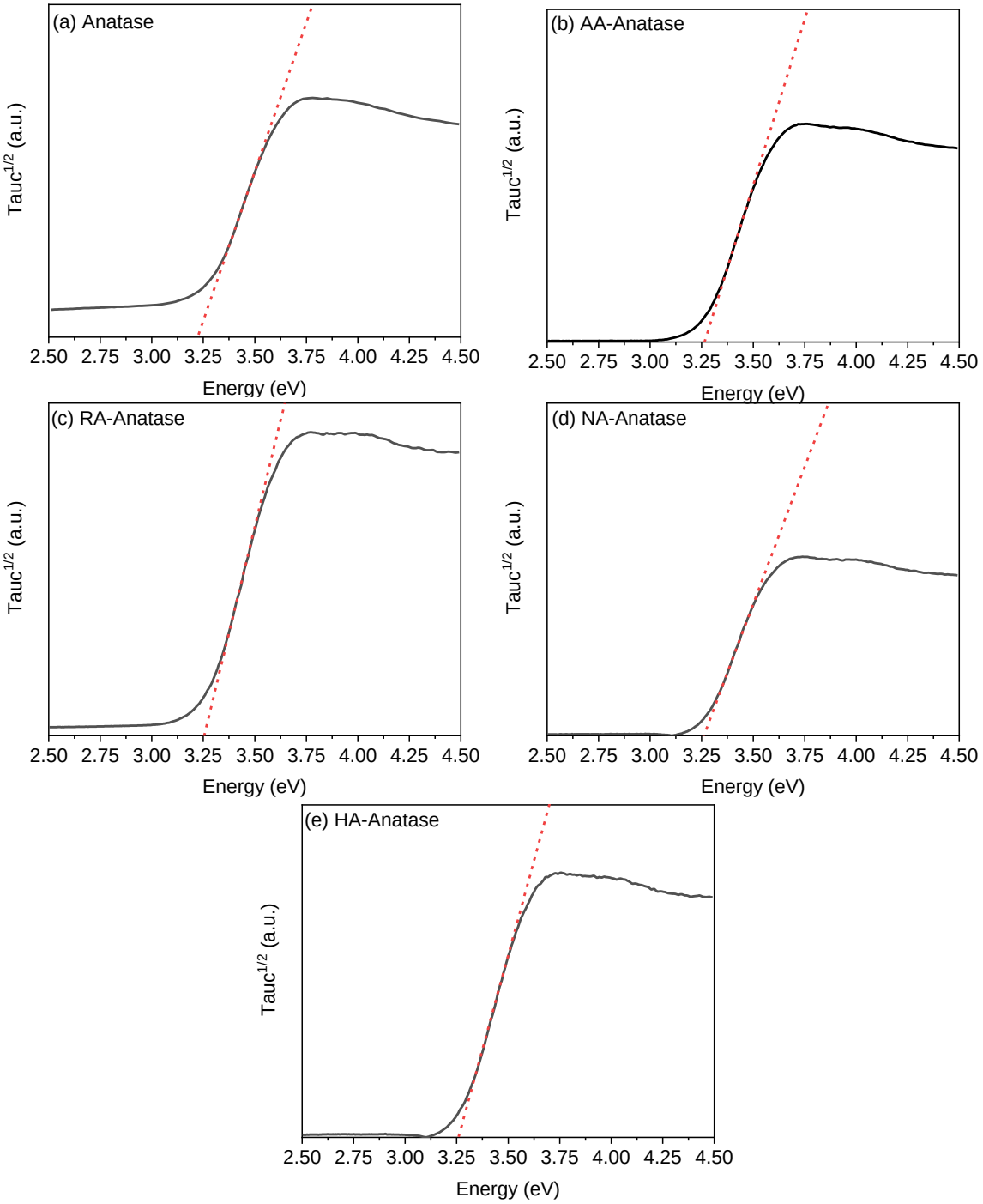

Figure 4.A3 Calculation of BGE using Tauc$^{1/2}$method. x-intercept of tangent line indicates BGE value.

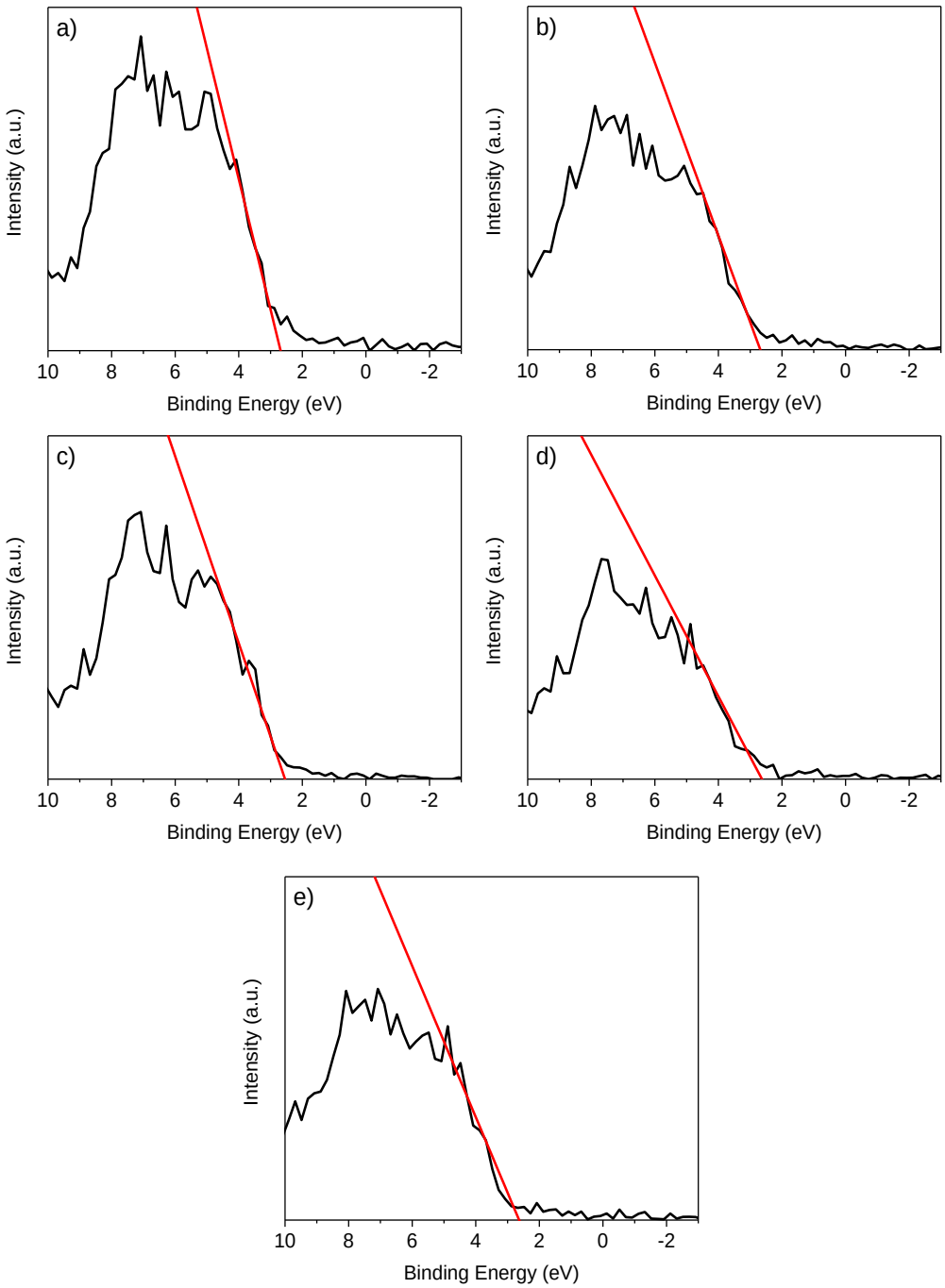

Figure 4.A4 XPS analysis of valence band position of a) anatase, b) AA-anatase, c) RA-anatase, d) NA-anatase, e) HA-anatase. x-intercept of tangent line indicates valence band energy.

4.A.2 Ti2p XPS Spectra

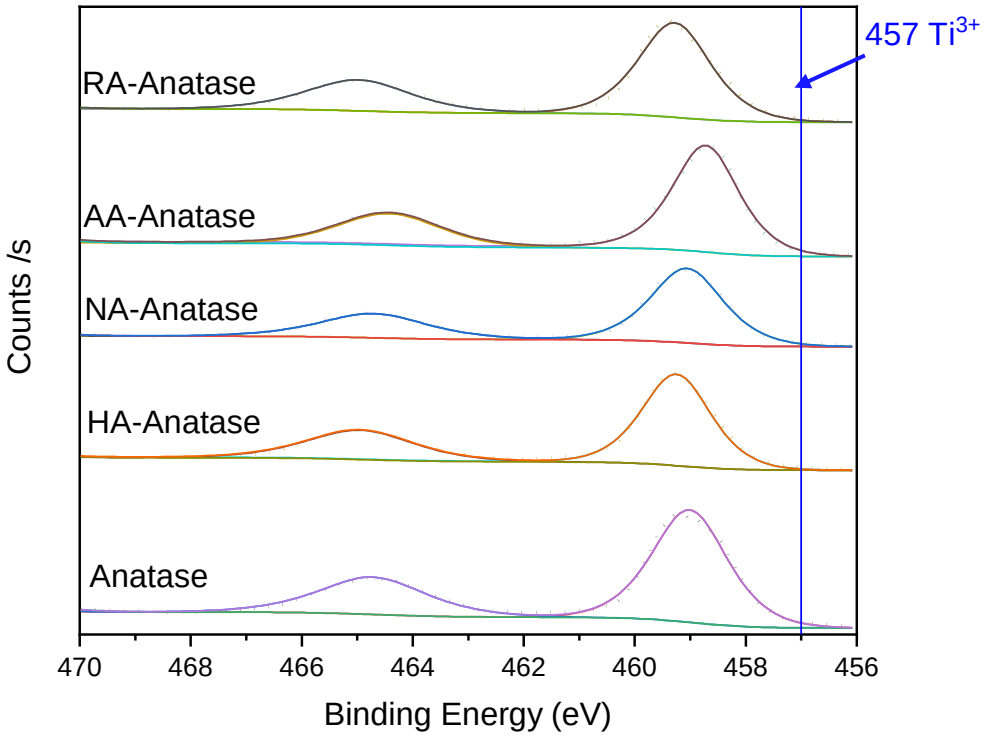

Figure 4.A5 Ti2p XPS spectra with titanium in different environments: $Ti2p_{1/2}$ (464.7 eV) and $Ti2p_{3/2}$ (464.7 eV) in Ti^{4+} state, $Ti2p_{3/2}$ in Ti^{3+} state (457.0 eV).

4.A.3 Nitrogen Analysis by XPS and CHN Elemental Analysis

Analysis of the N_{1s} region: 395 eV to 410 eV and CHN analysis indicate that there were no nitrogen atoms present in the TiO_2 lattice following annealing in nitrogen gas.

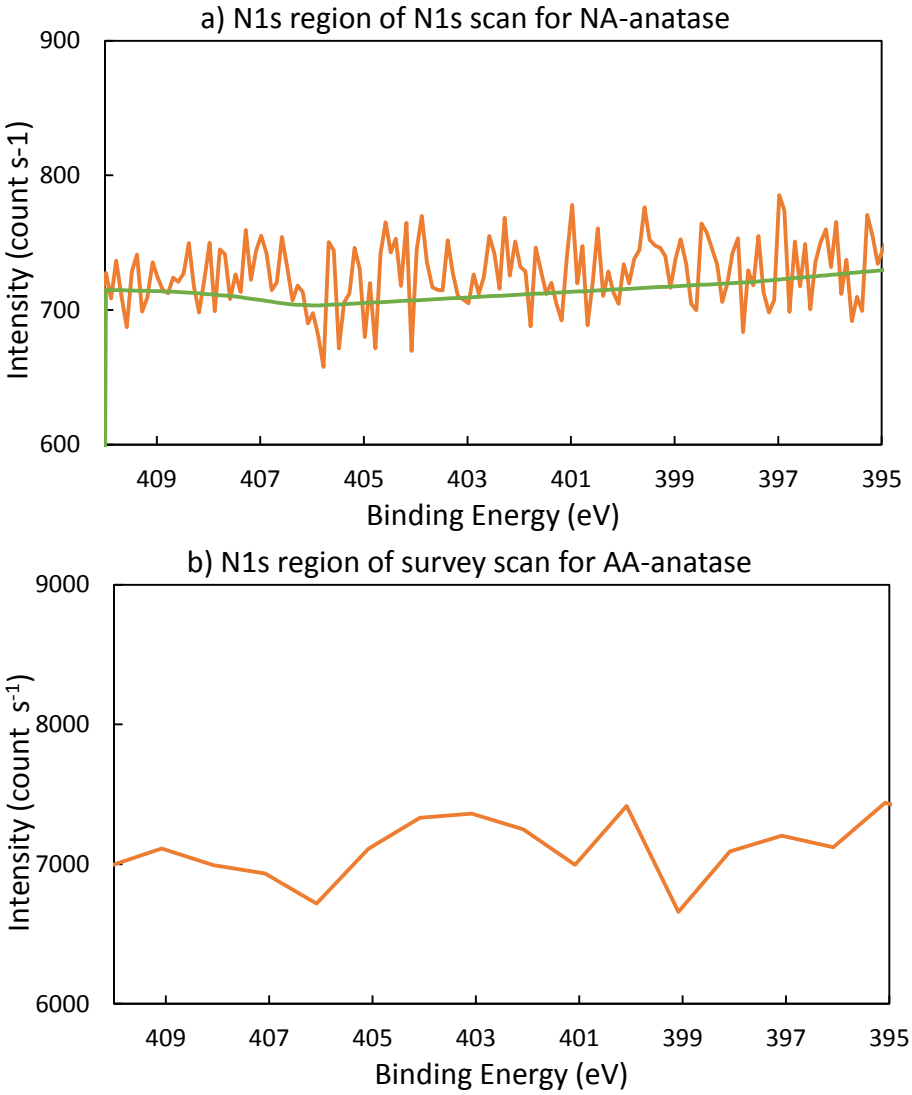

Figure 4.A6 XPS N_{1s} spectrum showing no nitrogen in either NA-anatase nor AA-anatase. a) NA-anatase, 20 scans, 3m 1.0 s 200 m, CAE 50.0 0.10eV. (b) AA-antase, 2 scans, 2 m 16.1 s 200 um, CAE 200.0, 1.0 eV.

Table 4.A1 CHN analysis (BD indicates below detection of the instrument)

Sample	%C	%H	%N
Anatase	BD	BD	BD
HA-Anatase	0.041	BD	BD
NA-Anatase	0.064	BD	BD
RA-Anatase	0.029	BD	BD

4.A.4 Phase Purity of HA-Anatase Following Reaction

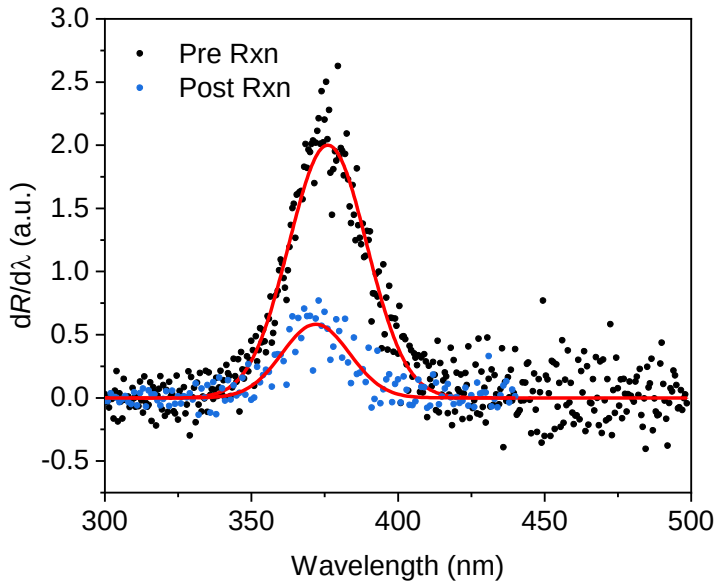

Figure 4.A7 In situ DPR of HA-Anatase before (black and after (blue) 36 hr of MSR reaction conditions. Single gaussian curve fit to data indicate a anatase phase, and no rutile phase present.

4.A.5 Illumination During EPR Spectroscopy and Photogeneration of Ti^{3+} Centers

The regeneration of Ti^{3+} centers in TiO_2 upon UV illumination is further supported via EPR analysis of samples irradiated with UV light. **Figure 4.A8** shows the difference spectra of a sample irradiated for 1 minute prior to the EPR scan as well as during the scan, under UV irradiation in the EPR sample compartment minus the original EPR spectra of the sample without illumination.

Though the spectra before and after UV illumination look similar, the difference spectra allows for the ability to detect the minute increase in Ti^{3+} centers and oxygen with a trapped hole generated via the proposed mechanism (Equation 4.1 and 4.4) upon UV illumination. Thus suggesting an increase in catalyst longevity under UV illumination compared to dark reactions.

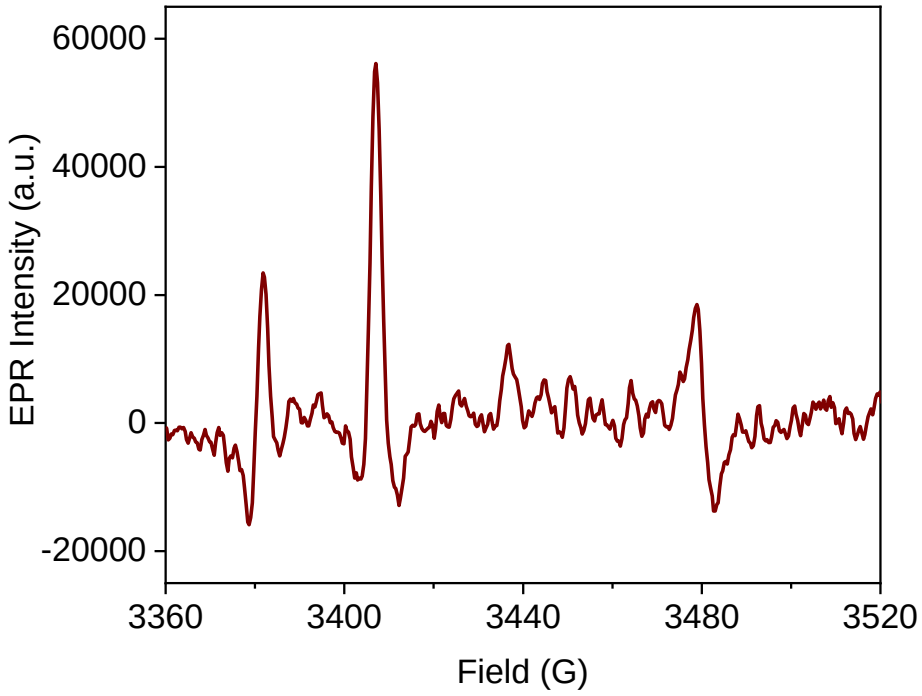

Figure 4.A8 EPR difference spectrum of HA-anatase before and after UV illumination. Illumination increased concentrations of all paramagnetic defects, F-center (g=2.003), oxygen with trapped hole (g=1.987), and bulk Ti^{3+} center ($g_{\|}$=1.97, $g_{\perp}$=1.946). While the impact on trapped holes was larger, the concentration of bulk Ti^{3+} centers also increased following illumination.

Chapter 5: Enhanced Photocatalytic Hydrogen Production over Nickel-supported Anatase

5.1 Introduction

The majority of hydrogen is produced commercially from unsustainable and unrenewable resources including the steam reforming of fossil fuel derived methane (MSR),[151,152] which is an endothermic endergonic reaction needing to be run at high temperatures. Often these reactions are run at a steam to methane ratio of 4 to avoid coking, though such large volumes of steam are improbable when considering point source MSR. Thus it is important to develop catalysts that can function at lower steam to methane ratios. This work focuses on the development of UV photo-active titania-based catalysts with supported nickel cocatalysts that use photo-derived energetic electrons to overcome the high free energy of MSR while increasing the production of hydrogen from MSR allowing for greener energy production with minimal environmental impact.

When a semiconductor is irradiated by a photon with energy greater than or equal to the semiconductor BGE an electron is excited from the valence band (VB) to the conduction band (CB) leaving behind a positively charged hole (h^+). Once an electron-hole pair is formed, the excitons may move throughout the particle and migrate to the TiO_2 surface where the oxidation/reduction reaction may occur. However, if the two excitons are in close proximity, the electron and hole may recombine leading to no net benefit from the original photoexcitation event. The rate of surface recombination therefore competes with surface reaction. One common solution to both reduce the rate of recombination and increase the rate of surface reaction is to support cocatalyst metal nanoparticles on the surface of the semiconductor. The addition of metal cocatalysts also aid in hydrogen

production from MSR as pure TiO_2 is generally inactive for hydrogen production over TiO_2.[153] Though it has been demonstrated that high pressure high temperature annealed TiO_2 is able to photocatalytically evolve hydrogen during MSR.[153] Nickel metal has been chosen as the supported metal cocatalyst on both commercial anatase and annealed anatase due to the commercial use of nickel in MSR as well as its abundance compared to other cocatalytic metals (such as platinum).

Electron Paramagnetic Resonance (EPR) has been used to investigate the presence and concentration of defects in nickel supported and annealed anatase. EPR identifies multiple paramagnetic defect structures in the annealed and nickel supported TiO_2, including paramagnetic nickel,[154] holes trapped at O atoms (O^-), electrons trapped at oxygen vacancies (F-centers), and Ti^{3+} centers in bulk and surface lattice positions, as reported in chapter 4. In this paper, the effect of illumination condition on the most promising annealed nickel on anatase photocatalysts was investigated under dark, UV illumination conditions at a steam to methane ratio of 0.8.

5.2. Materials and Methods

5.2.1 Sample Preparation

As received anatase TiO_2 (*Acros Organics,* #213581000, 98+% anatase) was calcined in a in a Thermo Scientific Lindberg Blue tube furnace equipped with multi-step ramp-soak program functionality. Samples were calcined at 773 K for 3 hours with a ramp rate of 2 K min^{-1} under a flow of 100 ml min^{-1} air. 1-wt% $Ni(O)/TiO_2$ was synthesized via incipient wetness impregnation (IWI). Nickel(II) Nitrate (*Acros Organics)* was dissolved in a known amount of DI water and added dropwise to the TiO_2 support the sample was then dried in an oven at 373 K for 24 hours and subsequently calcined under the same

conditions as the initial support. High-pressure, high-temperature annealing was carried out under 18 atm of hydrogen at 473 K for 5 days, via the methods described by the Celik group.[153] **Table 5.1** indicates the sample naming convention.

5.2.2 Diffuse Reflectance UV-Visible Spectroscopy

Diffuse reflectance UV-visible spectroscopy was carried out in a Thermo Scientific Evolution 3000 spectrophotometer equipped with a Harrick Scientific Praying Mantis diffuse reflectance accessory. A Spectralon disk was used as the absolute reflectance standard. Band gap energies were calculated using the Tauc and DPR[155] methods. Peak fitting was performed using fityk software, first mentioned in section 3.2.

5.2.3 X-Ray Powder Diffraction

X-ray powder diffraction (XRD) patterns were collected on a PANalytical Philips X'Pert X-ray diffractometer equipped with a Cu-Kα source at 40 kV and 40 mA with a 0.026° step and angular incidence 2θ between 20° and 80°. PDF# 01-073-1764 and PDF# 01-078-1510 were used to determine polymorph for anatase and rutile, respectively. Crystallite size was determined during WPF refinement while removing instrumental contribution.

5.2.4 Electron Paramagnetic Resonance

As previously discussed in chapter 4, X-band Electron Paramagnetic Resonance Spectroscopy (EPR) was performed on a Bruker Elexsys E 500 equipped with a single microwave cavity with an X-band bridge operating at 9.2-9.9 GHz with a microwave power of 40 bB. EPR spectra were recorded in 4 mm Wilmad EPR tubes at 12 K. The spin counts were calibrated using a $CuSO_4$ crystal suspended in mineral oil.

5.2.6 Photocatalytic Reactions

Gas-phase heterogeneous photocatalytic MSR reactions were carried out in a Harrick Scientific Praying Mantis high temperature reaction chamber illuminated by a Newport 150W xenon ozone-free Arc Lamp equipped with a dichroic mirror beamturner reflector and colored glass bandpass filter were used to restrict illumination to 280 nm and 400 nm. The gas-phase reaction mixture consisted of methane, nitrogen, and water vapor, supplied via nitrogen carrier gas through a DI water bubbler heated to 313 K. The catalyst was heated to the first reaction temperature of 473 K at a ramp rate of 5 K min^{-1} with constant 50 ml min^{-1} flow of reactant gases: 6 mol% methane, 5 mol% water, and balance nitrogen. 45 mg of fresh catalyst was used for each reaction. The reaction was held for 1.5 hr at each temperature between 473 K and 973 K in increments of 100 K to test photocatalytic activity at lower temperatures. An in line Agilent 7890b GC equipped with a flame ionization detector and a thermal conductivity detector was used to monitor reaction products while an Agilent 5977a GCMS equipped with a mass-selective detector was used to quantify coke formation post reaction. Hydrogen and CO_2 were the major gaseous products detected.

5.3. Results and Discussion

5.3.1 Characterization

5.3.1.1 Sample Preparation and UV-Visible Spectroscopy

The order in which the nickel was supported on the samples in relation to hydrogen annealing effected the samples absorption of visible light, as seen by a darkening of color (**Figure 5.A1**). The color change evident in the diffuse-reflectance UV-visible spectra, **Figure 5.1**, noted by an increase in visible light absorption. However this increase in visible light absorption did not yield a change in the band gap energy (BGE), **Table 5.2**. BGE

values calculated via the DPR method (**Figure 5.A2**) and the Tauc method (**Figure 5.A3**) showed minor variation in the BGE of anatase upon annealing and supporting nickel. Samples denoted in **Table 5.1**.

Table 5.1 Naming convention and order of operations for nickel supported and annealed anatase samples. Step 1 is first step. Steps follow linearly until last step for sample

Sample	Calcined	Nickel Supported	Annealed
anatase	1	--	--
Ni(O)/anatase	1,3	2	--
HA-anatase	1	--	2
HA-Ni(O)/anatase	1,3	2	4

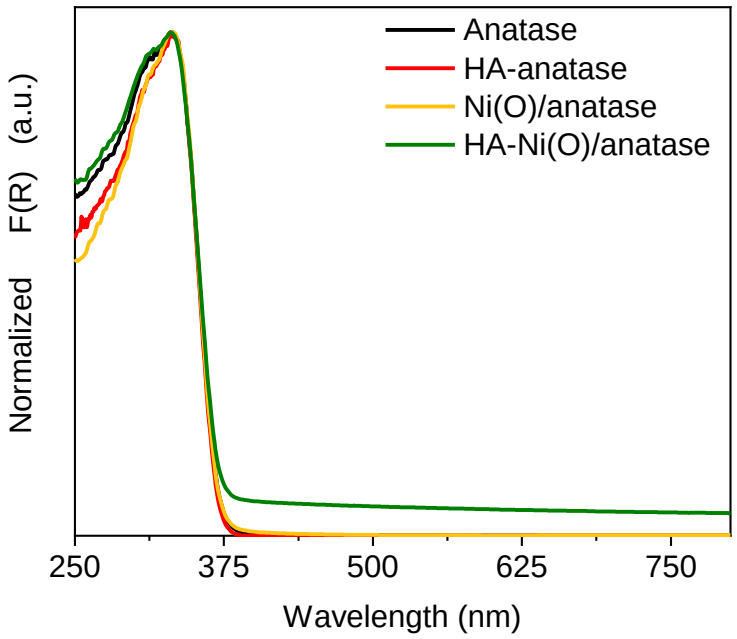

Figure 5.1 Diffuse-reflectance UV-visible spectra of samples in Kubelka-Munk units F(R) show increasing visible light absorption with nickel on anatase (Ni(O)/anatase, yellow), annealed nickel anatase (HA-Ni(O)/anatase, green) compared to anatase (black) and HA-anatase (red).

Each KMU value is normalized to the maximum value of its spectrum and plotted against wavelength. A comparison of the normalized KMU shown in **Figure 5.1** reveals that samples containing nickel metal have a greater visible light absorbance with a

negligible change in the onset of absorbance and a slight change in the normalized KMU in the UV region (200-325 nm).

Table 5.2 Physical and optical properties of nickel supported and annealed anatase samples. Particle size estimated by XRD, surface area from 11-point BET, band gap energy calculated from Tauc and DPR methods.

Sample	Tauc^{½} BGE [eV]	DPR ($dR_\infty/d\lambda$) BGE [eV]		
		Anatase	NiO	$Ni(OH)_2$
anatase	3.22	3.31	--	--
Ni(O)/anatase	3.25	3.31	3.54	3.17
HA-anatase	3.26	3.31	--	--
HA-Ni(O)/anatase	3.22	3.36	3.55	3.14

DPR is employed to reveal the presence of metal oxide polymorphs with different band gap energies. All samples were fit with a single anatase peak and no rutile was found during peak-fitting (**Figure 5.A1**).[155] While DPR was able to detect a second metal oxide with a peak centered at 3.53 eV in samples containing 1wt% nickel (**Figure 5.A1c-h**), and a third peak corresponding to nickel hydroxide centered around 3.15 eV[156] for Ni(O) samples that were not reduced and passivated. The difference between the NiO and $Ni(OH)_2$ BGE is roughly 0.38 eV which corresponds well to the difference between the two band gaps of nanostructured nickel oxide and nickel hydroxide.[157] Nickel samples that had not been reduced and passivated showed a larger intensity of the peak attributed to nickel oxide.

5.3.1.2 Electron Paramagnetic Resonance Spectroscopy

The concentration of Ti^{3+} centers was investigated via Electron Paramagnetic Resonance Spectroscopy (EPR) conducted at ambient pressure and low temperature. The EPR spectra of the parent anatase sample and all nickel supported and annealed samples are shown in **Figure 5.2**. For all spectra, five features could be identified: F-centers

(g=2.003), O^- (g=1.987), bulk Ti^{3+} ($g_{\|}$=1.97, $g_{\perp}$=1.946) and surface Ti^{3+} (g=1.89). EPR assignments agree with previous reports[138] Concentration of paramagnetic species are shown in **Table 5.2**.

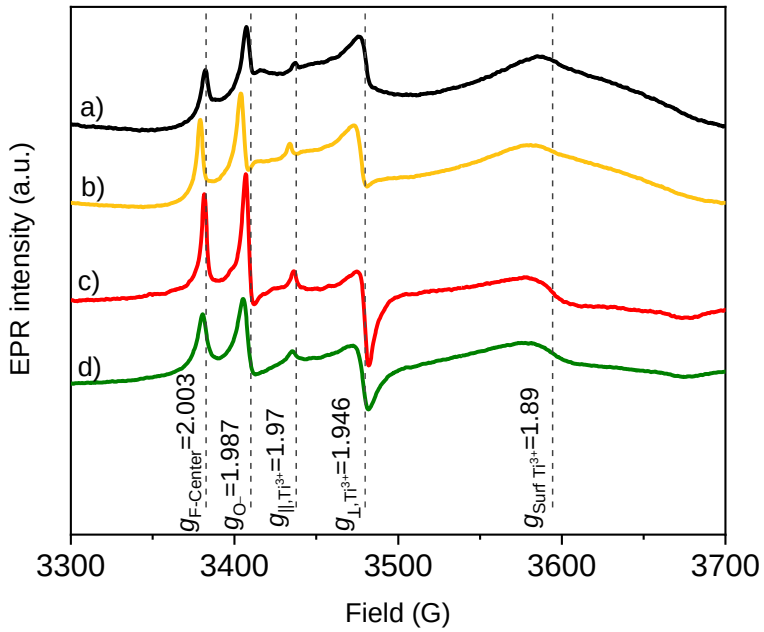

Figure 5.2 EPR spectra of *a)* anatase, *b)* Ni(O)/anatase, *c)* HA-anatase, *and d) HA-Ni(O)/anatase*. Peaks labelled for F-center (g = 2.003), oxygen with trapped hole (g = 1.987), bulk Ti^{3+} ($g_{\|}$ = 1.97, $g_{\perp}$ = 1.946), *and* surface Ti^{3+} (g = 1.89*)*.

Minimal signal for Ni was seen at g = 2.17 in HA-Ni(O)/anatase but not in Ni(O)/anatase. This signal lies in the range for various Ni species, and most closely agrees with the reported g-value for Ni^+.[154,158] The concentration of various paramagnetic species are reported in **Table 5.3**. The amount of bulk and surface Ti^{3+} appear to be reduced when nickel is supported on the TiO_2, however, nickel on the sample may be altering the signal as nickel of a sufficiently small size is expected to exhibit superparamagnetism and dominate the magnetic properties of the spectra as the particle size of nickel metal and nickel oxide decreases to the nanometer scale due to the increase in the surface to volume ratio, and therefore increase in surface spins.[154,158] Alternatively,

the presence of Ni(O) in the annealing vessel may consume some of the reducing gas, therefore decreasing the partial pressure of the annealing environment and therefore decrease the extent of Ti^{3+} centers produced, though the signal of Ni(O)/anatase and HA-Ni(O)/anatase are quite similar, which advocates for the first hypothesis.

Table 5.3 Concentration in (nmol g_{TiO2}^{-1}) of paramagnetic defects in samples measured by EPR spin counting, including bulk and surface Ti^{3+} centers, F-Centers, *and* O^- *centers*. Spin counts determined with standard reference $CuSO_4$.

Sample	**Bulk Ti^{3+}**	**Surface Ti^{3+}**	**F-Center**	**O^-**
anatase	55	1.7	0.4	1.3
Ni(O)/anatase	14	0	2.4	4.7
HA-anatase	326	13	2.1	3.8
HA-Ni(O)/anatase	17	6.2	2.7	1.8

3.2 Photocatalytic Activity

3.2.1 Photocatalyst Stability

All reported reaction rates were measured between 773 K and 973 K in increments of 100 K. The reaction was allowed to reach steady state by being held for 1 hour at every 100 K increment. Catalyst was exposed to reaction gases while ramping to reaction temperature. Under UV illumination anatase, without annealing treatment or supported nickel, shows no photocatalytic activity towards hydrogen generation, while annealed anatase (HA-anatase) showed moderate metal-free hydrogen production at 973 K.[153] The anatase polymorph of TiO_2 converts to the rutile polymorph at high temperatures. As discussed in section 3.3, during calcination, rutilization begins between 673 K and 873 K, depending on the sample.[155] XRD of select samples (**Figure 5.A4**) post reaction indicate no change in polymorph post reaction. Changes in particle shape and exposed facets of the anatase crystallites has been associated with stabilization of the anatase phase at high

temperature,[155] suggesting that both the supporting nickel as well as the annealing process stabilized the anatase phase.

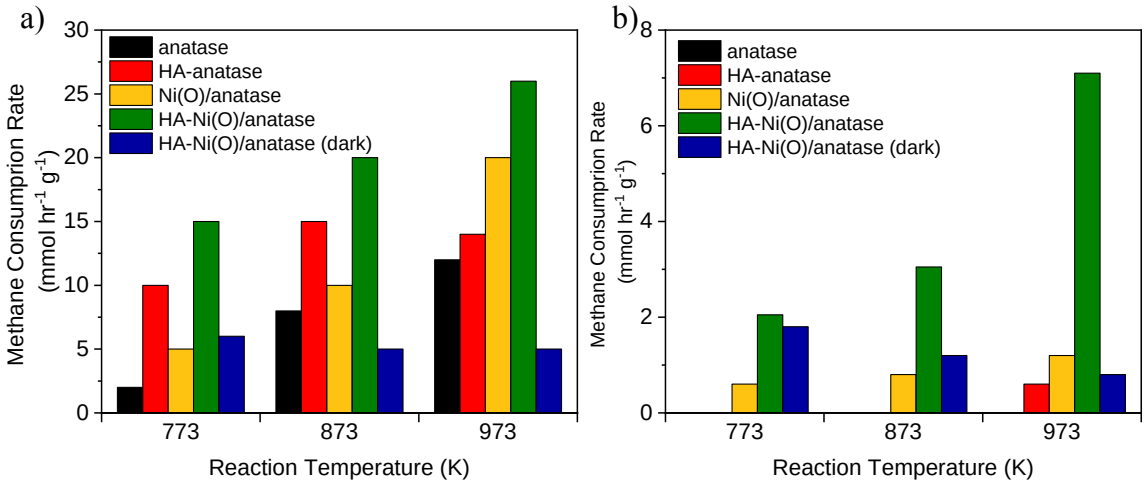

Figure 5.3 Photocatalytic MSR (50 ml min^{-1} of 5 mol% CH_4, 4 mol% H_2O, balance N_2) under UV illumination over 45 mg of sample) b) methane consumption rate, b) hydrogen production rate. Catalyst was ramped to reaction temperature under flowing reaction gases.

The addition of nickel on the TiO_2 support prior to annealing increases the methane conversion over the tested temperature range, suggesting that the supported nickel oxide aids in C-H activation. Additionally, the catalysts containing nickel are able to evolve hydrogen at lower temperatures, and at 973 K the hydrogen evolution over HA-Ni(O)/anatase is 6 time that of nickel supported on anatase and 12 times that of metal-free HA-anatase, suggesting a synergistic effect between the two main active cites for hydrogen evolution: the Ti^{3+} centers in the HA-anatase and the nickel nanoparticles. However, this also suggests that if the supported nickel had been reduced prior to reaction such that a majority of the nickel is in the metallic phase a higher activity may have been achieved.

Without illumination by UV light, there was a noticeable decline in C-H activation and hydrogen formation at increased temperature over HA-Ni(O)/anatase. This decline in activity is related to coking of the sample in the dark, as detected by the sample color

changing from gray to black. Whereas minimal coking occurred during steady state hydrogen evolution over HA-Ni(O)/anatase under UV illumination and the catalyst maintained activity and original color.

4. Conclusions

The combination of a nickel cocatalyst with a high concentration of unique Ti^{3+} defect sites generated during annealing catalyze hydrogen evolution from MSR, precious metal cocatalysts are avoided. This work shows that the implementation of nickel supported on defect-rich anatase TiO_2 for highly stable photocatalytic hydrogen evolution from MSR with a major reduction in coking at low steam to carbon ratios due to the regeneration of the Ti^{3+} upon illumination preventing coke accumulation on the nickel cocatalyst under UV irradiation.

5.4. Appendix

5.A1 Band Gap Measurements

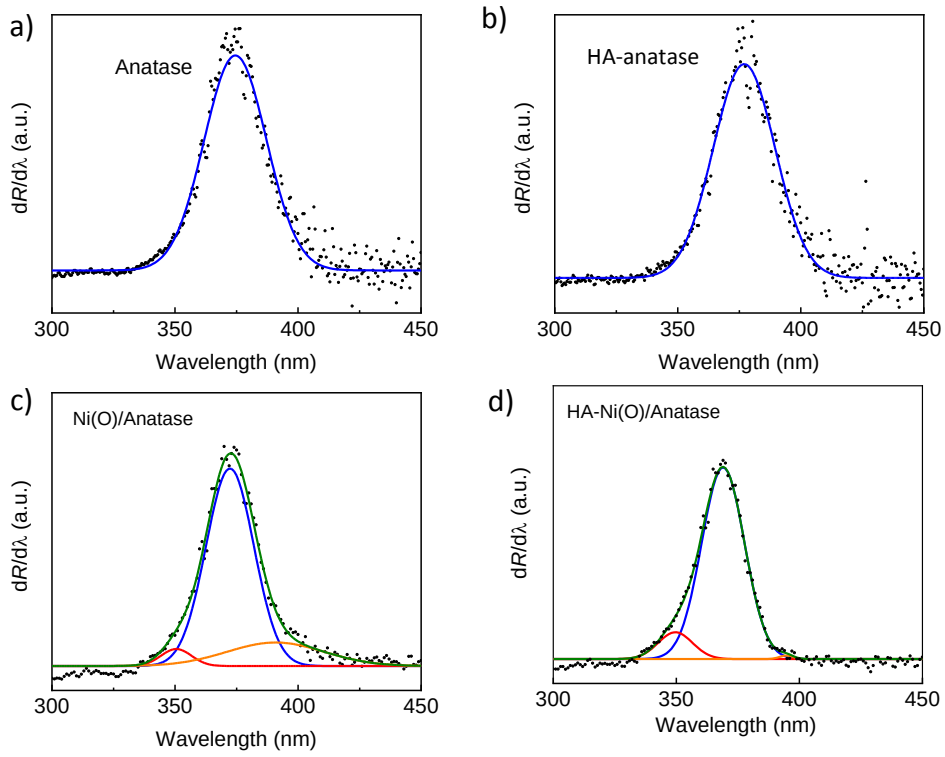

Figure 5.A1 Calculation of BGE using DPR method. Peak-center position of Gaussian curve for anatase TiO_2 (blue), nickel oxide (red), and nickel hydroxide (orange) fitted to the derivative of the reflectance spectrum (black) for a) anatase, b) HA-anatase, c) Ni(O)/anatase, d) HA-Ni(O)/anatase.

The Tauc[1/2] method for determining indirect band gap energies was used where the *x*-intercept of then tangent line to the square root of $[F(R)*E(\lambda)]$ gives the indirect BGE, $F(R)$ is the Kubelka Munk function and $E(\lambda)$ is the photon energy.

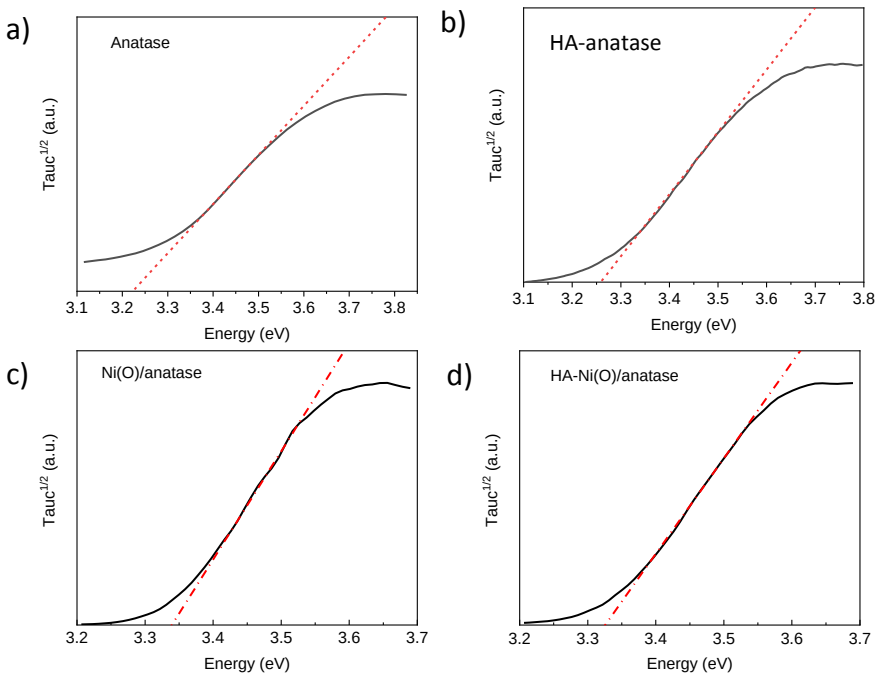

Figure 5.A2 Calculation of BGE using Tauc$^{1/2}$method. x-intercept of tangent line indicates BGE value for a) anatase, b) HA-anatase, c) Ni(O)/anatase, d) HA-Ni(O)/anatase.

5.A2 Phase Purity of HA-Anatase Following Reaction

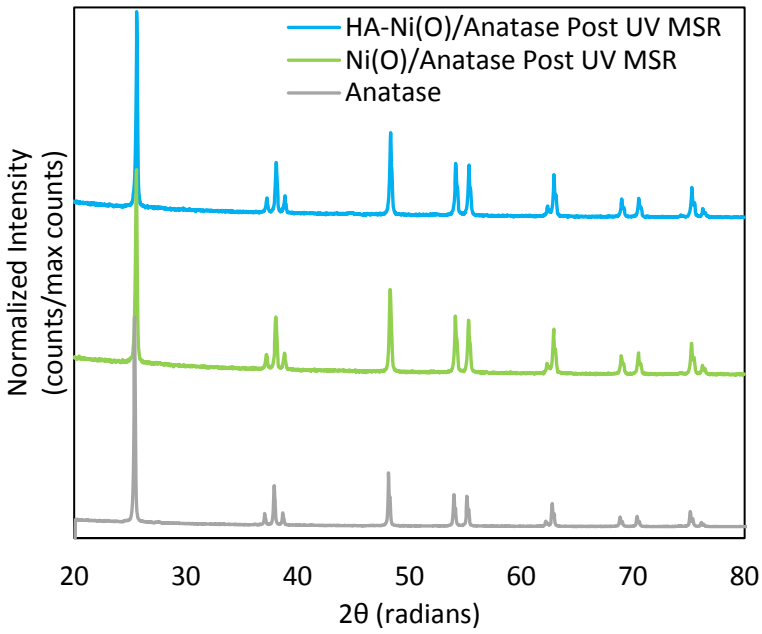

Figure 5.A3 XRD of post UV MSR samples: HA-Ni(O)/Anatase (blue), and Ni(O)/Anatase (green) compared to as received anatase (gray), indicating anatase phase, and no rutile phase present post reaction at 973 K.

The X-ray powder diffraction patterns of the nickel supported and annealed samples compared to the parent anatase material show that the anatase polymorph is maintained, **Figure 5.A3**. As the nickel loading is below the limit of XRD no metallic nickel nanoparticles or nickel oxide nanoparticles are noted in the XRD patterns.

Chapter 6: Properties and Photocatalytic Application of Low Pressure Flame Synthesized Anatase TiO_2

6.1 Introduction

Titanium dioxide (TiO_2) is an effective photocatalyst; stable under reaction conditions and photoactive in the ultraviolet spectrum. The anatase phase of TiO_2 is especially favored for photocatalytic applications due to the high mobility of excitons.[159] The two most commonly occurring phases of TiO_2 are rutile, and anatase, with anatase being the phase of interest in this study due to its high surface area and increased exciton transport: charge carriers excited in the bulk are able to reach the surface to effect surface reaction, with maximum thickness of 2.5 nm and 5 nm for rutile and anatase particles respectively, as discussed in chapter 1.

Flame synthesis is well-known as a technique that can control physical and chemical properties of particles. It has received attention due to its scalability, low cost, high throughput capabilities[160] as well as its ability to control various parameters such as particle size, crystallinity, and phase purity.[161] The implementation of low pressure flame synthesis using premixed flames has been investigated for the synthesis of TiO_2,[162] SiO_2,[163] among others. Employing a burner-stabilized premixed stagnation flat flame (SFF)[161,164] at 20 torr small nanoparticles (~7nm) of carbon doped TiO_2 are produced from TTiP. The small particle size allows for a more efficient use of the excitons from within the bulk. Carbon doping of TiO_2 via various methods has been an area of interest over the last decade.[165] Both experimental and computational work has analyzed the feasibility and activity of nonmetal doped TiO_2.[166,167]

6.2 Materials and Methods

6.2.1 Sample Preparation

Low pressure flame synthesis was conducted in the synthesis apparatus used in previous work by the Tse group.[162] The liquid precursor, titanium tetra-iso-propoxide (TTiP), is entrained in the hydrogen carrier gas via a bubbler heated to 358 K. The seeded carrier gas is then combined with the nitrogen, and oxygen to form an axi-symmetric, stagnation-point mixed flame with a composition of 1:1.21:0.74 H_2:O_2:N_2 with a linear flow through the burner of 250 cm s^{-1} for a precursor loading rate of 3.87E-2 mol s^{-1}. All manifold lines are heated to 383 K. TiO_2 nanoparticles are collected from the substrate collection plate cooled to 277 K. The walls of the combustion chamber were continuously cooled to maintain a temperature of 277 K.

6.2.2 Surface Area Analysis

Multi-point BET surface area and pore analysis were conducted by nitrogen physisorption at 77 K with a Quantachrome Autosorb1. Pore diameter and volume were measured via NLDFT equilibrium physisorption at 77 K with nitrogen as the adsorbent and silica as the oxygen model.

6.2.3 X-Ray Powder Diffraction

X-ray powder diffraction (XRD) patterns were collected on a PANalytical Philips X'Pert X-ray diffractometer equipped with a Cu-Kα source at 40 kV and 40 mA with a 0.026° step and angular incidence 2θ between 20° and 80°. PDF# 01-073-1764 and PDF# 01-078-1510 were used to determine polymorph for anatase and rutile, respectively. Crystallite size was determined during WPF refinement while removing instrumental contribution.

6.2.3 CHN Elemental Analysis

Carbon-Hydrogen-Nitrogen (CHN) Elemental analysis was conducted on a Carlo Erba NA-1500 Analyzer, as mentioned in section 4.2. Samples were massed in small aluminum cups and combusted at 1773 K to yield quantification of Carbon with high accuracy, ±0.003 wt%.

6.2.4 Diffuse Reflectance UV-Visible Spectroscopy

Diffuse Reflectance UV-Visible Spectroscopy was measured using a Harrick Scientific Praying Mantis Diffuse Reflectance Accessory mounted in a Thermo Fisher Evolution 300 UV Visible Spectrophotometer. Band Gap energies were obtained from the Tauc method and the DPR methods, as mentioned in section 3.2.

6.2.4 Electron Paramagnetic Resonance

X-band Electron Paramagnetic Resonance Spectroscopy (EPR) was performed on a Bruker Elexsys E 500 equipped with a single microwave cavity with an X-band bridge operating at 9.2-9.9 GHz with a microwave power of 40 bB, section 4.2. EPR spectra were recorded at 12 K. The spin counts were calibrated using a $CuSO_4$ crystal suspended in mineral oil.

6.2.5 X-Ray Photoelectron Spectroscopy

X-Ray Photoelectron Spectroscopy (XPS) was measured under UHV using a Thermo Fisher K-Alpha XPS instrument equipped with a monochromatic Al Kα line with photon energy of 1486.7 eV. As discussed in chapter 4, the estimated analysis depth in this geometry is about 10 nm. Spectra were deconvoluted using the method described by Nesbitt and Banerjee to obtain a quantifiable near-surface titanium oxidation state and

carbon and oxygen environment. All reported binding energies are in reference to the C1s peak at 285.0 eV.

6.2.6 Electron Microscopy

Annular Dark Field imaging using an aberration-corrected-STEM was performed with a Nion UltraSTEM using a ~1 Å probe at 60 kV. Annular Dark Field imaging using a Jeol 2010F TEM at 200 kV. Scanning Electron Micrographs were obtained from a Nanoscience Instruments Phenom ProX SEM operating at 10 kV whereas EDS scans were run at 15 keV for maximum sensitivity.

6.2.7 Photocatalytic Water Reduction

Photocatalytic activity of the samples was tested via batch phase water reduction with methanol as a sacrificial agent.[168] The reaction was carried out in a 25 ml glass reactor at 293 K. 3 mg of fresh catalyst was dispersed in 10 ml of 20% methanol in DI water via sonication. The sample was illuminated with a Newport 150W Xenon Ozone-free Arc Lamp under UV illumination. UV cutoffs of 280 nm – 400 nm were achieved via dichroic mirror beamturner assembly and glass bandpass filter. A 300 µL aliquot of the reactor headspace gas was injected into the thermal conductivity detector of an Agilent 7890B GC to monitor the hydrogen production rate.

6.3 Results and Discussion

6.3.1 Characterization

6.3.1.1 Sample Polymorph Analysis

All characterizations and analyses were compared to commercial anatase TiO_2 (*Acros Organics*, #213581000). The low pressure flame synthesized samples were determined by XRD to be anatase phase with a crystallite size of 7 nm, **Figure 6.1**. Upon

calcination under 100 ml min^{-1} air to 673 K the crystallinity is maintained while the crystallite size increased slightly to 8 nm.

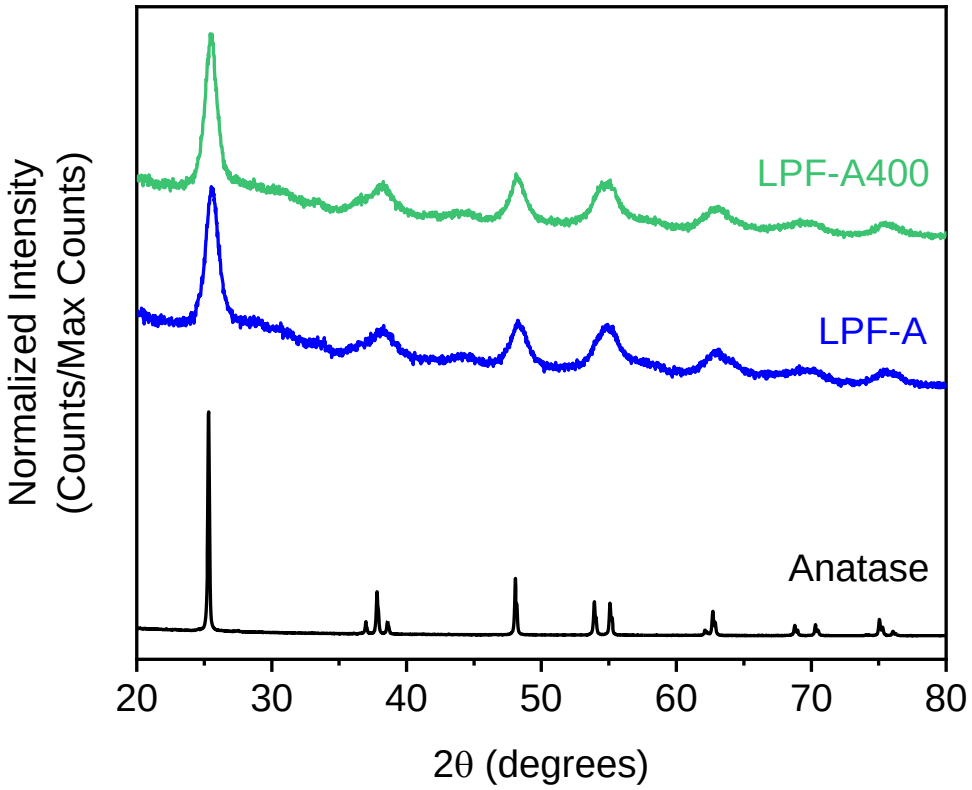

Figure 6.1 XRD powder diffraction patterns of analyzed samples: Anatase (black), LPF-A (blue), and LPF-A400 (green).

6.3.1.1 Surface Area and Porosimetry Analysis

Surface area of the as synthesized anatase TiO_2 was 22 times larger (187 m^2 g^{-1}) than commercial anatase (8.54 m^2 g^{-1}) and 2.6 times larger than commercial P25 (71.2 m^2 g^{-1}), **Table 6.1**. Upon calcination particle size increases while surface area decreases to a value of 177 m^2 g^{-1} and 149 m^2 g^{-1} for LPF-A calcined to 673 K and 773 K, respectively. The isotherms (**Figure 6.A2**) for flame synthesized samples show a hysteresis indicating porosity.

Table 6.1 Physical and optical properties of low pressure flame synthesized anatase samples. Sample preparation, particle size estimated by XRD, surface area from 7-point BET, mean pore volume and mode pore width determined by NLDFT equilibrium mode physisorption analysis, and band gap energy calculated from Tauc and DPR methods.

Sample	Calcined	Particle size[a] (nm)	Surface Area[b] (m^2 g^{-1})	Mean Pore Volume (cc g^{-1})	Avg. Pore Width (nm)	Tauc$^{1/2}$ BGE (eV)	DPR BGE (eV)
Anatase	-	26.5	8.5	0.042	NA	3.22	3.31
P25	-	31.0	71.2	0.258	27.7	3.27	3.33, 3.13[c]
LPF-A	-	7.2	187	0.503	12.8	3.37	3.27, 3.18[d]
LPF-A400	673 K	8.0	177	0.627	27.1	3.23	3.27, 3.18[d]
LPF-A500	773 K	8.5	149	0.918	54.1	3.23	3.25, 3.12[d]

[a)] Apparent crystallite size from whole pattern fitting Rietveld refinement
[b)] C-values for BET of samples: anatase: 149.9, P25: 71.5, LPF-A: 123.6, LPF-A400: 112.2, LPF-A500: 104.2.
[c)] BGE of rutile TiO_2
[d)] BGE of semiconductor effected by carbon doping of sample, as no rutile is seen in the sample via XRD.

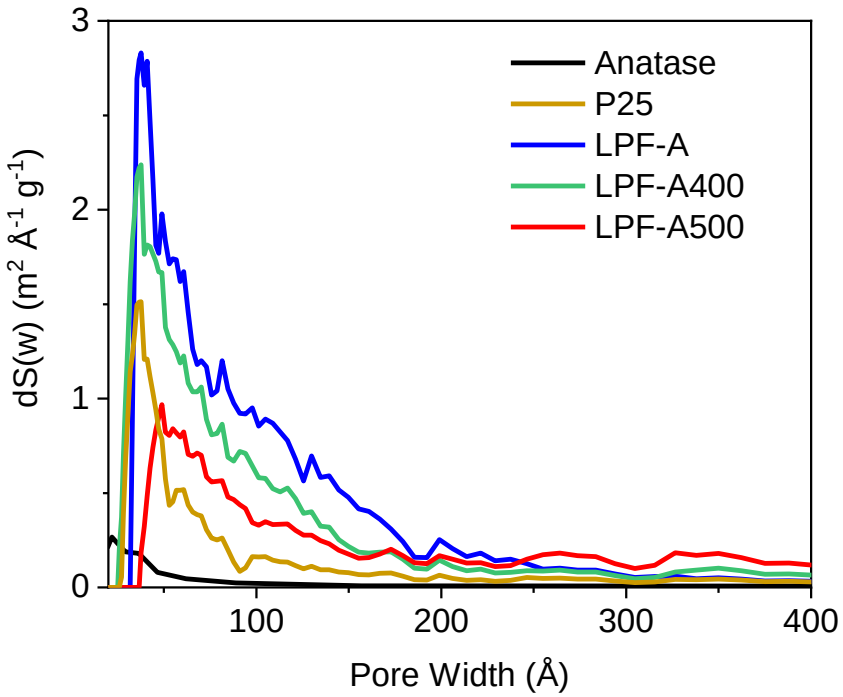

Figure 6.2 Pore size distribution for commercial anatase (black), P25 (yellow), LPF-A (blue), LPF-A400 (green), and LPF-A500 (red).

As the sample is calcined the pore width and mean pore volume increases, **Table 6.1**. High surface area, small particle size, and mesoporosity (**Figure 6.2**) may all aid in photocatalytic efficiency of the flame synthesized sample. STEM (**Figure 6.3**) reveals that the as synthesized particles are not mesoporous, but that the mesoporosity is a result of the space between the intimate contact between primary particles that are fused during synthesis in the flame regime as well as quenching on the substrate plate.

6.3.1.5 Microscopy

TEM (**Figure S4**) and STEM (**Figure 6.3**) were employed to confirm particle size as well as investigate particle crystallinity and mesoporosity.

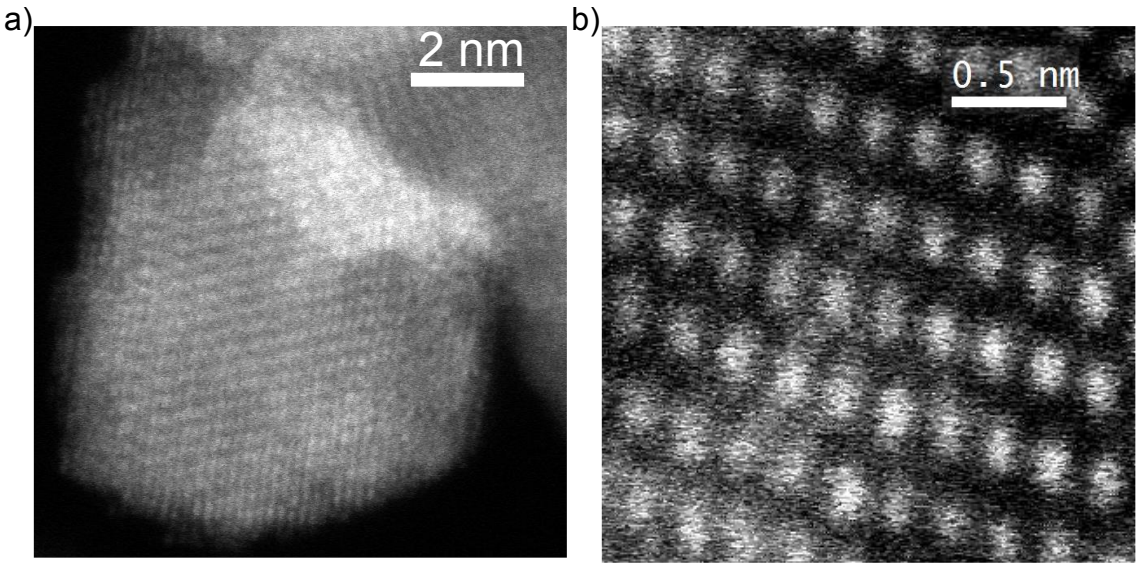

Figure 6.3 High Resolution STEM Image of low pressure flame synthesized carbon doped anatase (LPF-A) a) single particle over vacuum space with 2 nm scale, and b) increased resolution of particle lattice fringes with 0.5 nm scale.

Since the TiO_2 precursor contains carbon, CHN analysis was used to determine carbon content. The as synthesized particle is 1.15 % carbon by mass, **Table 6.A1**. The as synthesized particles are crystalline throughout and not a carbon-titania core shell structure, as seen by the lattice fringes from center to edge of the nanoparticle (**Figure 6.3** and **Figure**

6.A4). STEM shows evidence for interstitial carbon doping; roughly 15% of the lattice spacing have a 0.04 nm increase in distance from Ti center to Ti center with an average distance of 0.289 nm (SI), which may be preferential for heterogeneous photocatalysis over TiO_2.

Analysis of micrographs from Jeol 2010F Transmission Electron Microscope of LPF-A confirmed an average particle size of 7.2 nm, **Figure 6.4**. During synthesis the primary particles fuse during quenching on the substrate plate. This process creates a network of primary particles with void space (pores), as seen in Figure 6.4. The average and mode diameters of the pores seen in the TEM micrographs are in agreement with the values determined via porosimetry where the average pore width is about 12-15 nm.

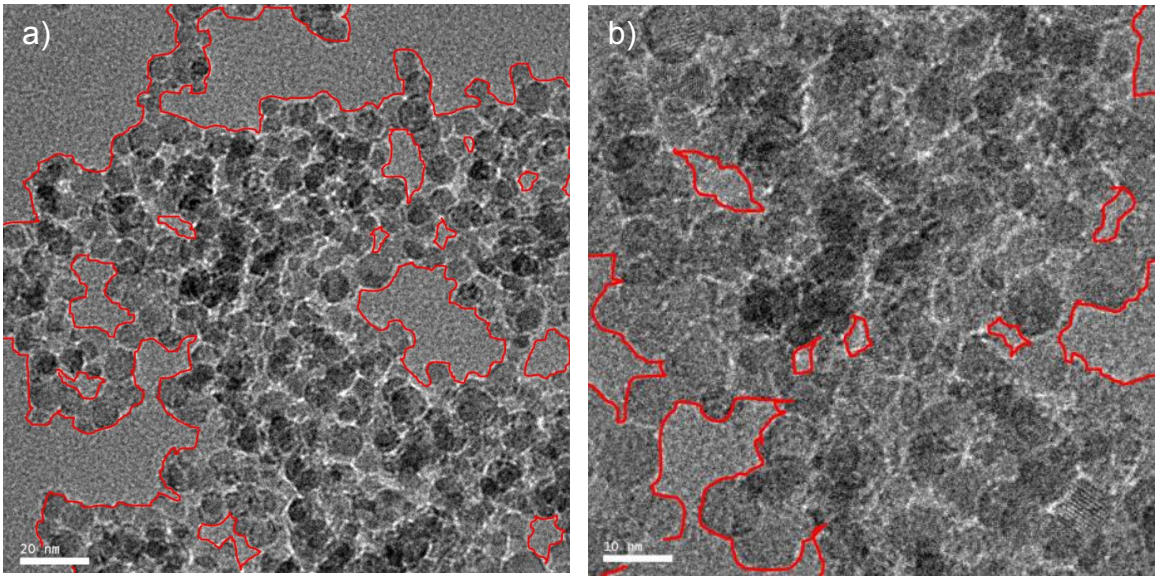

Figure 6.4 TEM micrographs of LPF-A depicting a network of TiO_2 primary particles and the pores/void space within the network. The interface between the primary particles and the void space is marked in red with a scale of a) 20 nm and b) 10 nm.

6.3.1.3 X-ray Photoelectron Spectroscopy

The chemical environments of surface and near-surface oxygen, carbon, and titanium atoms in as synthesized LPF-A were analyzed by XPS. The O1s signal of oxygen

atoms in surface environments were fit with three peaks, as shown in **Figure 6.5a**. The primary peak at a binding energy of 530.4 eV corresponds to the bulk/lattice oxygen in TiO_2. The secondary peak at 531.9 eV is assigned to defect oxygen sites corresponding to an oxygen atom geminal to a lattice oxygen vacancy (V_o), and the tertiary peak at 532.9 eV is assigned to oxygen in a surface hydroxyl state is seen only in commercial anatase. Evidence of Ti^{3+} centers are seen as shoulders at 461.2 and 457 eV (**Figure 6.5b**) for Titanium $2p_{1/2}$ and $2p_{3/2}$, respectively. Titanium and oxygen band assignments per the discussion in section 4.3. Additionally, analysis of the carbon environment confirms the carbon environment with peaks at 285.0 eV (C-C or C-H), 286.7 eV (C-O), and 289.1 eV (C=O), **Figure 6.5c**. No evidence of the Ti-C bond is seen at 281.1 eV indicating that the carbon is not directly bonded to the Titanium, but either bonded to an oxygen, or interstitially doped.

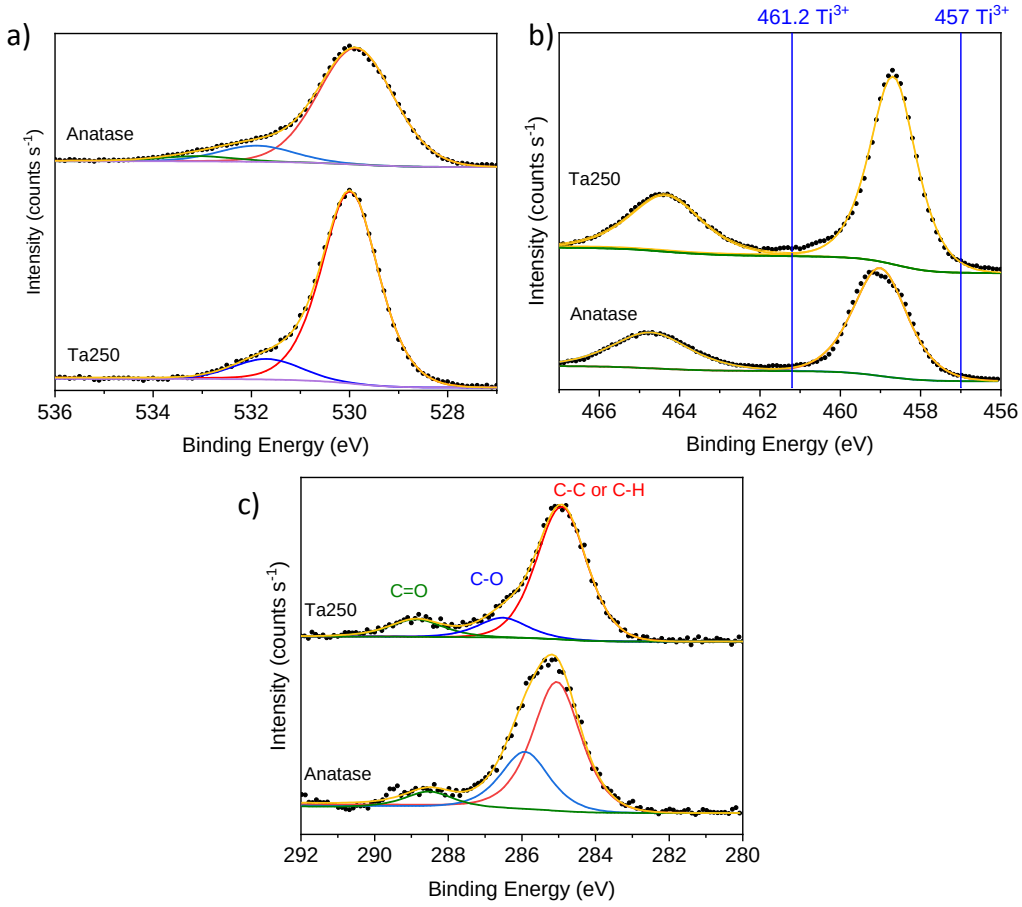

Figure 6.5 XPS spectra of as synthesized low pressure flame synthesized anatase vs commercial anatase a) O1s region showing oxygen in two environments in the flame synthesized sample and three in the commercial anatase, deconvoluted to fit up to three peaks to bulk oxygen (red), oxygen defect sites adjacent to oxygen vacancies (blue), and surface hydroxyl (green). b) Ti2p region showing titanium in different environments: $Ti2p_{1/2}$ (464.7 eV) and $Ti2p_{3/2}$ (464.7 eV) in Ti^{4+} state, $Ti2p_{1/2}$ in Ti^{3+} state (461.2 eV), and $Ti2p_{3/2}$ in Ti^{3+} state (457.0 eV). c) C1s spectra showing carbon in three environments, the C-C or C-H (285.0 eV), C-O (286.7 eV), and C=O (289.1 eV).

6.3.1.4 Electron Paramagnetic Resonance Spectroscopy

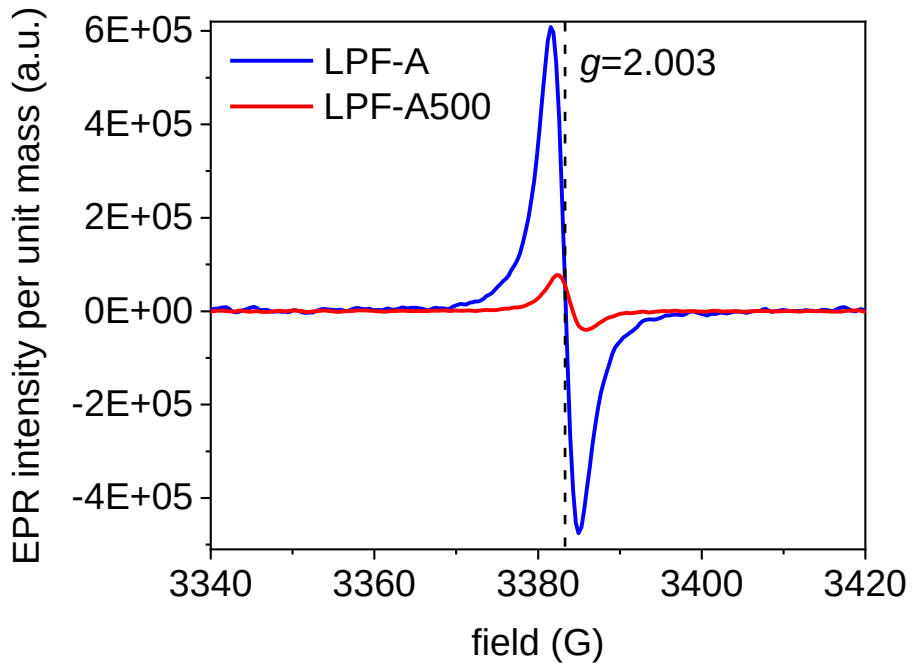

Figure 6.6 EPR spectra of as synthesized LPF-A (blue) and LPF-A500 (red). Labelled g-factor for either F-center (g = 2.003) or isopropoxide radical (g = 2.002).

The EPR spectra of LPF-A and LPF-A500 shows a strong singlet at *g*-factor = 2.003, corresponding to either F-center (g = 2.003) or isopropoxide radical (g = 2.002),[169,170] **Figure 6.6**. Upon calcination the intensity of the signal decreased, suggesting that the F-center was stabilized by a carbon atom or that the isopropoxide radical was removed during the calcination. The double integration of the EPR signal at a *g*-factor of 2.003 quantifies 21.0 µmol/mol TiO_2 and 3.5 µmol/mol TiO_2 for LPF-A and LPF-A500, respectively. An 83% decrease in signal agrees with a 94% decrease in carbon from CHN analysis, **Table 6.A1**, though the 10% difference in carbon loss suggests that at least some of the signal at *g*=2.003 comes from f-centers instead of carbon containing radicals. Due to saturation from the signal at *g*=2.003 minimal contribution from Ti^{3+} was seen via EPR.

6.3.2 Photocatalytic Water Reduction

As the particle size decreases the photocatalytic activity is enhanced due to the increasing percentage of atoms on the surface which provide locations for the surface redox reactions to occur. However, per the discussion in chapter 1, as particle size shrinks below 10 nm the confining dimension of the discrete energy orbitals shrinks. Due to this, region of irradiated sunlight that the catalyst can absorb will shrink due to the widening of the band gap of a bulk material until it reaches the energy difference between the HOMO and LUMO orbitals of a molecule.[171] Therefore there is a tradeoff between decreasing the particle size as it can increase surface area and efficiency of bulk exciton transport, however decreases BGE. This is rested via water reduction with methanol as a sacrificial agent.

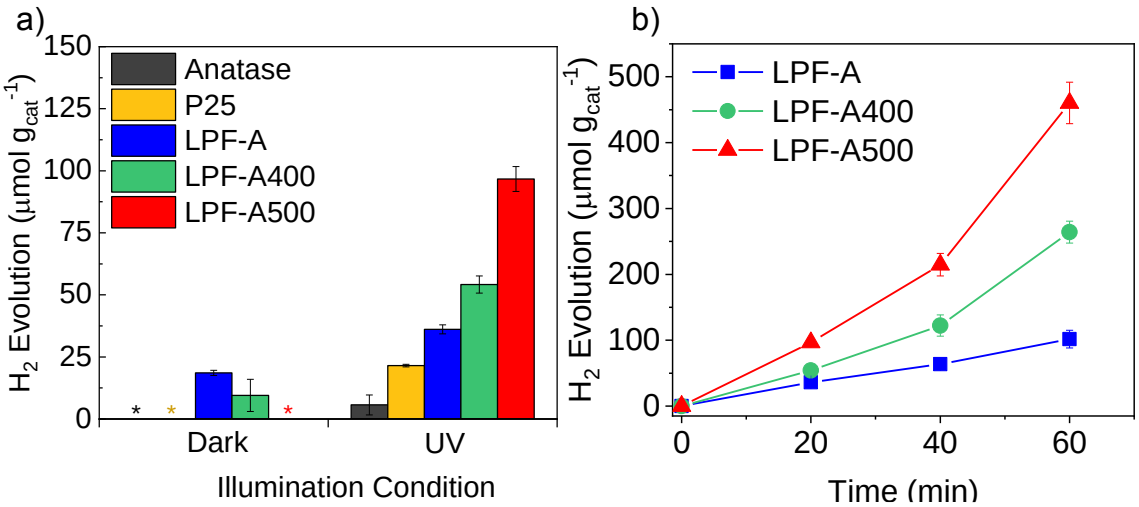

Figure 6.7 Hydrogen generation from water reduction under no illumination and UV illumination (280 nm – 400 nm), reaction vessel at room temperature. a) All samples at 20 minutes, b) hydrogen generation over an hour for LPF-A, LPF-A400, and LPF-A500. * indicates no hydrogen production for that reaction condition.

Under ambient temperature and pressure neither commercial anatase nor commercial Degussa P25 have any thermocatalytic (dark) activity for hydrogen

production, while they show minimal activity (10 – 22 $\mu mol_{H2}\ g_{TiO2}^{-1}$) under UV illumination for 20 minutes, **Figure 6.7**. In contrast the as synthesized low pressure flame synthesized TiO_2 shows activity in the dark (18 $\mu mol_{H2}\ g_{TiO2}^{-1}$) as well as increased activity under UV illumination (36 $\mu mol_{H2}\ g_{TiO2}^{-1}$). Upon calcination the sample begins to lose dark activity suggesting that carbon content plays a role in ambient temperature thermocatalytic hydrogen production. Conversely, calcination of the particles increases the photocatalytic hydrogen production to 54 $\mu mol_{H2}\ g_{TiO2}^{-1}$ and 97 $\mu mol_{H2}\ g_{TiO2}^{-1}$, over LPF-A400 and LPF-A500, respectively. The increase in hydrogen production over the catalyst post calcination suggests that a combination of minimal carbon content (0.068 wt%), and larger pore diameter and volume enhance the

6.4 Conclusions

High surface area, carbon doped anatase phase TiO_2 with mesoporosity is synthesized with low pressure flame synthesis employing a burner-stabilized premixed stagnation flat flame. These particles (7-8.5 nm) are below the quantum confinement limit, yet show unique photocatalytic activity. The photocatalytic activities of the LPF-A systems were evaluated following hydrogen evolution from water reduction under dark and UV irradiation. As hypothesized, the low pressure flame synthesized samples showed enhanced the photocatalytic activity. Calcining LPF-A decreases doped carbon content while increasing pore diameter and pore volume, leading to an increase in photocatalytic activity.

6.A Appendix

6.A.1 Diffuse Reflectance UV-Visible Spectroscopy

In situ UV-visible spectroscopy in tandem with calcination under 100 ml min^{-1} allowed for a visual characterization of the low pressure flame synthesized TiO_2 stability with heat treatment. As the sample was heated to 473 K the reflectance decreased (**Figure 6.A1a**) and turned from white to caramel orange (**Figure 6.A1 inset**). Upon continual increase in calcination temperature from 473 K to 673 K the reflectance increased and the sample reverted to white.

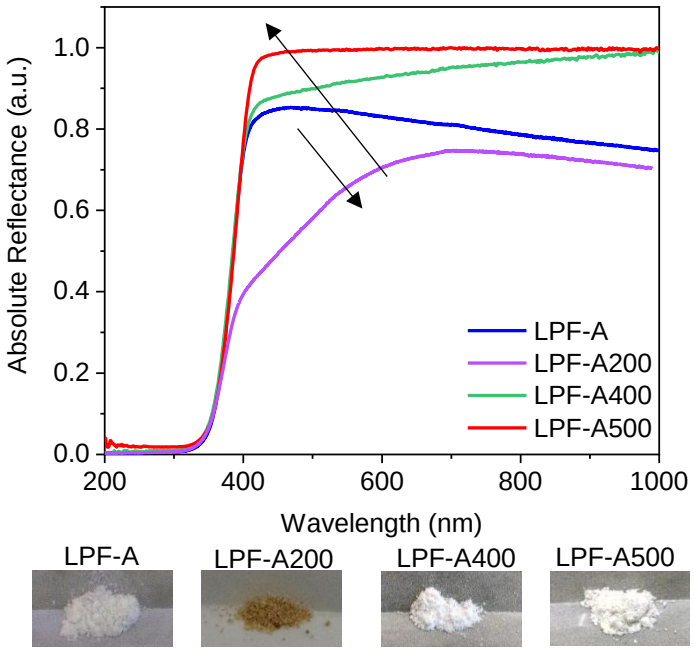

Figure 6.A1 Diffuse Reflectance UV-visible spectroscopy of LPF-A calcined to various temperatures. The inset images show each sample's physical appearance.

6.A.2 Carbon Analysis

Table 6.A1 CHN analysis of commercial anatase compared to low pressure flame synthesized samples calcined to different temperatures (BD indicates below detection of the instrument).

Sample	Carbon	Hydrogen	Nitrogen
Commercial anatase	BD	BD	BD
P25	BD	0.031	BD
LPF-A	1.150%	0.330%	0.007%
LPF-A500	0.068%	0.402%	BD

6.A.3 Surface Area Analysis: Isotherm

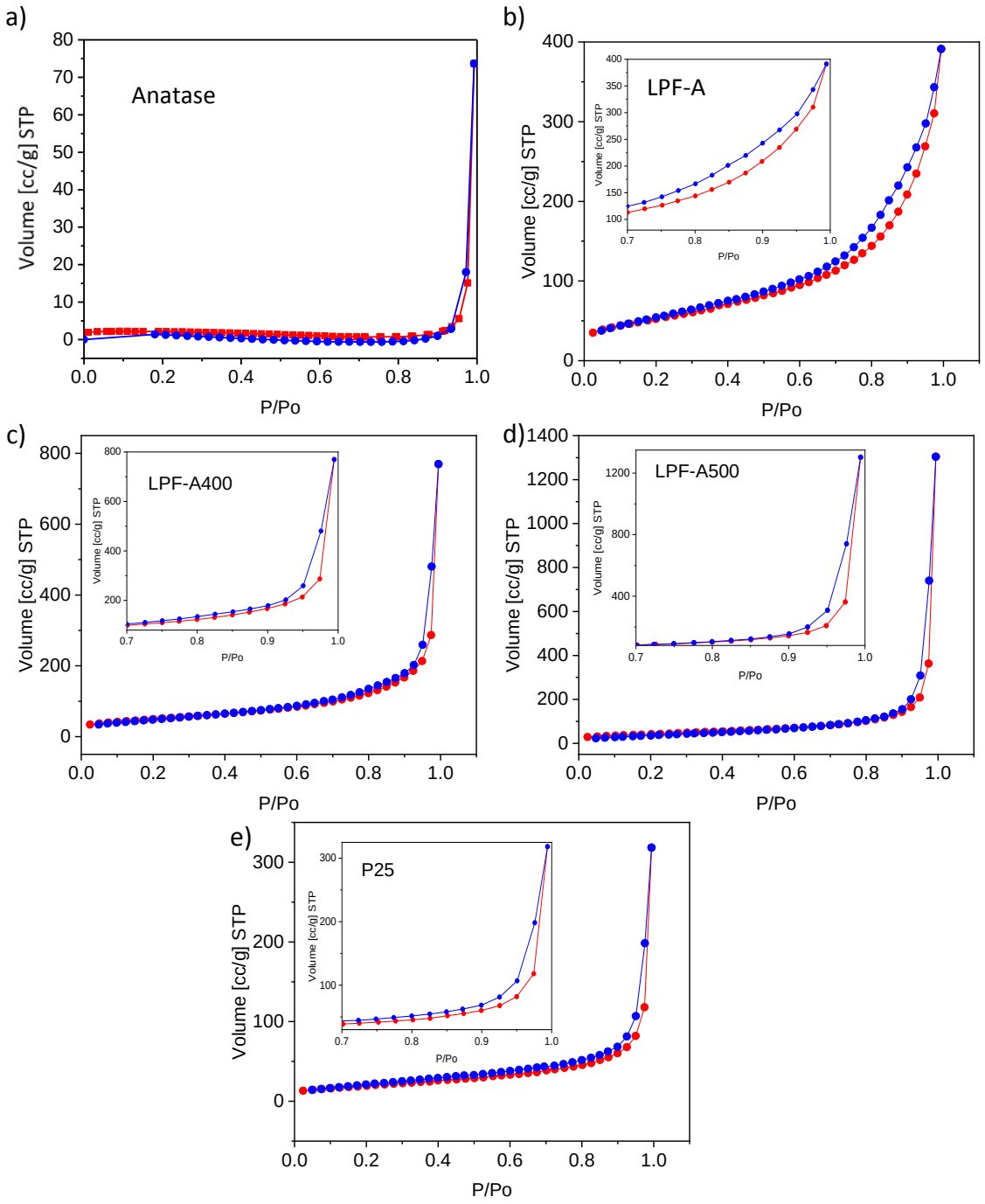

Figure 6.A2 Isotherm at 77 K with nitrogen as the adsorbent for a) commercial anatase, b) LPF-A, c) LPF-A400, d) LPF-A500, and e) Degussa P25.

6.A.4 SEM Analysis

Figure 6.A3 compares the agglomerate structures of commercial anatase, which has a spherical morphology, low pressure flame synthesized anatase (LPF-A), which has a packed cylindrical morphology, and heat treated low pressure flame synthesized anatase (LPF-A200, and LPF-A400) which maintain the packed cylindrical agglomerate structure, with the sample heat treated at 673 K having the largest aggregate diameters of the low pressure flame synthesized samples.

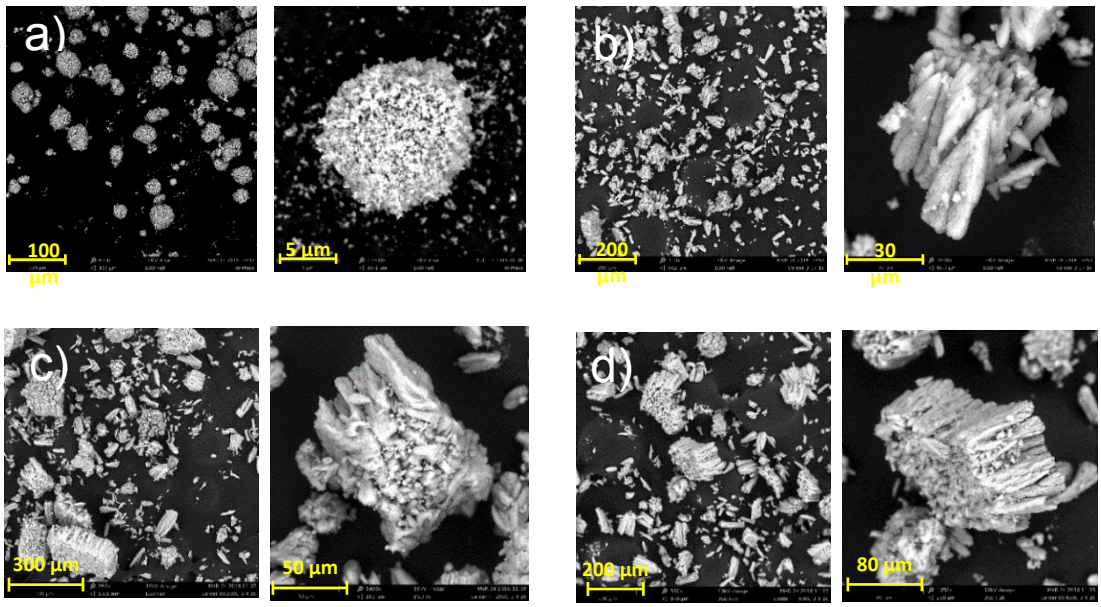

Figure 6.A3 SEM micrographs of a) commercial anatase, b) LPF-A, c) LPF-A200, and d) LPF-A400.

It is noted that on the micron scale, commercial anatase appears relatively spherical and non-porous in their agglomerate morphology, while the low pressure flame synthesized samples appear to have large pores between the packed cylinders, potentially increasing the pore size of these samples.

S.3 TEM and STEM Analysis

Analysis of the Fourier Transform of the STEM micrograph in **Figure 6.3** gives multiple Fourier pairs leading to a rhombus-like shape.

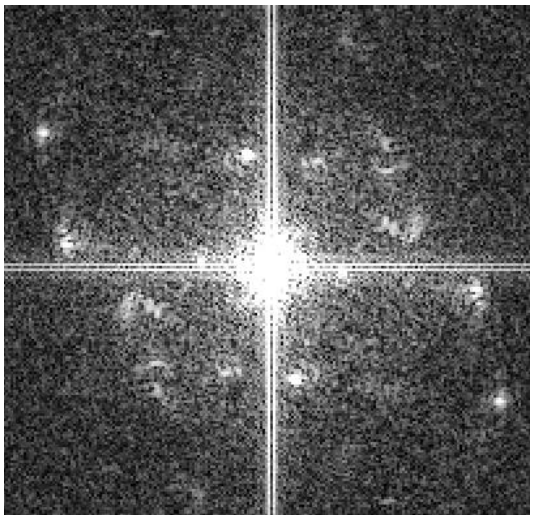

Figure 6.A4 Fast Fourier Transform pattern of LPF-A.

The distance between the pairs divided by two (the distance between the pair and the center) is the inverse of the distance between the lattice spacing. Therefore, by measuring the distance between each pair and taking the inverse divided by two gives the lattice spacing, **Table 6.A2**.

Table 6.A2 Lattice Spacing determined from Fourier Transform of LPF-A STEM Micrograph

Distance Between FFT Pairs (1/nm)	Lattice Distance (nm)	Direction
12.578	0.159	Quadrant 1 to 4
5.455	0.367	Quadrant 1 to 4
9.815	0.204	Quadrant 1 to 4
3.376	0.592	Quadrant 1 to 4
5.348	0.374	Quadrant 2 to 3
7.021	0.285	Quadrant 2 to 3
5.997	0.334	Quadrant 2 to 3

Many of the lattice distances are close to the distance for the 110 face of anatase TiO_2, 0.378 nm. Variations in distance may be attributed to the addition of carbon in the

structure, or ratios of oxygen to titanium that are either sub or super stoichiometric. There are multiple lattice fringes with different spacing and direction in this micrograph. There are two possible explanations, firstly as the nanoparticles form in the reaction zone post flame primary particles (d_p < 5 nm) are formed. Upon quenching the primary particles may agglomerate to form the nanoparticles (d_p = 7.2). During this quenching agglomeration it is possible that two primary particles meet at different faces and form a nanoparticle with multiple lattice spacing. A second reasoning is that the lacey carbon grid had a decent amount of sample distributed on the surface and therefore we may not be looking at one nanoparticle, but many on top of each other. Analysis of 106 lattice fringes indicates that the average spacing is 2.46 Å. The mode was 0.2423 nm with a small percentage having a larger spacing, possibly indicative of carbon doped, and a small percentage having a smaller spacing, possibly indicative of oxygen vacancies of some other crystallographic defect.

Chapter 7: Conclusions and Future Directions

7.1 Unraveling the Phase Composition of Metal Oxide, Degussa P25 TiO_2 via Derivative Peak Fitting of Differential Diffuse Reflectance

The DPR technique represents an important step in understanding the phase behavior and optical properties of semiconductors and metal oxides. This work has shown that physical changes in TiO_2 can affect phase composition as well as susceptibility to rutilization, which can be monitored in situ by DPR. Additionally, DPR shows that the band gap of anatase is preserved across TiO_2 samples prepared and modified by a range of techniques, including grinding, sieving, high-pressure high-temperature annealing, and low-pressure flame synthesis.

7.2 Metal-Free Hydrogen Evolution over Defect-Rich Anatase Phase Titanium Dioxide

High Pressure High Temperature annealing was employed to modify commercial anatase such that the semiconductor could evolve hydrogen from methane steam reforming without the presence of a precious-metal co-catalyst. The photocatalytic cycle for hydrogen evolution over annealed TiO_2 was proposed where Ti^{3+} centers generated during annealing are consumed to produce dihydrogen and then regenerated by the UV-excited electron, thus closing the catalytic cycle. In the absence of UV illumination, the excited electron was not present and these Ti^{3+} cites were quickly consumed thus implicating that photoexcitation is required for the catalytic cycle.

7.3 Photocatalytic Reduction of Coking while Enhancing Hydrogen Production over Nickel supported Anatase

Once again, the presence of precious metal cocatalysts are avoided in the photocatalytic hydrogen production from methane steam reforming. In this project it is revealed that the addition of 1wt% nickel as a cocatalyst on the TiO2 increases CH

activation as well as hydrogen production, with the most promising of the catalysts being the annealed nickel supported on TiO_2 suggesting that the combination of a nickel cocatalyst and a defect-rich metal oxide increases the photocatalytic activity of the catalyst. Additionally, these nickel-supported catalysts are exhibit a major reduction in coking at low steam to carbon ratios when illuminated. Understanding the mechanism by which this coke reduction occurs would be important to both academia and industry alike.

7.4 Properties and Photocatalytic Application of Low Pressure Flame Synthesized Anatase TiO_2

High surface area carbon-doped anatase TiO_2 with mesoporosity and small particle sizes was synthesized via low pressure flame synthesis. This scalable technique allows for the tuning of the TiO_2 polymorph and particle size. The fusing of the small crystallites during quenching produces a sample with mesoporosity caused by void space between a network of fused primary particles. The combination of small particle size (and therefore likely a greater quantum efficiency), high surface area, and large mesopores gives the catalyst unique activity. Hydrogen evolution from water reduction with methanol as a sacrificial agent was the model reaction used to test this activity. LPF-A samples outperformed commercial anatase and commercial (high surface area, fumed) Degussa P25 under UV irradiation.

7.5 Future Directions

7.5.1 Efficacy of the DPR Technique on Various Semiconductors

Band gap energies as well as phase composition of various semiconductors will be analyzed using the DPR method in order to solidify the prowess of the method. DPR can also be applied to systems of other semiconductor and insulator metal oxides. Preliminary work in this area has shown that it is applicable to other semiconductor systems including

zinc oxide, zirconium oxide, and cerium oxide. Intriguing possibilities for DPR include the ability to quantify the relative contribution of different oxidation states within a single sample. Thus showing that the DPR method is a reliable technique for BGE measurements across many semiconductors.

7.5.2 Nickel Metal on Defect Rich TiO_2

The reaction analysis of anatase and defect rich anatase with supported Ni(O) shows an increase in hydrogen production (chapter 5). However, the supported nickel was not reduced and passivated prior to HPHT nor prior to reaction. Since nickel metal is known to be a better hydrogen evolution catalyst than nickel oxide, we propose to repeat these experiments with reduced and passivated samples: Ni/Anatase, HA-Ni/Anatase, Ni/HA-Anatase. The physical properties and the photocatalytic activity of these samples for hydrogen evolution from methane steam reforming will be monitored, as it is expected that metallic nickel on annealed anatase will have a much larger activity due to the metal acting as both and electron trap and a hydrogen evolution site.

7.5.3 HPHT of Low Pressure Flame Synthesized Anatase

Low Pressure Flame Synthesized produces a high surface area, carbon doped anatase phase titanium dioxide, with a particle size of 8.5 nm post calcination. Though these nanoparticles have a large surface area of 149 $m^2\ g^{-1}$, which is promising for photocatalytic applications, and a small particle size, which aids in the quantum efficiency of excitons generated in the bulk being used for reaction, as noted in chapter 6, however below the quantum confinement limit the BGE increases and therefore decreases the efficiency of the catalyst as it is able to absorb fewer photons from irradiated sunlight.

High pressure high temperature annealing has the benefit of inducing photocatalytically active Ti^{3+} centers as noted in chapter 4, however, the treatment increases the particle size by 33-67% from 60 nm to 80-100 nm. Though this increase in particle size is not desirable for a large particle, it could potentially increase the particle size of the low pressure flame synthesized samples to between 10 and 20nm, thus breaching the quantum confinement limit and decreasing the LPF-A BGE to that of a bulk anatase TiO_2 semiconductor ~3.2 eV. The combination of these two techniques is hypothesized to develop an active MSR hydrogen evolution catalyst by increase the particle size past the quantum confinement limit while keeping the size relatively small, and increase surface roughness of the high surface area material while inducing the formation of photocatalytically active Ti^{3+} centers into the material.

References

[1] Kheirandish, A.; Kazemi, M.S.; Dahari, M. Dynamic Performance Assessment of the Efficiency of Fuel Cell-Powered Bicycle: An Experimental Approach. *International Journal of Hydrogen Energy*, *39*, **2014**, 13276-13284.

[2] Hydrogen Analysis Resource Center. U.S. Department of Energy: Energy Efficiency & Renewable Energy, **2015**.

[3] Sandia National Laboratories. US DOE Hydrogen Program 2000 Annual Review, **2000**.

[4] Clariza, L.; Spasiano, D.; Somma, I.D.; Marotta, R.; Andreozzi, R.; Dionysiou, D.D. Copper Modified-TiO_2 Catalysts for Hydrogen Generation Through Photoreforming of Organics. A Short Review. *International Journal of Hydrogen Energy*, *39*, **2014**, 16812-16831.

[5] Kalamaras, C.M.; Efstathiou, A.M. Hydrogen Production Technologies: Current State and Future Developments. *Conference Papers in Energy*, 2013 **2013**, 1-9.

[6] Liu, Q.; Zheng, H. Experimental Research on Low-Temperature Methane Steam Reforming Technology in a Chemically Recuperated Gas Turbine. *ACS, Energy and Fuels*, *28*, **2014**, 6596-6603.

[7] Xu, Y. Schoonen, M.A.A. The Absolute Energy Positions of Conduction and Valence Bands of Selected Semiconducting Minerals. *American Mineralogist*, *85*, **2000**, 543-566.

[8] Serpone, N.; Pelizzetti, E. Photocatalysis Fundamentals & Applications. Wiley, NY, **1989**.

[9] Chen, X.; Lou, Y.; Samia A.C.S.; Burda, C.; Gole, J.L. Formation of Oxynitride as the Photocatalytic Enhancing Site in Nitrogen-Doped Titania Nanocatalysts: Comparison to a Commercial Nanopowder. *Advanced Functional Materials*, *15*, **2015**, 41.

[10] Ni, M.; Leung, M.K.H.; Leung, D.Y.C.; Sumathy, K. A Review and Recent Developments in Photocatalytic Water-Splitting Using TiO_2 for Hydrogen Production, *Renewable and Sustainable Energy Review*, *11*, **2007**, 401

[11] Gázquez, M.J.; Bolívar, J.P.; Garcia-Tenorio, R.; Vaca, F.; A Review of the Production Cycle of Titanium Dioxide Pigment. *MSA Materials Sciences and Applications*, *5*, **2014**.

[12] Scanlon, D.O.; Dunnill, C.W.; Buckeridge, J.; Shevlin, S.A.; Logsdail, A.J.; Woodley, S.M.; Catlow, C.R.A.; Powell, M.J.; Palgrave, R.G.; Parkin, I.P.; Watson, G.W.; Keal, T.W.; Sherwood, P.; Walsh, A.; Sokol, A.A.; Band Alignment of Rutile and Anatase TiO_2. *Nature Materials*, *12*, **2013**, 3697.

[13] Amano, F.; Nakata, M. High-Temperature Calcination and Hydrogen Reduction of Rutile TiO_2: A Method to Improve the Photocatalytic Activity for Water Oxidation. *Applied Catalysis B: Environmental*, *158-159*, **2014**, 202-208.

[14] Barret, C.S.; Massalski, T.B. Structure of Metals McGraw Hill, 3rd edition, **1980**.

[15] Ashcroft, N.W.; Mermin, N.D. Fermi Energies, Fermi Temperatures, and Fermi Velocities. *Hyperphysics*, **2000**.

[16] Miley, G.H. Electrical Cells, Components and Methods. Patent Application Number WO2001063010 A1, **2001**.

[17] Luttrell, T.; Halpegamage, S.; Tao, J.; Kramer, A.; Sutter, E.; Batzill, M. Why is Anatase a Better Photocatalyst than Rutile? – Model Studies on Epitaxial TiO_2 Films. *Nature Scientific Reports*, *4*, **2014**.

[18] Anpo, M.; Shima, T.; Kodama, S.; Kubokawa, Y. Photocatalytic Hydrogenation of CH_3CCH with H_2O on Small-Particle TiO_2: Size Quantization Effects and Reaction Intermediates. *Journal of Physical Chemistry*, *91*, **1987**.

[19] Gueymard, C. The Sun's Total and Spectral Irradiance for Solar Energy Applications and Solar Radiation Models. *Solar Energy*, **2004,** 423–453.

[20] Zhang, H.; Lei, Y.; Kropf, A.J.; Zhang, G.; Elam, J.W.; Miller, J.T.; Sollberger, F.; Ribiero, F.; Akatay, M.C.; Stach, E.A.; Dumessic, J.A. Enhancing the Stability of Copper Chromite Catalysts for the Selective Hydrogenation of Furfural using ALD Overcoating. *Journal of Catalysis*, *317*, **2014**, 284-292.

[21] Tanksale, A.; Beltramini, J.N.; Dumesic, J.A.; Effect of Pt and Pd Promoter on Ni Supported Catalysts— A TPR/TPO/TPD and Microcalorimetry Study. *Journal of Catalysis*, *258*, **2008**, 366-377.

[22] Jentoft, F. Diffuse reflectance IR and UV-vis Spectroscopy, Modern Methods in Heterogeneous Catalysis. *Fritz Harbor Institute*, **2004**.

[23] Eaton, G.R.; Eaton, S.S.; Barr, D.P.; Weber, R.T. Quantitative EPR. *SpringerWein New York*, **2010**, DIO 10.1007/978-3-211-92948-3

[24] Winter, M. **2017** Accessed 8/2017 https://www.webelements.com/copper/isotopes.html

[25] Ohno, T.; Sarukawa, K.; Tokieda, K.; Matsumura, M.; Morphology of a TiO_2 Photocatalyst (Degussa, P-25) Consisting of Anatase and Rutile Crystalline Phases. *Journal of Catalysis*, *203*, **2001**, 82-86.

[26] Hurum, D.C.; Agrios, A.G.; Gray, K.A.; Explaining the Enhanced Photoactivity of Degussa P25 Mixed-Phase TiO_2 Using EPR. *Journal of Physical Chemistry B*, *107*, **2003**, 4545-4549.

[27] Hashimoto, K.; Irie, H.; Fujishima, A. TiO_2 Photocatalysis: A Historical Overview and Future Prospects. *Japanese Journal of Applied Physics*, *44*, **2005**, 8269-8285.

[28] Trejo-Tzab, R.; Alvarado-Gil, J.J.; Quintana, P. Photocatalytic Activity of Degussa P25 TiO_2/Au Obtained Using Argon (Ar) and Nitrogen (N_2) Plasma. *Topics in Catalysis*, *54*, **2011**, 250-256.

[29] Schneider, J.; Matsuoka, M.; Takeuchi, M.; Zhang, J.; Horiuchi, Y.; Anpo, M.; Bahnemann, D.W. Understanding TiO_2 Photocatalysis: Mechanisms and Materials. *Chemical Reviews*, *114*, **2014**, 9919-9986.

[30] Tilocca, A.; Selloni, A. Methanol Adsorption and Reactivity on Clean and Hydroxylated Anatase(101) Surfaces. *J. Phys. Chem. B*, *108*, **2004**, 19314-19319.

[31] Bacsa, R.R.; Kiwi, J. Effect of Rutile Phase on The Photocatalytic Properties of Nanocrystalline Titania during the Degradation of *p*-coumaric Acid. *Applied Catalysis B*, *16*, **1998**, 19-29.

[32] Janus, M.; Morawski, A.W. New Method of Improving Photocatalytic Activity of Commercial Degussa P25 for Azo Dyes Decomposition. *Applied Catalysis B*, *75*, **2007**, 118-123.

[33] Schmidt, C.M.; Weitz, E.; Geiger, F.M. Interaction of the Indoor Air Pollutant Acetone with Degussa P25 TiO_2 Studied by Chemical Ionization Mass Spectrometry. *Langmuir*, *22*, **2006**, 9642-9650.

[34] Jiang, X.; Manawan, M.; Feng, T.; Qian, R.; Zhao, T.; Zhou, G.; Kong, F.; Wang, Q.; Dai, S.; Pan, J.H. Anatase and Rutile in Evonik Aeroxide P25: Heterojunctioned or Individual Nanoparticles? *Catalysis Today*, *300*, **2018**, 12-17.

[35] Evonik Industries, AEROXIDE®, AERODISP, and AEROPERL Titanium Dioxide as a Photocatalyst. Technical Information TI 1243, **2015**, 1-12.

[36] Jensen. H.; Joensen, K.D.; Jørgensen, J.; Pedersen, J.S.; Søgaard, E.G. Characterization of Nanosized Partly Crystalline Photocatalysts. *Journal of Nanoparticle Research, 6*, **2004**, 519-526.

[37] Ohtani, B; Prieto-Mahaney, O.O.; Li, D.; Abe, R. What is Degussa (Evonik) P25? Crystalline Composition Analysis, Reconstruction from Isolated Pure Particles and Photocatalytic Activity Test. *Journal of Photochemistry and Photobiology A-Chem.*, **2010**, *216*, 179-182.

[38] Tobaldi, D.M.; Pullar, R.C.; Seabra, M.P.; Labrincha, J.A. Fully Quantitative X-ray Characterisation of Evonik Aeroxide TiO_2 P25®. *Materials Letters*, *122*, **2014**, 345-347.

[39] Lebedev, V.A.; Kozlov, D.A.; Kolesnik, I.V.; Poluboyarinov, A.S.; Becerikli, A.E.; Grünert, W.; Garshev, A.V. The Amorphous Phase in Titania and its Influence on Photocatalytic Properties. *Applied Catalysis B*, *195*, **2016**, 39-47.

[40] Bickley, R.I.; Gonzalex-Carreno, T.A.; Lees, J.S.; Palmisano, L.; Tilley, R.J.D. A Structural Investigation of Titanium Dioxide Photocatalysts. *Journal of Solid State Chemistry, 92*, **1991**, 178-190.

[41] Wang, G.; Xu, L.; Zhang, J.; Yin, T.; Han, D. Enhanced Photocatalytic Activity of TiO_2 Powders (P25) via Calcination Treatment. *International Journal of Photoenergy*, *2012*, **2012**, 265760.

[42] Vijayarangamuthu, K.; Han, H.E.; Jeon, K.J. Low Frequency Ultrasonication of Degussa P25 TiO_2 and its Superior Photocatalytic Properties. *Journal of Nanoscience and Nanotechnology*, *16*, **2016**, 4399-4404.

[43] Zhang, Z.L.; Li, D.N.; Mao, Y.L.; Effects of Trap Density on the Surface-Enhanced RamanScattering of Molecules Adsorbed on TiO_2 (Degussa P25). *Journal of Raman Spectroscopy*, *43*, **2012**, 1920-1923.

[44] Yang, L.; Gong, M.; Jiang, X.; Yin, D.; Qin, X.; Zhao, B.; Ruan, W. Investigation on SERS of Different Phase Structure TiO_2 Nanoparticles. *Journal of Raman Spectroscopy, 46*, **2015**, 287-292.

[45] Rengifo-Herrera, J.A.; Fidalgo de Cortalezzi, M.M.; Pizzio, L.R. Visible-light-absorbing Evonik P-25 Nanoparticles Modified with Tungstophosphoric Acid and Their Photocatalytic Activity on Different Wavelengths. *Materials Research Bulletin*, *83*, **2016**, 360-368.

[46] Vorontsov, A.V.; Altynnikov, A.A.; Savinov, E.N.; Kurkin, E.N. Correlation of TiO_2 Photocatalytic Activity and Diffuse Reflectance Spectra. *Journal of Photochemistry and Photobiology A*, *144*, **2001**, 193-196.

[47] Breeson, A.C.; Sankar, G.; Goh, G.K.L.; Palgrave, R.G. Phase Quantification by X-ray Photoemission Valence Band Analysis Applied to Mixed Phase TiO_2 powders. *Applied Surface Science*, *423*, **2017**, 205-209.

[48] Deskins, N.A.; Kerisit, S.; Rosso, K.M.; Dupuis, M. Molecular Dynamics Characterization of Rutile-Anatase Interfaces. *Journal of Physical Chemistry C*, *111*, **2007**, 9290-9298.

[49] Wergner, K.; Pratsinis, S.E. Gas-Phase Synthesis of Nanoparticles: Scale-Up and Design of Flame Reactors. *Powder Technology*, *150*, **2005**, 117-122.
[50] Tauc, J.; Grigorovici, R.; Vancu, A. Optical Properties and Electronic Structure of Amorphous Germanium. *Physica Status Solidi*, *15*, **1966**, 627-637.
[51] Davis, E.A; Mott, N.F. Conduction in Non-Crystalline Systems V: Conductivity, Optical Absorption and Photoconductivity in Amorphous Semiconductors, *Philosophical Magazine*, *22*, **1970**, 903-922.
[52] Michalow, K.A.; Logvinovich, D.; Weidenkaff, A.; Amberg, M.; Fortunato, G.; Heel, A.; Graule, T.; Rekas, M. Synthesis, Characterization and Electronic Structure of Nitrogen-doped TiO_2 Nanopowder. *Catalysis Today*, *144*, **2009**, 7-12.
[53] Viezbicke, B.D.; Patel, S.; Davis, B.E.; Birnie III, D.P. Evaluation of the Tauc Method for Optical Absorption Edge Determination: ZnO Thin Films as a Model System. *Physica Status Solidi B*, *252*, **2015**, 1700-1710.
[54] Dolgonos, A.; Mason, T.O.; Poeppelmeier, K.R. Direct Optical Band Gap Measurement in Polycrystalline Semiconductors: A Critical Look at the Tauc Method. *Journal of Solid State Chemistry*, *240*, **2016**, 43-48.
[55] Apopei, P.; Catrinescu, C.; Teodosiu, C.; Royer, S. Mixed-phase TiO_2 Photocatalysts: Crystalline Phase Isolation and Reconstruction, Characterization and Photocatalytic Activity in the Oxidation of 4-chlorophenol from Aqueous Effluents. *Applied Catalysis B*, *160*, **2014**, 374-382.
[56] Borensztein, Y.; Delannoy, L.; Barrera, R.G.; Louis, C. Kinetics of the Plasmon Optical Response of Au Nanoparticles/TiO_2 Catalyst under O_2 and H_2 Followed by Differential Diffuse Reflectance Spectroscopy. *The European Physical Journal D*, *63*, **2011**, 235-240.
[57] Molinari, A.; Bonino, F.; Magnacca, G.; Demaria, F.; Maldotti, A. Relation between Phase Composition and Photocatalytic Photoactivity of TiO_2 in a Sulfoxide Deoxygenation Reaction. *Materials Chemistry and Physics*, *158*, **2015**, 60-66.
[58] Chiarello, G.L.; Selli, E.; Forni, L. Photocatalytic Hydrogen Production over Flame Spray Pyrolysis-Synthesised TiO_2 and Au/TiO_2. *Applied Catalysis B*, *84*, **2008**, 332-339.
[59] Kuś, S.; Marczenko, Z.; Obarski, N. Derivative UV-Vis Spectrophotometry in Analytical Chemistry. *Chemia Analityczna -Warsaw*, *41*, **1996**, 899-929.
[60] Karpińska, J. Derivative Spectrophotometry— Recent Applications and Directions of Developments. *Talanta*, *64*, **2004**, 801-822.
[61] Parmar, A.; Sharma, S.; Derivative UV-Vis Absorption Spectra as Invigorated Spectrophotometric Method for Spectral Resolution and Quantitative Analysis: Theoretical Aspects and Analytical Applications: A Review. *TrAC-Trends in Analytical Chemistry*, *77*, **2016**, 44-53.
[62] Wojdyr, M. Fityk: A General-Purpose Peak Fitting Program. *Journal of Applied Crystallography*, *43*, **2010**, 1126-1128.
[63] Mora-Seró, I.; Bisquert, J. Fermi Level of Surface States in TiO_2 Nanoparticles. *Nano Letters*, *3*, **2003**, 945-949.
[64] Kho, Y.K.; Iwase, A.; Teoh, W.Y.; Mädler, A.; Kudo, A.; Amal, R. Photocatalytic H_2 Evolution over TiO_2 Nanoparticles. The Synergistic Effect of Anatase and Rutile. *Journal of Physical Chemistry C*, *114*, **2010**, 2821-2829.

[65] Molinari, A.; Bonino, F.; Magnacca, G.; Demaria, F.; Maldotti, A. Relation between phase composition and photocatalytic activity of TiO_2 in a sulfoxide deoxygenation reaction. *Materials Chemistry Physics*, **2015**, *158*, 60-66.

[66] Shen, S.; Wang, X.; Chen, T.; Feng, Z.; Li, C. Transfer of Photoinduced Electrons in Anatase−Rutile TiO_2 Determined by Time-Resolved Mid-Infrared Spectroscopy. *Journal of Physical Chemistry C*, *118*, **2014**, 12661-12668.

[67] Hirano, M.; Nakahara, N.; Ota, K.; Tanaike, O.; Inagaki, N. Photoactivity and Phase Stability of ZrO_2-Doped Anatase-Type TiO_2 Directly Formed as Nanometer-Sized Particles by Hydrolysis under Hydrothermal Conditions. *Journal of Solid State Chemistry*, *170*, **2003**, 39-47.

[68] Li, G.S.; Li, L.P.; Boerio-Goates, J.; Woodfield, B.F. High Purity Anatase TiO_2 Nanocrystals: Near Room-Temperature Synthesis, Grain Growth Kinetics, and Surface Hydration Chemistry. *Journal of the American Chemical Society*, *127*, **2005**, 8659-8666.

[69] Zhang, H.; Banfield, J.F. Phase Transformation of Nanocrystalline Anatase-to-Rutile via Combined Interface and Surface Nucleation. *Journal of Materials Research*, *15*, **2000**, 437-448.

[70] Hanaor, D.A.H.; Sorrell, C.C. Review of the Anatase to Rutile Phase Transformation. *Journal of Material Science 46*, **2011,** 855-874.

[71] Šepelák, V.; Bégin-Colin, S.; Le Caër, G. Transformations in Oxides Induced by High-energy Ball-milling. *Dalton Transactions*, *41*, **2012**, 11927-11948.

[72] Gajovik, A.; Furic, K.; Tomasic, N.; Popovic, S.; Skoko, Z.; Music, S. Mechanochemical Preparation of Nanocrystalline TiO_2 Powders and Their Behavior at High Temperatures. *Journal of Alloys and Compounds*, *398*, **2008**, 188-199.

[73] Hu, J.; Qin, H.; Sui, Z.; Lu, H. Characteristic of Mechanically Milled TiO_2 Powders. *Materials Letters*, *53*, **2002**, 421-424.

[74] Pan, X.; Ma, X. Study on the Milling-Induced Transformation in TiO_2 Powder with Different Grain Sizes. *Materials Letters*, *58*, **2004**, 513-515.

[75] Sekiya, T.; Ohta, S.; Kamei, S.; Hanakawa, N.; Kurita, S. Raman Spectroscopy and Phase Transition of Anatase TiO_2 Under High Pressure. *Journal of Physics and Chemistry of Solids*, *62*, **2001**, 717–721.

[76] Hwang, S.L.; Shen, P.; Chu, H.-T.; Yui, T.-F. *Science*, *288*, **2000**, 321–324.

[77] Saitow, K.; Wakamiya, T. 130-Fold Enhancement of TiO_2 Photocatalytic Activities by Ball Milling. *Applied Physics Letters*, *103*, **2013**, 031916.

[78] Levchenko, A.A.; Li, G.; Boerio-Goates, J.; Woodfield, B.F.; Navrotsky, A. TiO_2 Stability Landscape: Polymorphism, Surface Energy, and Bound Water Energetics. *Chemistry of Materials*, *18*, **2006**, 6324-6332.

[79] Barthelmy, D. Mineralogy Database. http://webmineral.com (accessed Jan 5, 2018).

[80] Liu, G.; Yang, H.A.; Pan, J.; Yang, Y.Q.; Lu, G.Q.; Cheng, H.M. Titanium Dioxide Crystals with Tailored Facets. *Chemical Reviews*, *114*, **2014**, 9559-9612.

[81] Han, X.; Zheng, B.; Ouyang, J.; Wang, X.; Kuang, Q.; Jiang, Y.; Xie, Z.; Zheng, L. Control of Anatase TiO_2 Nanocrystals with a Series of High-Energy Crystal Facets via a Fuorine-Free Strategy. *Chemistry—An Asian Journal*, *7*, **2012**, 2538-2542.

[82] Lee, M.K.; Park, Y.C. Super-hydrophilic Anatase TiO_2 Thin Film In-situ Deposited by DC Magnetron Sputtering. *Thin Solid Films*, *638*, **2017**, 9-16.

[83] Jiang, H. B.; Cuan, Q.; Wen, C. Z.; Xing, J.; Wu, D.; Gong, X.-Q.; Li, C.; Yang, H. G. Anatase TiO_2 Crystals with Exposed High-Index Facets. *Angewandte Chemie International Edition*, *50*, **2011**, 3764-3768.

[84] Lu, J.; Dai, Y.; Jin, H.; Huang, B. Effective Increasing of Optical Absorption and Energy Conversion Efficiency of Anatase TiO_2 Nanocrystals by Hydrogenation. *Physical Chemistry Chemical Physics*, *13*, **2011**, 18063-18068.

[85] Burdett, J.K.; Hughbanks, T.; Miller, G.T.; Richardson, J.W. Jr; Smith, J.V. Structural-Electronic Relationships in Inorganic Solids: Powder Neutron Diffraction Studies of the Rutile and Anatase Polymorphs of Titanium Dioxide at 15 and 295 K. *Journal of the American Chemical Society*, *109*, **1987**, 3639-3646.

[86] Bessergnenev, V.G; Mateus, M.C; Botelho do Rego, A.M.; Hantusch, M.; Burkel, E. An Improvement of Photocatalytic Activity of TiO_2 Degussa P25 powder. *Applied Catalysis A*, *500*, **2015**, 40-50.

[87] Li, C.L.; Chen, W.; Yuan, J.; Shangguan W.F. Hydrogen Evolution by Photocatalytic Steam Reforming of Methane over Pt/TiO_2. *Acta Physico-Chimica Sinica*, *28*, **2012**, 450.

[88] Xiong, L.B.; Li, J.L.; Yang, B.; Yu, Y. Ti^{3+} in the Surface of Titanium Dioxide: Generation, Properties and Photocatalytic Application. *Journal of Nanomaterials*, *2012*, **2012**, 831524.

[89] Fujishima, A.; Honda. K. Electrochemical Photolysis of Water at a Semiconductor Electrode. *Nature*, *238*, **1972**, 37.

[90] Al-Mazroai, L.S.; Bowker, M.; Davies, P.; Dickinson, A.; Greaves, J.; James, D.; Millard. L. The Photocatalytic Reforming of Methanol. *Catalysis Today*, *122*, **2007**, 46-50.

[91] Highfield, J.G.; Chen, M.H.; Nguyen, P.T.; Chen. Z. Mechanistic Investigations of Photo-Driven Process over TiO_2 by in-situ DRIFTS-MS: Part 1. Platinum and Methanol Reforming. *Energy and Environmental Science*, *2*, **2009**, 991.

[92] Chiarello, G.L.; Forni, L.; Selli. E. Photocatalytic Hydrogen Production by Liquid- and Gas-Phase Reforming of CH_3OH Over Flame-Made TiO_2 and Au/TiO_2. *Catalysis Today*, *144*, **2009**, 69.

[93] Chiarello, G.L.; Aguirre, M.H.; Selli, E. Hydrogen Production by Photocatalytic Steam Reforming of Methanol on Noble Metal-modified TiO_2. *Journal of Catalysis*, *273*, **2010**, 182-190.

[94] Chiarello, G.L.; Aguirre, M.H.; Selli. E. Effect of the CH_3OH/H_2O Ratio on the Mechanism of the Gas-Phase Photocatalytic Reforming of Methanol on Noble Metal-Modified TiO_2. *Journal of Catalysis*, *280*, **2011**, 177.

[95] Shen, M.; Henderson. M.A. Identification of the Active Species in Photochemical Hole Scavenging Reactions of Methanol on TiO_2. *Journal of Physical Chemistry Letters*, *2*, **2011**, 2707.

[96] Shen, M.; Henderson. M.A. Role of Water in Methanol Photochemistry on Rutile TiO_2(110). *Journal of Physical Chemistry C*, *116*, **2012**, 18788.

[97] Shen, M.; Acharya, D.P.; Dohnálek, Z.; Henderson. M.A. Importance of Diffusion in Methanol Photochemistry on TiO_2(110). *Journal of Physical Chemistry C*, *116*, **2012**, 25465.

[98] Phillips, K.R.; Jensen, S.C.; Baron, M.; Li, S.; Friend. C.M. Sequential Photo-Oxidation of Methanol to Methyl Formate on TiO_2(110). *Journal of the American Chemical Society*, *135*, **2013**, 574.

[99] Chiarello, G.L.; Dozzi, M.V.; Scavini, M.; Grunwaldt, J.; Selli. E. One Step Flame-Made Fluorinated Pt/TiO_2 Photocatalysts for Hydrogen Production. *Applied Catalysis B: Environmental*, *160-161*, **2014**, 144-151.

[100] Nomikos, G.N.; Panagiotopoulou, P.; Kondarides, D.I.; Verykios. X.E. Kinetic and Mechanic Study of the Photocatalytic Reforming of Methanol over Pt/TiO_2 Catalyst. *Applied Catalysis B: Environmental*, *146*, **2014**, 249.

[101] Kennedy, J.; Jones, W.; Morgan, D.J.; Bowker, M.; Lu, L.; Kiely, C.J.; Wells, P.P.; Dimitratos; N. Photocatalytic Hydrogen Production by Reforming of Methanol using Au/TiO_2, Ag/TiO_2 and Au-Ag/TiO_2 Catalysts. *Catalysis, Structure and Reactivity*, *1*, **2015**, 35.

[102] Fu, X.; Long, J.; Wang, X.; Leung, D.Y.C.; Ding, Z.; Wu, L.; Zhang, Z.; Li, Z.; Fu. X. Photocatalytic Reforming of Biomass: A Systematic Study of Hydrogen Evolution from Glucose Solution. *International Journal of Hydrogen Energy*, *33*, **2008**, 6484.

[103] Navarro, R.M.; Sánchez-Sánchez, M.C.; Alvarez-Galvan, M.C.; del Valle, F.; Fierro, J.L.G. Hydrogen Production from Renewable Sources: Biomass and Photocatalytic Opportunities. *Energy & Environmental Science*, *2*, **2009**, 35.

[104] Kondarides, D.I.; Daskalaki, V.M.; Patsourna, A.; Verykios. X.E. Hydrogen Production by Photo-Induced Reforming of Biomass Components and Derivatives at Ambient Conditions. *Catalysis Letters*, *122*, **2008**, 26.

[105] Rossetti. I.; Hydrogen Production by Photoreforming of Renewable Substrates. *ISRN Chemicial Engineering*, *2012*, **2012**, 964936.

[106] Gu, Q.; Long, J.; Fan, L.; Chen, L.; Zhao, L.; Lin, H.; Wang. X. Single-Site Sn-Grafted Ru/TiO_2 Photocatalysts for Biomass Reforming: Synergistic Effect of Dual Co-Catalysts and Molecular Mechanism. *Journal of Catalysis*, *303*, **2013**, 141.

[107] Clariza, L; Spasiano, D.; Somma, I.D.; Marotta, R.; Andreozzi, R.; Dionysiou. D.D. Copper Modified-TiO_2 Catalysts for Hydrogen Generation Through Photoreforming of Organics. A short review. *International Journal of Hydrogen Energy*, *39*, **2014**, 16812.

[108] Jacobson, M.Z.; Colella, W.G.; Golden, D.M. Cleaning the Air and Improving Health with Hydrogen Fuel-Cell Vehicles. *Science*, *308*, **2005**, 1901.

[109] Edwards, P.P.; Kuznetsov, V.L.; David, W.I.F.; Brandon, N.P. Hydrogen and Fuel Cells: Towards A Sustainable Energy Future. *Energy Policy*, *36*, **2008**, 4356.

[110] Deb, M.; Sastry, G.R.K.; Bose, P.K.; Banerjee, R. An Experimental Study on Combustion, Performance and Emission Analysis of A Single Cylinder, 4-Stroke DI-Diesel Engine using Hydrogen in Dual Fuel Mode of Operation. *International Journal of Hydrogen Energy*, *40*, **2015**, 8586.

[111] Agrafiotis, C.; von Storch, H.; Roeb, M.; Sattler, C. Solar Thermal Reforming of Methane Feedstocks for Hydrogen and Syngas Production—A Review. *Renewable and Sustainable Energy Reviews*, *29*, **2014**, 656-682.

[112] Barreto, L.; Makihira, A.; Riahi, K. The Hydrogen Economy in the 21st Century: A Sustainable Development Scenario. *International Journal of Hydrogen Energy*, *28*, **2003**, 267-284.

[113] Chen, H.; Ding, Y.; Cong, N.; Dou, B.; Dupont, V.; Ghadiri, M.; Williams, P. Progress in Low Temperature Hydrogen Production with Simultaneous CO_2 Abatement. *Chemical Engineering Research and Design*, *89*, **2011**, 1774-1782.

[114] Wang, F.; Tan, J.; Ma, L.; Leng, Y. Effects of Key Factors on Solar Aided Methane Steam Reforming in Porous Medium Thermochemical Reactor. *Energy Conversion and Management*, *103*, **2015**, 419-430.

[115] Baltrusaitis, J.; Jansen, I.; Schuttlefield Christus, J.D. Renewable Energy Based Catalytic CH_4 Conversion to Fuels. *Catalysis Science & Technology*, *4*, **2014**, 4.

[116] Shimura, K.; Yoshida, H. Heterogeneous Photocatalytic Hydrogen Production from Water and Biomass Derivatives. *Energy & Environmental Science*. *4*, **2011,** 2467.

[117] G. Myhre, D. Shindell, F.-M. Bréon, W. Collins, J. Fuglestvedt, J. Huang, D. Koch, J.-F. Lamarque, D. Lee, B. Mendoza, T. Nakajima, A. Robock, G. Stephens, T. Takemura and H. Zhang. Anthropogenic and Natural Radiative Forcing. In: Climate Change 2013: The Physical Science Basis. Contribution of Working Group I to the Fifth Assessment Report of the Intergovernmental Panel on Climate Change. Stocker, T.F., D. Qin, G.-K. Plattner, M. Tignor, S.K. Allen, J. Boschung, A. Nauels, Y. Xia, V. Bex and P.M. Midgley (eds.). Cambridge University Press, Cambridge, United Kingdom and New York, NY, USA. **2013**.

[118] Fuqiang, W.; Jianyu, T.; Lanxin, M.; Yu, L. Effects of Key Factors on Solar Aided Methane Steam Reforming in Porous Medium Thermochemical Reactor. *Energy Conversion and Management*, *103*, **2015**, 419.

[119] Yoshida, H.; Kato, S.; Hirao, K.; Nishimoto, J.I.; Hattori, T. Photocatalytic Steam Reforming of Methane over Platinum-Loaded Semiconductors for Hydrogen Production. *Chemistry Letters*, *36*, **2007**, 430-431.

[120] Yoshida, H.; Hirao, K.; Nishimoto, J.I.; Shimura, K.; Kato, S.; Itoh, H.; Hattori, T. Hydrogen Production from Methane and Water on Platinum Loaded Titanium Oxide Photocatalysts. *Journal of Physical Chemistry C*, *112*, **2008**, 5542-5551.

[121] Yuliati, L.; Yoshida, H. Photocatalytic Conversion of Methane. *Chemical Society Reviews*, *37*, **2008**, 1592-1602.

[122] Yoshida, H. Photocatalytic Hydrogen Production from Methane and Water. *Handbook of Photocatalysts: Preparation, Structure and Applications, G.K. Castello ed. Nova Science Publishers Hauppauge*, NY, **2010,** 535.

[123] Shimura, K.; Kato, S.; Yoshida, T.; Itoh, H.; Hattori, T.; Yoshida. H. Photocatalytic Steam Reforming of Methane over Sodium Tantalate. *Journal of Physical Chemistry C*, *114*, **2010**, 3493-3503.

[124] Shimura, K.; Yoshida, H. Hydrogen Production from Water and Methane over Pt-Loaded Calcium Titanate Photocatalyst. *Energy & Environmental Science*, *3*, **2010**, 615-617.

[125] Shimura, K.; Yoshida, T.; Yoshida, H. Photocatalytic Activation of Water and Methane over Modified Gallium Oxide for Hydrogen Production. *Journal of Physical Chemistry C*. *114*, **2010**, 11466-11474.

[126] Shimura, K.; Kawai, H.; Yoshida, T.; Yoshida, H. Bifunctional Rhodium Cocatalysts for Photocatalytic Steam Reforming Methane over Alkaline Titanate. *ACS Catalysis*, *2*, **2012**, 2126-2134.

[127] Yamakata, A.; Ishibashi, T.; Onishi, H.; Water- and Oxygen-Induced Decay Kinetics of Photogenerated Electrons in TiO_2 and Pt/TiO_2: A Time-Resolved Infrared Absorption Study. *Journal of Physical Chemistry B, 105,* **2001**, 7258-7262.

[128] Gurylev, V.; Su, C.Y.; Perng, T.P. Surface Reconstruction, Oxygen Vacancy Distribution and Photocatalytic Activity of Hydrogenated Titanium Thin Film. *Journal of Catalysis*, *330*, **2015**, 177-186.

[129] Liu, H.; Ma, H. T.; Li, X.Z.; Li, W.Z.; Wu, M.; Bao, X.H. The Enhancement of TiO_2 Photocatalytic Activity by Hydrogen Thermal Treatment, *Chemosphere*, *50*, **2003**, 39–46.

[130] Marucco, J.F.; Gautron, J.; Lemasson, P. Thermogravimetric and Electrical Study of Nonstoichiometric Titanium-Dioxide TiO_{2-x} Between 800 and 1100-Degrees-C. *Journal of Physics and Chemistry of Solids*, *42*, **1981**, 412.

[131] Plugaru, R. Optical Properties of Nanocrystalline Titanium Oxide. *Thin Solid Films*, *516*, **2008**, 8179.

[132] Sekiya, T.; Yagisawa, T.; Kurita, S. Annealing of Anatase Titanium Dioxide under Hydrogen Atmosphere. *Journal of the Ceramic Society of Japan*, *109*, **2001**, 672.

[133] Chen, X.; Liu, L.; Yu, P.Y.; Mao, S.S. Increasing Solar Absorption for Photocatalysis with Black Hydrogenated Titanium Dioxide Nanocrystals. *Science*, *331,* **2011,** 746-750.

[134] Wang, G.; Wang, H.; Ling, Y.; Tang, Y.; Yang, X.; Fitzmorris, R.C.; Wang, C.; Zhang, J.Z.; Li, Y. Hydrogen-Treated TiO_2 Nanowire Arrays for Photoelectrochemical Water Splitting. *Nano Letters*, *11*, **2011**, 3026.

[135] Xin, X.; Xu, T.; Yin, J.; Wang, L.; Wang, C. Management on the Location and Concentration of Ti^{3+} in Anatase TiO_2 for Defects-Induced Visible-Light Photocatalysis. *Applied Catalysis B: Environmental*, *176-177*, **2015**, 354-362.

[136] Mehta, M.; Kodan, N.; Kumar, S.; Kaushal, A.; Mayrhofer, L.; Walter, M.; Moseler, M.; Dey, A.; Krishnamurthy, S.; Basu, S.; Singh, A.P. Hydrogen Treated Anatase TiO_2: A New Experimental Approach and Further Insights from Theory. *Journal of Materials Chemistry A*, *4*, **2016**, 2670-2681.

[137] Nandasir, M.I.; Shutthanandan, V.; Manandhar, S.; Schwarz, A.M.; Oxenford, L.; Kennedy, J.V.; Thevuthasan, S.; Henderson, M.A. Instability of Hydrogenated TiO_2. *The Journal of Physical Chemistry Letters*, *6*, **2015**, 4627-4632.

[138] Misra, S.K.; Andronenko, S.I.; Tipikin, D.; Freed, J.H.; Somani, V.; Prakash, O. Study of Paramagnetic Defect Centers in As-Grown and Annealed TiO_2 Anatase and Rutile Nanoparticles by a Variable-Temperature X-band and High-Frequency (236 Ghz) EPR. *Journal of Magnetism and Magnetic Materials*, *401*, **2016**, 495-505.

[139] Verardo, D.J.; Froelich, P.N.; McIntyre, A. Determination of Organic Carbon and Nitrogen in Marine Sediments using Carlo Erba NA-1500 Analyzer. *Deep-Sea Research*, *37*, **1990**, 157-165.

[140] Biedron, A.B.; Garfunkel, E.L.; Castner Jr., E.W.; Rangan, S. Ionic Liquid Ultrathin Films at The Surface of Cu(100) and Au(111). *The Journal of Chemical Physics*, *146*, **2017**, 054704.

[141] Nesbitt, H.W.; Banerjee, D. Interpretation of XPS Mn(2p) Spectra of Mn Oxyhydroxides and Constraints on The Mechanism of MnO_2 Precipitation. *American Mineralogist*, *83*, **1998**, 305−315.

[142] Strunk, J.; Vining, W.C.; Bell, A.T.; A Study of Oxygen Vacancy Formation and Annihilation in Submonolayer Coverages of TiO_2 Dispersed on MCM-48, *Journal of Physical Chemistry C*, *114*, **2010**, 16937-16945

[143] Jiang, J.; Weber, R.T. ELEXSYS E 500 USER'S MANUAL Basic Operations, Bruker Instruments, Inc. Version 2.0, **2001**.

[144] Tran, V.A.; Truong, T.T.; Phan, T.A.P.; Nguyen, T.N.; Huynh, T.V.; Agresti, A.; Pescetelli, S.; Le, T.K.; Carlo, A.D.; Lund, T.; Le, S.N.; Nguyen, P.T. Application of Nitrogen-Doped TiO_2 Nano-Tubes in Dye-Sensitized Solar Cells. *Applied Surface Science*, *399*, **2017**, 515-522.

[145] Yu, Y.; Wu, K.; Wang, D. Dye-Sensitized Solar Cells with Modified TiO_2 Surface Chemical States: The Role of Ti^{3+}. *Applied Physics Letters*, *99*, **2011**, 192104.

[146] Zhu, J.; Yang, J.; Bian, Z.-F.; Ren, J.; Liu, Y.-M.; Cao, Y.; Li, H.-X.; He, H.-Y.; Fan, K.-N. Nanocrystalline Anatase TiO_2 Photocatalysts Prepared via Facile Low Temperature Nonhydrolytic Sol-gel Reaction of TiCl(4) and benzyl Alcohol. *Applied Catalysis B: Environmental*, *76*, **2007**, 82–91.

[147] Gouttebaron, R.; Cornelissen, D.; Snyders, R.; Dauchot, J.P.; Wautelet, M.; Hecq, M. XPS Study of TiOx Thin Films Prepared by D.C. Magnetron Sputtering in Ar-O-2 Gas Mixtures. *Surface and Interface Analysis*, *30*, **2000**, 527–530.

[148] Mayer, J.T.; Diebold, U.; Madey, T.E.; Garfunkel, E. Titanium and Reduced Titania Overlayers on Titanium Dioxide(110). *Journal of Electron Spectroscopy and Related Phenomena*, *73*, **1995**, 1–11.

[149] Hook, A.; Nuber, T.P.; Celik, F.E. Density Functional Theory Investigation of the Role of Cocatalytic Water in Methane Steam Reforming over Anatase TiO_2 (101). Submitted manuscript.

[150] CH_x species generated from methane will further oxidize to form CO_2. The details of this mechanism were not investigated and are therefore omitted from the proposed mechanism.

[151] Seelam, P.K. Hydrogen Production by Steam Reforming of Bio-Alcohols. Acta Universitatis Ouluensis C Technica, *473*, **2013**.

[152] Riis, T.; Hagen, E.F.; Vie, P.J.S.; Ulleberg, Ø. Hydrogen Production R&D: Priorities and Gaps. *International Energy Agency – Hydrogen Co-Ordination Group, Hydrogen Implementing Agreement*, **2006**.

[153] Pennington, A.M.; Yang, R.A.; Munoz, D.T., Celik, F.E. Metal-Free Hydrogen Evolution over Defect-Rich Anatase Titanium Dioxide, International Journal of Hydrogen Energy, Submitted manuscript.

[154] Xu, S.; Walter, E.D.; Zhao, Z.; Hu, M.Y.; Han, X.; Hu, J.Z.; Bao, X. Dynamic Structural Changes of SiO_2 Supported Pt-Ni Bimetallic Catalysts over Redox Treatments Revealed by NMR and EPR. *Journal of Physical Chemistry C*, 119, **2015**, 21219-21226.

[155] Pennington, A.M.; Okonmah, A.I.; Munoz, D.T.; Tsilomelekis, G.; Celik, F.E. Changes in Polymorph Composition in P25-TiO_2 during Pretreatment Analyzed by Differential Diffuse Reflectance Spectral Analysis. *Journal of Physical Chemistry C*, *122*, **2018**, 5093-5104.

[156] Tang, Z.-K., Liu, W.-W., Zhang, D.-Y., Lau, W.-M., Liu, L.-M. Tuneable Band Gap and Magnetism of the Two-Dimensional Nickel Hydroxide. *RSC Advances*, *5*, **2015**, 77154-77158.

[157] Bakar, M.A., Hamid, M.A.A. Transformation Nanostructures Nickel Hydroxide to Nickel Oxide Film by Aqueous Chemical Growth. *AIP Conference Proceedings*, *1528*, **2013**, 359.

[158] Kodama, R.H.; Makhlouf, S.A.; Berkowitz, A.E. Finite Size Effects in Antiferromagnetic NiO nanoparticles. *Physical Review Letters*, *79*, **1997**, 1393-1396.

[159] Tang, H.; Lévy, F.; Berger, H.; Schmid, P.E. Urbach Tail of Anatase TiO_2. *Physical Review B*, *52*, **1995**, 11.

[160] Wergner, K.; Pratsinis, S.E. Scale-up of Nanoparticle Synthesis in Diffusion Flame Reactors. *Chemical Engineering Science*, *58*, **2003**, 20.

[161] Zhao, B.; Uchikawa, K.; McCormick, J.R.; Ni, C.Y.; Chen, J.G.; Wang, H. Ultrafine Anatase TiO_2 Nanoparticles Produced in Premixed Ethylene Stagnation Flame at 1 atm. *Proceedings of the Combustion Institute*, *30*, **2005**, 2.

[162] Zhao, H.; Liu, X.; Tse, S.D. Effects of Pressure and Precursor Loading in the Flame Synthesis of Titania Nanoparticles. *Journal of Aerosol Science*, *40*, **2009**, 11.

[163] Glumac, N.G.; Skandan, G.; Chen, Y.J.; Kear, B.H. Particle Size Control during Flat Flame Synthesis of Nanophase Oxide Powders. *Nanostructured Materials*, *12*, **1999**, 253–258.

[164] Abid, A.D.; Tolmachoff, E.D.; Phares, D.J.; Campbell, C.S.; Wang, H. Size Distribution and Morphology of Nascent Soot in Premixed Ethylene Flames with and without Benzene Doping. *Proceedings of the Combustion Institute*, *32*, **2009**, 1.

[165] Palanievelu, K.; Im, J.S.; Lee, Y.S. Carbon Doping of TiO_2 for Visible Light Potocatalysis – A review. *Carbon Science*, 8, **2007**, 3.

[166] Muhich, C.L.; Westcott IV, J.Y.; Furest, T.; Weimer, A.W.; Musgrave, C.B. Increasing the Photocatalytic Activity of Anatase TiO_2 Through B, C, and N doping. *The Journal of Physical Chemistry*, *118*, **2014**.

[167] Valentin, C.D.; Pacchioni, G.; Selloni, A. Theory of Carbon Doping of Titanium Dioxide. *Chemistry of Materials*, *17*, **2005**.

[168] Wu, B.; Liu, D.; Mubeen, S.; Chuong, T. T.; Moskovits, M.; Stucky, G.D. Anisotropic Growth of TiO_2 onto Gold Nanorods for Plasmon-Enhanced Hydrogen Production from Water Reduction. *Journal of the American Chemical Society*, *138*, **2016,** 1114-1117.

[169] Lalevée, J.; Bourgon, J.; Poupart, R.; Leroy, E.; Bastida, J.C.; Fouassier, J.-P., Verscace, D.-L. Oxygen-Mediated Reactions in Photopolymerizable Radical Thin Films: Applications to Simultaneous Photocuring under Air and Nanoparticle Formation. *Macromolecular Chemistry and Physics*, *216*, **2015**, 1702-1711.

[170] Petit, C.; Poli, E.; Favre-Réguillon, A.; Khrouz, L.; Denis-Quanquin, S.; Bonnevoit, L.; Mignani, G.; Lemaire, M. Unraveling the Catalytic Cycle of Tertiary Phosphine Oxides Reduction with Hydrosiloxane and Ti(OiPr)(4) through EPR and Si-29 NMR Spectroscopy. *ACS Catalysis*, *3*, **2013**, 1431-1438.

[171] Anpo, M.; Takeuchi, M. The Design and Development of Highly Reactive Titanium Oxide Photocatalysts Operating under Visible Light Irradiation. *Journal of Catalysis*, *216*, **2002**.